The Ratchet Effect
with cold atoms

Soliman Edris

PhD Thesis
Physics
UCL

April 2019

Principal Supervisor: Professor Ferruccio Renzoni
Second Supervisor: Professor Phil Jones

Declaration

I, Soliman Edris, confirm that the work presented in this thesis is my own. Where information has been derived from other sources, I confirm that this has been indicated in the thesis.

Abstract

This thesis describes the development and presents the results of a series of experiments on the ratchet effect with laser-cooled caesium atoms in a two-dimensional dissipative optical lattice.
The ratchet effect describes the directed motion of atoms that are undergoing an unbiased (time-average equal to zero) driving force, which can be realised experimentally using cold atoms in a driven optical lattice.
The thesis describes the experimental set-up and methods used to cool and trap atoms in a two-dimensional optical lattice using well-known laser-cooling techniques, as well as the computer software used to control the experiment. It then goes on to present the results of ratchet experiments with cold atoms in the two-dimensional driven optical lattice.
Using specific forms of the driving force – namely the biharmonic and split-biharmonic driving – the atoms undergo directed transport even though the driving forces time-average to zero, corresponding to a manifestation of the ratchet effect. The ratchet transport of the atoms is characterised for various parameters of the driving force.
The transport for *quasiperiodic* driving forces is considered by examining the velocity resonance as a function of relative frequency, and it is shown that the finite duration of the driving becomes a relevant parameter for determining the transport behaviour. An analysis of the structure of the velocity resonance is provided. The results of this work establish that quasiperiodic behaviour can only be guaranteed for long driving times and for those irrational numbers that have poor rational approximations.
The final chapter presents the work performed at the National Physical Laboratory on the rubidium atomic fountain in order to measure the rubidium-87 ground-state hyperfine splitting frequency. This work led to a publication [57] and subsequent redefinition [7] of the official value based on those measurements.

Impact statement

The work in this thesis addresses several aspects of active research with applications ranging across various subject fields, including cold atom physics, stochastic dynamics, and quasiperiodically driven systems. Both stochastic dynamics and quasiperiodicity are ubiquitous across much of science and even find a role in financial systems, and so enhancing their study is an ever-fruitful avenue of research.

The thesis details the production of a classical ratchet experiment using laser-cooled atoms in a two-dimensional dissipative optical lattice and, by using this ratchet, quantitatively investigates the transition to quasiperiodicity in driven systems. These new results equip us with knowledge of the regimes in which a system exhibits quasiperiodic phenomena, and can be immediately extended to *any* quasiperiodically driven system.

The ratchet effect describes the generation of motion out of unbiased fluctuations and finds its uses in biological systems as well as in nanotechnology, such as for particle separators and electron pumps. In two dimensions there is strong coupling between the degrees of freedom which has previously caused the overall direction of ratchet motion to be unpredictable. This thesis demonstrates a method to decouple the degrees of freedom using quasiperiodic driving fields, therefore making ratchet motion more predictable, which has particular implications for the aforementioned devices that utilise the ratchet effect.

The characterisation of the ratchet effect using 'split-biharmonic' driving has revealed subtle details about how the symmetries of the driving fields govern ratchet motion, showing that the shape of the motion and the direction of the motion are determined by separate symmetries; a fact which was previously obscured.

In the final part of the thesis a new measurement for the rubidium-87 ground-state hyperfine splitting frequency is presented. The rubidium frequency standard is currently the most popular secondary frequency standard used in practice, so excellent knowledge of this frequency is essential. Before this new result, only one other lab in the world had measured the frequency and the new measurement has already led to a redefinition of the value by the BIPM.

Acknowledgements

Firstly I would like to acknowledge Professor Ferruccio Renzoni and thank him for the opportunity to work in his buzzing lab. Also I would like to thank Professor Phil Jones, who was my secondary supervisor for this thesis and, before then, was my tutor during my undergraduate studies. I hold fond memories of my tutorials with him and wish I could have been more actively engaged with him during my PhD.

During my time as a post-grad at UCL I have had the privilege to work on several experiments with many talented people.

When I first joined the lab I was shown the ropes by Arne, Nihal, Boeing and Meliz on the rubidium-87 Bose-Einstein condensate experiment. Arne was my primary port of call when any issues arose – he is a very talented experimental physicist (even after his German advantage is taken into account). I enjoyed also the company of Cosimo, although he was generally tucked away in a corner soldering his electronics inventions, and Michal "The Theoretician" Hemmerling whose joviality injected the lab with a positive atmosphere. He could be found tapping away on his laptop, endlessly trying to locate files on his Linux laptop. I used to wonder why he didn't just make his life easier and get Windows. I am slowly but surely discovering why.

I then had the privilege of working for nine months with Professor Yuri Ovchinnikov on his rubidium atomic fountain at the National Physical Laboratory, Teddington. I am eternally grateful to him for sharing with me many experimental techniques and I admire his vast knowledge of cold atom physics. He is truly a walking encyclopaedia of experimental physics.

Upon returning to UCL to work on the ratchet experiment I found new members in the ever-expanding group – Michaela, Raffa, Roberta, Luca, Brendan (80% of whom are Italian. The clue is in the vowel endings!). Working with Roberta to develop her master LabVIEW program was a particular highlight. I enjoyed the conversations with Albert and Sarunas, who were talented Masters students and now PhD students elsewhere. I am sure they will go far and am expecting to read their names on some future seminal papers. Later Sarah, Pik and Cameron joined the group. I wish them the best success.

A lot of items in the lab were home-made and so John Dumper was crucial in sorting all our mechanical needs; drilling, hewing and carving out our aluminium designs.
Rafid "The Electrimagician" Jawal resolved all our electronic woes, with the

ability to pinpoint the exact dastardly capacitor that was bringing our system to its knees. No matter what sort of electronic ailment it is, Rafid can find the cure and so it was always a relief to go and visit him (with his stack of "WARRANTY VOID IF REMOVED" stickers piled in the corner).

I also had the rare opportunity to spend several days at the INF in Italy with Professor Emilio Mariotti and Dr Luca Tomassetti for an intensive stint to study the spectroscopy of Francium. These were a very memorable three days, with work continuing through the night for the entirety of the time. There my colleagues were all Italian, so it sufficed to use sign-language to interpret most of what they were saying. It was there that I first worked alongside Luca Marmugi, who later joined the group at UCL.

As well as those who I worked with directly, there are many people I encountered along the corridors of the physics department. I would like to thank Professor Peter Barker, who first sowed the idea in my mind to continue with a PhD. Much of his advice and warnings I now see manifest. Also Professor Ian Ford, whom I admired from afar. I respect his refined knowledge and scrupulous explanations of deep concepts.

My family have kept me going through the good and rough times. It was in fact my Aunty Sarah who instigated my step into a PhD and was always supportive with her caring encouragement and smiling eyes. And my Uncle Magdy, who had the special gift to make everyone around him happy, was always prompting me with new ideas. Tragically, they both passed away during my studies. I miss you both.

I'm surrounded on all sides by sisters! Salma, Sara, Amna. Their energy and warmth always keeps me smiling and I couldn't ask for better sisters and companions. Forgive me for all those "physics rants".

Finally I am ever grateful to my parents, Ayesha and Jimmy, who are the loves of my life and my strength and with their nurturing equipped me to face the world. They are truly the best role-models and I am honoured when in their presence.

Ultimately I glorify The Subtle Creator for creating our universe with its infinite depths and for giving us minds to marvel.

For my parents

Contents

List of Figures

Chapter 1

Introduction

All is Number

Pythagorean Brotherhood
6^{th} century BC

This thesis explores the emergence of quasiperiodicity in driven systems by using the ratchet effect with cold atoms in a two-dimensional dissipative optical lattice. The thesis begins by introducing the ratchet effect and the laser-cooling techniques used to obtain a cloud of cold atoms. It then goes on to describe the experimental set-up that was built to generate a two-dimensional ratchet system with cold caesium atoms. It culminates by presenting the results of the ratchet effect experiments, focussing chiefly on the emergence of quasiperiodic behaviour. The final chapter of the thesis describes the work performed at the National Physical Laboratory in Teddington to measure the hyperfine splitting frequency of the rubidium-87 ground-state.

This chapter introduces the ratchet effect from its theoretical conception to its modern use. It then discusses quasiperiodicity in driven systems and motivates its use in the ratchet effect. Finally, a brief outline of the thesis is provided.

1.1 The Ratchet Effect

To begin we provide a brief introduction to the ratchet effect. There are several exhaustive reviews [3, 15, 36, 66, 67, 68, 69] that cover most of the information in this section and much more in great detail, and I do not aim to compete with them but rather to give the reader a summary of what the ratchet effect is and a flavour of some of its implementations in research today.

The ratchet effect refers to the generation of directed motion out of unbiased fluctuations. It may at first appear unfeasible that a non-zero direc-

ted motion can occur as a result of zero-mean fluctuations, so to elucidate how this may be achieved let us introduce two classical thought experiments that demonstrate the idea behind the ratchet effect – they are the Feynman-Smoluchowski ratchet, and Brillouin's rectifier.

1.1.1 The Gedanken Experiments

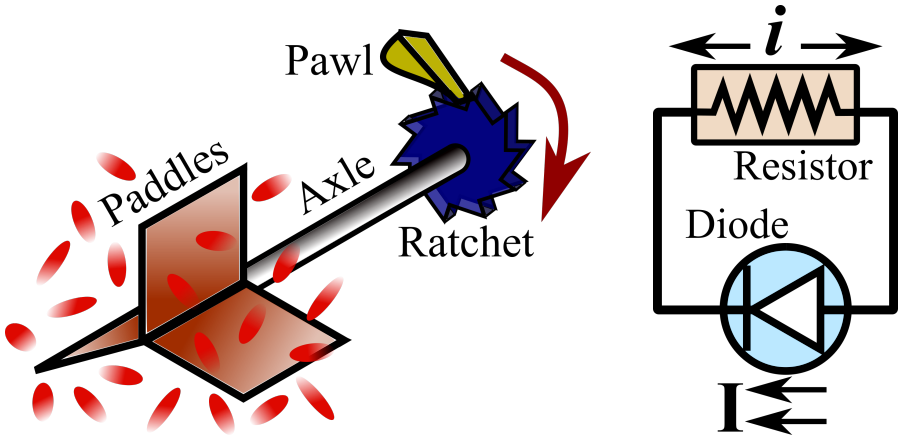

(a) Feynman ratchet (b) Brillouin rectifier

Figure 1.1: Depictions of the Feynman-Smoluchowski ratchet (left) and the Brillouin rectifier (right). Both of these provide examples of how at first sight it might appear that useful work can be extracted from zero-mean fluctuations. For the Feynman ratchet, the impact from the Brownian motion of particles on the paddle wheel induces a net rotation of the ratchet. Useful work could be extracted by lifting a weight attached to the axle. For the Brillouin rectifier, consisting of a resistor in series with a diode, it appears to be possible that random thermal noise in the resistor is rectified by the diode. Enough of these circuits in series could be used to charge a battery. The correspondence between the two devices is paddles⇔resistor, ratchet⇔diode.

The Feynman-Smoluchowski ratchet is the name given to a device first considered by Smoluchowski in 1912 [75], popularised by Feynmann in 1964 [22], and artistically rendered by Edris in figure 1.1a, in the so-called Feynman-Smoluchowski gedanken experiment. In that thought experiment it is considered whether a ratchet and pawl could be used to rectify the Brownian motion of particles. This is demonstrated in figure 1.1a, where particles undergoing Brownian motion bombard a paddle wheel. This paddle wheel is connected by an axle to a ratchet and pawl mechanism that restricts the system to rotate in one direction only. Even though the Brownian motion of the particles averages to zero, with this set-up it appears that the ratchet will

eventually rotate in a specific direction.
So here is a device that produces directed motion (ratchet rotating) out of unbiased fluctuations (Brownian motion). The problem, however, is that if such a device were to function then it could be used to do useful work (for example by lifting an item attached to the axle), and this would violate the second law of thermodynamics, as it would constitute a heat-engine at thermal equilibrium. Feynman resolved this apparent dilemma by realising that if the ratchet/pawl mechanism is sensitive enough to be affected by the Brownian motion of atoms, then it surely will experience Brownian motion itself. This means that even though the mechanism has a likelihood to rotate one way, it also has a likelihood to rotate back due to its own Brownian fluctuations. Therefore, in thermal equilibrium the net motion remains zero and no net work can be done; the second law of thermodynamics is obeyed.

The Brillouin rectifier is another classic example of a device that appears to extract useful work from unbiased fluctuations. It was first introduced as a thought experiment by Brillouin in 1950 [8], and it is a simple circuit comprising a diode in series with a resistor, as depicted in figure 1.1b. At a finite temperature, but at thermal equilibrium, there is non-zero (but zero-average) thermal noise in the resistor. With the diode present it appears that the noise can be rectified and with enough of these circuits one could, for example, charge a battery, thereby extracting useful work. As with the Feynman ratchet, this would violate the second law of thermodynamics and, as with the Feynman ratchet, the resolution lies in the microscopic dynamics of the system. In the case of the diode, the microscopic inductive response means that electron motion one way is exactly balanced by motion the other way and no net motion occurs. This was of course resolved by Brillouin in that same paper.

In both cases the symmetry of detailed balance is obeyed, which states that in thermal equilibrium the probability of the forward and reverse processes is balanced.

Therefore, the first vital ingredient to observe the ratchet effect in a system is that the system must be out of equilibrium. This was already considered by Feynman when he extended the idea so that the ratchet/pawl and the paddle are held at different temperatures. In this case the system is not in thermal equilibrium and directed motion can in fact occur.

1.1.2 Requirements for the ratchet effect

There are two necessary requirements for the ratchet effect. The first is that the system must be out of equilibrium, as revealed in the previous section. The second requirement is that there must be a system symmetry that is broken, in order for there to be directed motion. In the case of the Feynman-Smoluchowski ratchet this second requirement is fulfilled by the asymmetric

teeth of the ratchet, which ensures rotation is in one direction only. For the Brillouin rectifier, the asymmetry is provided by the current-flow direction imposed by the diode.

In fact, it has been suggested that *any* system possessing these two attributes should exhibit directed transport [24]. This can be regarded as a manifestation of Curie's principle, which is expressed in many different forms, from the colloquial "if it can happen it will happen", to the more formal "the symmetries (or asymmetries) present in causes of phenomena must be present in the phenomena themselves". For the purposes of our experiments we use the mantra "if the symmetries don't forbid it, we expect to see transport".

1.1.3 Ratchet realisations

Since the ratchet effect is generic to systems out of equilibrium and with a broken symmetry, it can be found in a wide variety of systems, ranging from biological all the way to financial.

It has been proposed as the mechanism behind molecular motors [4, 5, 83]. The ratchet transport of biological molecular motors is responsible for muscle contraction in most living organisms. The protein motors are driven by chemical combustion and they undergo directed motion along an asymmetric landscape in a highly damped environment in the absence of any net force. The ratchet effect is believed to be responsible for this.

It is also exhibited in macroscopic objects such as in mercury drops [30] and Leidenfrost droplets [49], where these liquids undergo directed motion with a low frequency zero-mean driving.

There has also been consideration for its application as a particle pump [79] and particle separator [61, 71, 82]. In these schemes the inherent sensitivity of the motion to the system parameters is exploited to provide the required ratchet motion. The diffusion constant is dependent on the particle properties and, since ratchet motion is sensitive to the diffusion constant, different particles can be manipulated differently. Under certain circumstances different particles can be made to move in opposite directions, providing separation mechanisms.

In all of the above ratchets the asymmetry is provided by an asymmetric potential and the system is driven out of equilibrium by some applied zero-mean force.

More exotic forms of the ratchet effect have been observed in solid-state devices, such as ratchet-like motion of magnetic flux quanta (vortices) in superconductors [84, 74] and voltage rectification across Josephson junctions [85, 52]. There have also been demonstrations in graphene [25], where impurities introduced by adatoms or on the substrate provide the asymmetric potential landscape. With an electric field driving, a ratchet-like motion of the electrons occurs producing a measurable current.

Also there is evidence of the ratchet effect in nanowires [63], where the characteristic current reversals produced a pronounced change in the resistance of the wires by up to several orders of magnitude.
The ratchet effect has even found its use in game theory [58], where by playing two losing games in a specific alternating sequence, one can produce a winning result. This amounts to a rectification of a dissipative (losing) process.

Another field that is expanding is the study of quantum ratchets [20, 19, 72]. With quantum ratchets new effects arise, such as quantum resonances where the velocity spikes at specific multiples of photon recoil frequency due to a mixing/interference of states. Another characteristic feature of quantum ratchets is that the transport depends on the starting phase of the driving force, which is contrary to classical ratchets where the system holds no memory of the initial conditions.

The ratchet effect was first observed with cold atoms in 1999 [51] for rubidium atoms in an asymmetric optical lattice potential. Since then there have been multiple realisations of cold atom ratchets [39, 27, 28, 26]. Cold atoms in optical lattices provide an excellent test-bed for studying the ratchet effect as optical lattices are generally quite adjustable, permitting many different ratchet configurations to be realised. For example, different lattice topologies can be formed, providing customisable asymmetric potentials, and also the driving forces can be varied with ease. Furthermore, the level of dissipation can be controlled via the optical lattice detuning.

For this thesis, cold caesium atoms in a two-dimensional dissipative optical lattice are used to observe the ratchet effect. In this case the atoms undergo Brownian motion and move stochastically across the symmetric lattice. When they are driven out of equilibrium by an asymmetric driving field, the atoms undergo directed motion even though the driving force time-averages to zero, corresponding to a realisation of the ratchet effect.

1.2 Irrationality and Quasiperiodicity

In this section we illustrate how irrationality manifests itself in physical systems in the form of quasiperiodicity. We begin by demonstrating what is meant by an irrational number in terms of incommensurate magnitudes. In this way we illustrate how incommensurate magnitudes must be treated independently, thereby extending the system's number of degrees of freedom. When this is transferred to quasiperiodically driven systems, the two incommensurate driving frequencies act independently, which can have profound implications for the system dynamics.

1.2.1 Irrational numbers and incommensurate magnitudes

To begin we reintroduce irrational numbers in the context of incommensurate magnitudes.
The real numbers can be split into the set of rational numbers and the set of irrational numbers. An irrational number is one that cannot be represented as a ratio of two integers. This means that it usually requires its own special representation in the form of a symbol, such as π, $\sqrt{2}$, e, φ. These each require their own individual hieroglyph because they are impossible to express as a fraction or in decimal form.

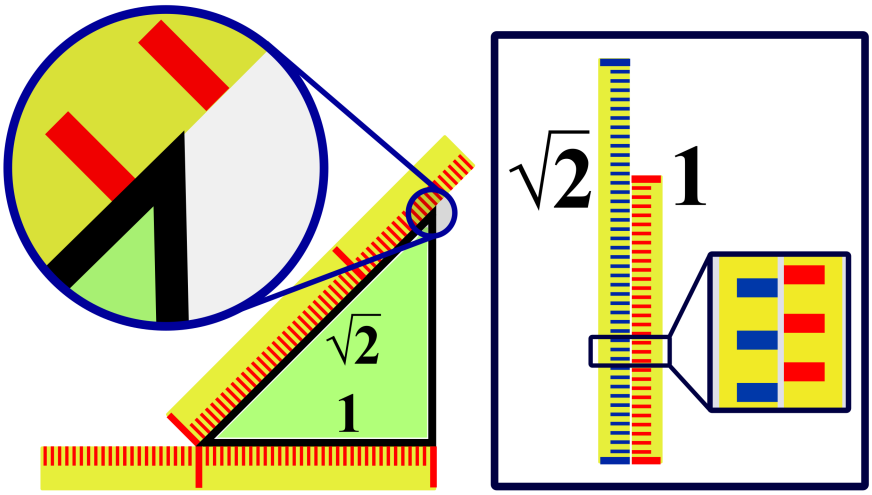

Figure 1.2: The irrational number $\sqrt{2}$ and the base unit 1 are incommensurable, meaning that it is impossible to use the same ruler to measure them both exactly. No matter how small we make the measurement divisions, an incommensurate magnitude will always lie in between two divisions and never hit the mark. To measure both sides we require two rulers – a $\sqrt{2}$ ruler and a unit 1 ruler – with divisions spanning over separate points in space.

Another illuminating way of considering irrational numbers is represented in figure 1.2, where the irrational length $\sqrt{2}$ is considered in relation to the unit length 1. If we were to get a ruler and mark out the side of length 1 – as represented by the thicker red lines on the ruler in the image – and then we were to divide this length into an arbitrarily large number of divisions, and then were to measure the side of length $\sqrt{2}$, we would find that the vertex lies in between two divisions and never exactly on one. This is regardless of how many divisions we make. We could then choose to split each division into a million (billion, googol), and still the measured $\sqrt{2}$ length would lie between two divisions. This is quite astounding, as the two magnitudes are mutually immeasurable. They simply cannot be represented in terms of each other.

When two values are as such, they are termed *incommensurate* or *incommensurable*. Irrational numbers are incommensurate with rational numbers, and in most cases irrational numbers are incommensurate to other irrational numbers.

When two values are incommensurate they are in some sense independent quantities. They must be treated as spanning separate spaces and in this way the dimensionality, or the number of degrees of freedom, is increased.

1.2.2 Quasiperiodicity in physical systems

Quasiperiodic means almost-periodic; quasi meaning 'almost' in Latin. Quasiperiodicity can be manifest spatially, such as in a quasiperiodic lattice, or temporally, such as with quasiperiodic driving. The concepts of quasiperiodicity and irrationality in numbers are linked. The irrationality arises in the ratio of the constituents that compose the quasiperiodic structure. For example, in the case of a quasiperiodic atomic lattice these two components may be the number of atoms of two species constituting the lattice. If the ratio of the number of the two species is irrational, then the lattice becomes quasiperiodic. For an optical lattice, the quasiperiodicity is determined by the irrational ratio of the laser beam wavevectors forming the lattice [34]. For a driven system, the quasiperiodicity is determined by the irrational ratio of the driving frequencies [28, 12].

Just as with the treatment of irrational numbers, quasiperiodicity results in an increase in the number of degrees of freedom [23], such that the incommensurate magnitudes are treated independently.

1.2.3 The emergence of quasiperiodicity in real experiments

Strictly, quasiperiodicity in driving frequencies is only defined for infinite-time experiments, and quasiperiodic geometric lattices are only defined for infinite lattices. To make a direct numerological analogy, an irrational number is only defined by an infinite decimal expansion, an infinite series, or an infinite continued fraction. Indeed the current record for the number of decimal places of the famous irrational π currently stands at just under 22.5 trillion, and it is irrational up to that digit. If, however, it was found to start repeating itself then it would formally be a rational number[1]. Similarly, two frequencies can only be defined as absolutely quasiperiodic in the infinite-time limit. At short times, however, a quasiperiodic driving and a periodic driving with a long time period are indistinguishable. This then raises the question – at what point does a system transition from periodic to quasiperiodic?

[1] There is actually a mathematical proof that π is irrational, so this is unlikely to happen any time soon.

What is deemed as "quasiperiodic behaviour" is difficult to define in a general sense as it depends on the system at hand, but the general treatment for dealing with quasiperiodic systems [23, 12] is to introduce an additional degree of freedom into the system. This additional degree of freedom can impact the system dynamics, thereby manifesting "quasiperiodic behaviour". In some cases the transition from periodic to quasiperiodic behaviour can mean quite a pronounced change in dynamics, for example in [52] a transition to quasiperiodicity in their solid-state device corresponds to a phase transition from a resistive to a super-conductive state.
The transition from periodicity to quasiperiodicity for driven systems is explored and characterised in this thesis, specifically in chapter 6, where it is demonstrated that the transition to quasiperiodicity has a discernible effect on the atomic dynamics, completely suppressing ratchet motion.

1.2.4 Decoupling the degrees of freedom

In a two-dimensional lattice it is possible to produce ratchet motion along each direction. The motions along each direction are not independent however, and this means that predictability of ratchet motion is lacking. Previous experiments by the group [43, 42] have demonstrated that the direction of motion is difficult to predict as a result of the coupling between transverse degrees of freedom. It has been suggested [14] that by using quasiperiodic driving fields, the degrees of freedom can become decoupled and the direction of motion more predictable. This decoupling is due to the increase in the system's number of degrees of freedom, which comes about as a result of the quasiperiodic driving.

In this thesis we demonstrate that the coupling between transverse degrees of freedom is suppressed for quasiperiodic driving fields, and quantify under what conditions a driven system may be regarded as quasiperiodic, as it is not guaranteed for all driving parameters.

1.3 This Thesis

This thesis explores the transition from periodic to quasiperiodic behaviour in driven systems by using the ratchet effect. A quasiperiodic driving arises when the ratio of the driving frequencies is irrational, and so the transition from periodic to quasiperiodic driving corresponds to a transition from a rational to an irrational frequency ratio. This transition is not so stark as the rational numbers and irrational numbers form a tight weave where between every pair of rational numbers there lies (uncountably) infinitely many irrational numbers and (countably) infinitely many rational numbers. Alas, what hope can there be in exploring the transition between the two?

We use the ratchet effect to observe the transition to quasiperiodicity. In

order to do this we make use of the split-biharmonic driving, which relies on the coupling between two transverse driving fields in order to produce motion. When the driving fields are quasiperiodic they become independent, due to an increase in the system's number of degrees of freedom (since we now require two 'rulers' instead of one). This means that the driving fields become decoupled as a result of the transition to quasiperiodicity and so with the split-biharmonic driving, where the coupling between the driving fields is essential for transport to occur, we are able to witness this decoupling by observing a suppression of transport. In this way it is possible to explore and quantify the transition from periodic to quasiperiodic driving by measuring the atoms transition from a regime of transport to no transport.

The structure of the thesis is as follows:
Chapter 2 provides a theoretical background for the topics in this thesis, starting with a brief summary of the concepts of laser cooling and trapping in cold atom experiments. Then the ratchet effect is considered and a powerful symmetry analysis is introduced that allows us to establish regimes where the ratchet effect can be observed.
Chapter 3 provides a description of the experimental set-up used to produce the ratchet effect in a two-dimensional optical lattice. There the laser systems for the magneto-optical trap and lattice are described as well as the generation of the ratchet driving forces.
Chapter 4 describes the computer control software, which represents quite a sophisticated software architecture developed specifically for this project.
Chapter 5 presents results of the one-dimensional ratchet effect in the two-dimensional optical lattice. It illustrates the manifestation of the symmetry conditions in the transport, and it also serves to characterise the transport current as a function of the different driving force parameters.
Chapter 6 presents results for the two-dimensional ratchet effect, where it is demonstrated that the transverse degrees of freedom are strongly coupled. The condition for quasiperiodicity is investigated and it is shown that in a real experiment incommensurability is determined by the finite interaction time, where quasiperiodic behaviour is shown to be only guaranteed at longer driving times. It is also considered how the coupling between transverse degrees of freedom can be suppressed using quasiperiodic driving fields and how this may be used to create ratchet currents with arbitrary, but deterministic, directions.
Chapter 7 concludes the ratchet experiments and provides a discussion of the results and presents an outlook for the next generation of ratchet experiments.
Finally chapter 8 describes the work performed at NPL, where I spent nine months during the beginning of my PhD working on the rubidium atomic fountain clock. During this time the fountain was upgraded and data was taken for an absolute measurement of the rubidium ground-state hyperfine

splitting frequency. This new measurement is published in Metrologia [57], and the BIPM subsequently adjusted the recommended value based on this new result.

Chapter 2

Theoretical Background

This chapter presents some theoretical background for the topics in this thesis. First it describes the principles of laser cooling of neutral atoms, which was developed mainly in the past 50 years. It then presents a symmetry analysis treatment of the ratchet effect, which proves to be a powerful tool for determining the expected form of ratchet current.

2.1 Atomic structure

In modern laser cooling experiments, alkali metals such as rubidium and caesium are favoured as study cases because they possess a single valence electron, making them Bohr-like atoms. Laser cooling manipulates the *hyperfine* states of the valence electron, labelled by quantum number F. The energy splitting for different depths of atomic structure is represented in figure 2.1, showing how a relatively simple atomic system has many internal states.

The energy splitting between different hyperfine states is typically of the order of several hundred MHz to several GHz. The hyperfine splitting of the caesium ground-state is used as a primary frequency standard to *define* the second. It has a value of 9 192 631 770 Hz, which is an exact value in virtue of the definition of the second.

2.2 Cooling and trapping atoms

An excellent and accessible review of the birth and development of laser cooling for neutral atoms is given by Bill Phillips in his Nobel prize lecture [59].

The term laser cooling refers to the use of laser fields to reduce the velocity of atoms. A velocity-dependent temperature is associated to the atoms by equating their average kinetic energy $\left\langle \frac{1}{2}mv^2 \right\rangle$ to their thermodynamic energy $\frac{1}{2}k_BT$. In this way, slow atoms are described as 'cold' atoms and the process of slowing the atoms is described as 'cooling'.

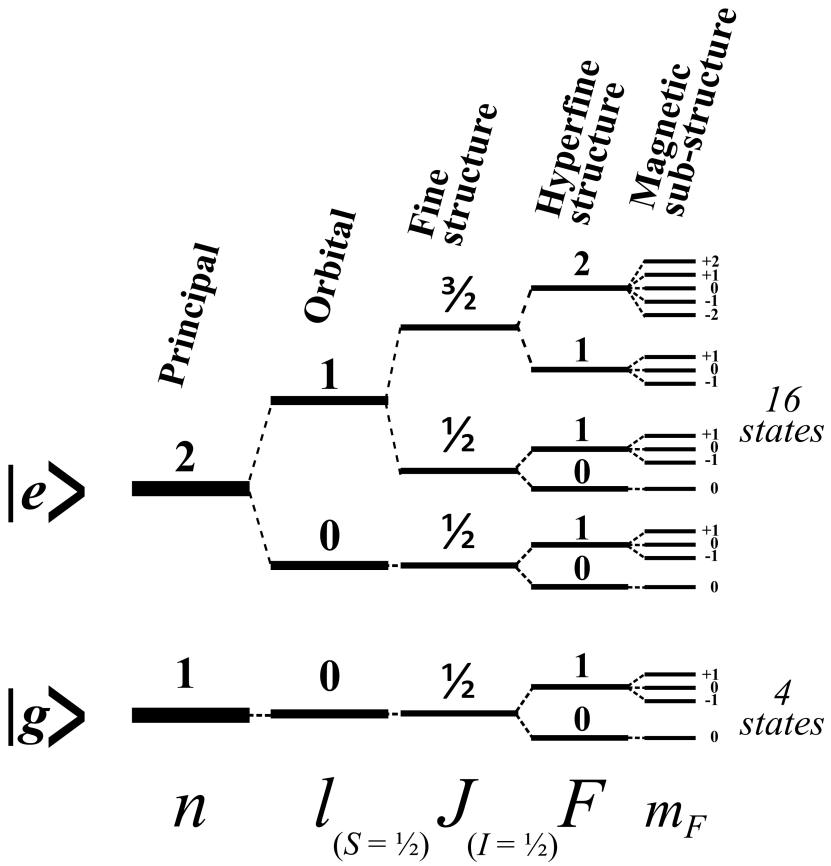

Figure 2.1: The energy-level splitting for a simple electron transition. Here the minimum possible quantum numbers are chosen, and already there are four ground sub-states and sixteen excited sub-states. Neglecting selection rules there would be sixty-four possible transitions, but the transition selection rules limit this number significantly. If higher quantum numbers were chosen there would be even more possible states and more possible transitions.

Although laser cooling and trapping started as a study in its own right [44, 37, 45], it is now used in many modern atomic physics experiments as a method to obtain a cloud of cold atoms, which are subsequently used for myriad purposes.

Laser cooling has become particularly popular since the mid-90's when it was demonstrated that it can be used to cool atoms down to quantum degeneracy [2, 18], as is done with Bose-Einstein Condensates. When a cloud of atoms is cooled to quantum degeneracy, the atomic de-Broglie waves become coherent and the entire cloud can be formally described by a single

wavefunction, with the coherence length of this wavefunction extended over the entire ensemble. In some experiments this macroscopic coherence of the atomic cloud wavefunction is exploited to make quantum sensors such as gravimeters and gravity gradiometers [41].

It often surprises non-specialists that lasers, which are usually portrayed as burning and blinding, can end up reducing the energy of delicate atoms. It is by exploiting the interaction of light and atomic energy levels that we are able to play this trick.

2.2.1 Laser cooling and optical molasses

According to quantum theory, the electron orbitals of an atom have discrete energy levels. Electrons can transition between these quantised energy states by absorbing or emitting a photon with energy equal to the energy difference between the states. When an electron absorbs a photon it is excited to a higher energy state, where it remains for a period determined by the lifetime of that state, before transitioning back to a lower energy state, emitting a photon in the process. We can therefore use carefully tuned laser light to excite the desired transitions and thereby manipulate the energy state of the atoms.

Laser cooling makes use of the absorption/emission process to reduce the energy of atoms. This is performed in the following way. Consider exposing atoms to laser light that is close to the resonant frequency of an atomic transition. An atom will absorb a photon and gain a momentum kick of $\hbar k$ along the direction of the laser beam, where $k = \frac{2\pi}{\lambda}$ is the wavenumber of a laser operating at wavelength λ. The atom then emits a photon in a random direction, which gives it a recoil kick of $\hbar k$ in a random direction. After many cycles of this process the atom has gained momentum primarily along the direction of the beam and lost momentum in random directions (with zero net direction). In this way a laser beam is able to exert a net force along its direction on an atom scattering the laser light.

It may be presumed that applying counter-propagating beams along the three dimensions would suffice to trap atoms, by pushing inwards from all directions. Unfortunately this is not the case, as atoms very quickly diffuse out of the trapping centre. Instead, another trick is played with the light, which makes use of the Doppler effect to provide a velocity-dependent damping force on the atoms, which slows the atoms down.

The underlying principle behind laser cooling is the Doppler effect. Consider a cloud of atoms that is illuminated by a red-detuned beam. The red-detuning refers to the laser having a slightly lower energy than the atomic

transition energy (lower energy corresponds to lower frequency, which corresponds to a longer ('redder') wavelength). Atoms moving with respect to this laser will experience the light as Doppler-shifted – blue-shifted for atoms moving towards the beam and red-shifted for atoms moving away from the beam. Therefore an atom moving towards the red-detuned beam will experience the beam as closer to resonance in the atom's reference frame, and atoms moving away from the beam will experience the beam as further from resonance. This means that atoms scatter more photons from the beam they are moving towards, which acts as an effective velocity-dependent damping force.

When six red-detuned laser beams are impinged on the atoms from the six directions of space, we obtain a velocity-dependent damping along all directions [10]. This configuration is called optical molasses, referring to the viscous damping of molasses.

Optical molasses works well for slowing down – or cooling – atoms, but it is not very effective as an atomic trap as the atoms may be damped but they are not localised. In order to apply a position-dependent force that will work as a trap we make use of the magnetic sub-structure of the hyperfine states, and use magnetic fields in collaboration with the light.

2.2.2 Magneto-optical trap (MOT)

As has been mentioned, the atomic energy levels are given by the hyperfine energy levels. Each of the hyperfine energy levels, F, has additionally $2F+1$ magnetic sub-states, which can be labelled by quantum numbers m_F. With zero magnetic field the magnetic sub-states are energy-degenerate and the atoms are distributed equally across all sub-states. With non-zero magnetic field the degeneracy is lifted and the sub-states attain an additional energy $\Delta E = \pm m_F g_F \mu_B |B|$ corresponding to the Zeeman splitting. These sub-states and their corresponding transition selection rules are exploited to form the magneto-optical trap.

The transition selection rules for magnetically sensitive hyperfine levels are given by $\Delta m_F = \pm 1$ for $\sigma^{\pm}$ circularly polarised light respectively. Therefore, absorption of σ^+ light has the tendency to optically pump atoms into the higher m_F states, and absorbing σ^- will pump atoms to lower m_F states. These selection rules along with the Zeeman splitting dependence on the magnetic field and a circularly-polarised, red-detuned laser beam are used in conjunction to trap atoms. This is demonstrated in figure 2.2, where a magnetic field with a linear dependence in space produces a spatial dependence of the magnetic sub-state energies. As atoms move away from the centre (where the magnetic field is zero) they are optically pumped to a state with an energy

closer to resonance with the opposing beam, causing them to scatter more light from that beam, which produces a net force back to the centre. In this way atoms have a spatially dependent force that tends to keep them localised around the magnetic field minimum.

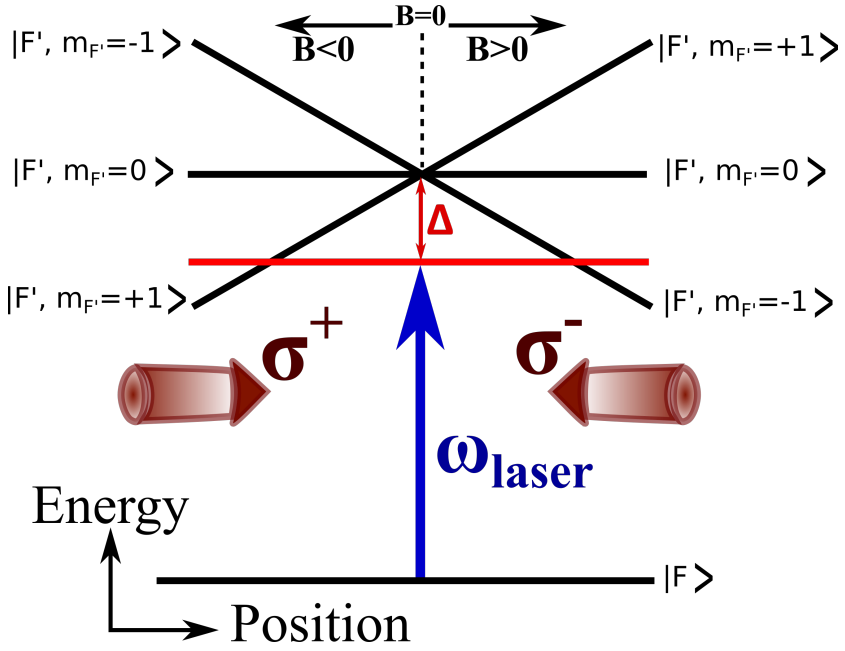

Figure 2.2: The working principle of the MOT along one axis. The configuration of the laser beams with respect to the orientation of the magnetic field means that as atoms move further from the centre they are closer to resonance with the counter-propagating beam, which produces a net force back towards the centre.

Since our cooling and trapping techniques require the absorption and subsequent re-emission of light, it is necessary to work with atomic energy states that have a high rate of absorption and re-emission. Therefore we require a cycling transition with a relatively short life-time of the excited state. For caesium-133 alkali metal we use the D_2 $F = 4 \rightarrow F' = 5$ hyperfine transition. This is a cycling transition, meaning that atoms excited from $F = 4 \rightarrow F' = 5$ then decay back to the $F = 4$ ground-state. In practice, there is a small probability that atoms decay to the $F = 3$ ground-state and are lost from the cycling transition. To counteract this effect we use a repumping beam, which transfers atoms from $F = 3 \rightarrow F' = 4$, which then decays back into the $F = 4$ ground-state to rejoin the cycling transition.

2.3 Optical lattices

Optical lattices are formed by the interference of overlapping coherent laser beams [35]. In this configuration, the light field produces a perfectly ordered array/lattice of nodes and anti-nodes corresponding to high and low intensity regions of the light field. Optical lattices are typically classified in terms of their detuning. Far-detuned optical lattices provide a conservative (non-dissipative) potential to trap atoms. Near-detuned lattices also trap atoms as well as providing a dissipative cooling mechanism – called Sisyphus cooling – that can cool atoms below the Doppler limit. The difference between the two regimes arises as a result of the repressed scattering rate as the detuning is increased, since the scattering rate Γ' scales as the inverse square of the detuning Δ: $\Gamma' \propto 1/\Delta^2$.

2.3.1 Lattice geometry

An optical lattice is formed by the interference of coherent laser beams that are overlapping. The lattice geometry is determined by the orientation of the laser beams with respect to each other as well as their relative phases. In general an n-dimensional lattice can be formed from $n+1$ beams. A one-dimensional lattice can be formed by counter-propagating beams with linear polarisations. The beams must be phase-coherent to avoid any drift of the lattice due to drifting relative phases. When the beams are coherent and their polarisations are orientated the same, there is interference between the beams and a standing wave is formed with nodes and anti-nodes corresponding to constructive and destructive interference of the electric field. This forms a one-dimensional optical lattice. The period of the lattice is equal to half the wavelength of the lattice light, which is usually around a fraction of a micron (0.426 microns for 852 nm light). Therefore, for a lattice formed from a beam with a width of several millimetres there can be tens of thousands of lattice sites.

It is possible to form a two-dimensional lattice by overlaying two one-dimensional lattices at transverse directions to each other, which would require four laser beams. Instead we use a different configuration with just three laser beams orientated such that they lie in the same plane with 120° angle between them mutually, which forms a hexagonal lattice. In fact, using three beams instead of four is somewhat a necessity since the topography of an n-dimensional lattice is insensitive to phase-drifts only if it is formed from $n+1$ laser beams [31], and so we use three beams to form our two-dimensional lattice.

The benefit of optical lattices is that they are perfectly defect-free as they are formed by light interference. Also they are highly tuneable such that the

lattice geometry can be changed drastically and in-situ. These two features are not true of solid-state lattices, and so optical lattices make an excellent candidate as a test-bed for concepts in solid-state physics.

The force experienced by the atoms in a lattice is produced by the potential gradient of the laser potential, corresponding to the light shift. This dipole potential gradient means that atoms are generally localised around lattice site minima, where the force reduces to zero. The Brownian motion random walk of an atom in a lattice corresponds to the atom scattering photons and moving stochastically across lattice sites.

2.3.2 Sub-Doppler cooling in an optical lattice

The scattering of photons imposes a fundamental limitation on the temperature that can be achieved with Doppler cooling. This limit is termed the Doppler temperature T_D and is directly proportional to the natural linewidth Γ of the transition, that is $k_B\,T_D = \hbar\Gamma/2$. For the caesium-133 $D2$ cooling transition the Doppler temperature is $125\,\mu$K.

It is possible to surpass this Doppler limit, however, as was experimentally discovered in 1988 [46], and shortly after a theory for sub-Doppler cooling based on polarisation gradients was developed [17]. The following section gives a brief description of this mechanism occurring in an optical lattice, termed Sisyphus cooling.

Sisyphus cooling

Sisyphus cooling refers to the cooling of atoms in an optical lattice as a result of the changing polarisation landscape experienced by the atoms [11, 87]. The process is represented in figure 2.3, where an atom moving through the lattice is optically pumped to the state with the lowest potential energy, thereby causing the atom to dissipate energy to the light field.

This form of cooling is termed 'polarisation-gradient cooling' because the interference of the lattice beams produces a position-dependent polarisation. The Zeeman sub-states of the atom experience different lattice potentials, and the correspondence between the lattice nodes and the polarisation nodes ensure that the atom is optically pumped to the state at the lattice minima just as they reach the maxima. The atoms lose energy with each transition and so are cooled after multiple cycles.
The name Sisyphus cooling stems from the Greek legend of Sisyphus, King of Ephyra, who is doomed to roll a boulder up one of Hades' many ever-inclining slopes. Just before Sisyphus can reach the summit, the boulder rolls back down again on account of its weight so that apparently, according to my sources in the Underworld, poor Sisyphus is still going to this day.

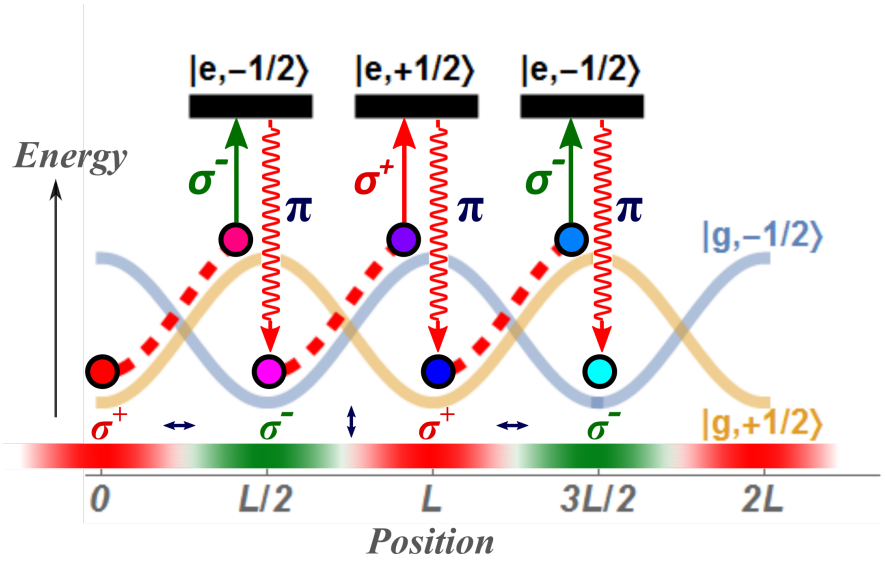

Figure 2.3: An illustration of the mechanism for Sisyphus cooling. An atom moving across the lattice converts its kinetic energy to internal energy as it climbs up the potential hill. Just as it reaches the top it has a high probability to transition to the state with lower potential energy due to the corresponding polarisation maximum. After several cycles of this process the atom dissipates its energy and can be cooled below the Doppler limit.

2.4 The ratchet effect with cold atoms

The ratchet effect refers to the generation of directed transport out of unbiased fluctuations. The ratchet effect has its origins in a thought-experiment by Smoluchowski [75] where it was considered whether random Brownian fluctuations could be used to do useful work. If this were the case it would constitute a Maxwell demon. Due to the second law of thermodynamics it is not possible for Brownian motion to perform useful work when the system is in thermal equilibrium. Out of equilibrium, however, the dynamics change and the ratchet effect can be realised.

In order to observe the ratchet effect two ingredients are required: first, the system must be out of equilibrium, which in our experiments is provided by a time-dependent rocking force driving the system out of equilibrium. Second, the system requires a broken symmetry, spatial or temporal, to permit the asymmetric transport that is characteristic of a ratchet. In the case of atoms in a hexagonal optical lattice, as in our experiments, the system is spatially symmetric and so we use the driving force to break the temporal symmetry of the system.

Therefore the driving force supplies both of the necessary elements to produce a ratchet.

Even with these ingredients at hand, it is still left to determine the correct recipe to cook up a ratchet. In order to analyse the conditions under which the ratchet effect can be observed we make use of a symmetry analysis, which is found to be a powerful tool enabling accurate predictions of the form of directed transport. This symmetry analysis was first introduced by Flach *et al.* [24], but it is presented here in a way that is tailored for our specific form of driving.

2.4.1 Symmetry analysis

Consider a particle of mass m experiencing a spatially-dependent potential $U(x)$, subject to friction with coefficient γ, under the influence of a time-dependent driving force $f(t)$, and subject to noise $\xi(t)$. The equation of motion for this particle is given by the following Langevin equation:

$$m\underline{\ddot{\mathbf{x}}} = -\gamma\underline{\dot{\mathbf{x}}} - \underline{\mathbf{U}}'(\underline{\mathbf{x}}) + \underline{\mathbf{f}}(t) + \underline{\xi}(t),$$

which can be rewritten in terms of momentum $\underline{\mathbf{p}}$ as

$$\underline{\dot{\mathbf{p}}} = -\frac{\gamma}{m}\underline{\mathbf{p}} - \underline{\mathbf{U}}'(\underline{\mathbf{x}}) + \underline{\mathbf{f}}(t) + \underline{\xi}(t), \tag{2.1}$$

where the dot and prime denote differentiation with respect to time and space respectively.

In the case of cold atoms in an optical potential, the $\underline{\dot{\mathbf{p}}}$ term corresponds to the inertia; the $-\underline{\mathbf{U}}'(\underline{\mathbf{x}})$ term describes the dipole force due to the optical lattice potential; the $-\gamma\underline{\mathbf{p}}/m$ term corresponds to the optical damping due to Sisyphus cooling; the $\underline{\mathbf{f}}(t)$ term corresponds to the time-dependent driving force, implemented by modulating the lattice frequency; and the noise term $\underline{\xi}(t)$ is the Brownian motion expressing the random walk of the atoms due to light scattering.

The purpose of the symmetry analysis is to find those symmetries of the equations of motion that *forbid* directed transport. By this knowledge of the conditions where transport is forbidden, we can move to regimes where these symmetries are broken and transport is permitted.

In order to determine the symmetries of the system that forbid directed transport we consider transformations that reverse the particle's momentum such that $\underline{\mathbf{p}} \to -\underline{\mathbf{p}}$. The reason we do this is because if the system (ie: the Langevin equation) is invariant under such a transformation it means that $\underline{\mathbf{p}} = -\underline{\mathbf{p}}$ and therefore $\underline{\mathbf{p}} \equiv 0$; the momentum is zero and so directed transport

is forbidden. If the Langevin equation is invariant under such a transformation we say that the system is symmetric under that transformation.

There are in fact two transformations that invert the momentum $\underline{\mathbf{p}} \to -\underline{\mathbf{p}}$. Considering that the momentum is defined as $\underline{\mathbf{p}} = m\frac{\mathbf{dx}}{dt}$, then the two transformations are

$$\begin{aligned} \hat{T}_1 : \quad & \underline{\mathbf{dx}} \to -\underline{\mathbf{dx}} \quad & dt \to dt \\ \hat{T}_2 : \quad & dt \to -dt \quad & \underline{\mathbf{dx}} \to \underline{\mathbf{dx}}\,, \end{aligned}$$

or by integrating

$$\begin{aligned} \hat{T}_1 : \quad & \underline{\mathbf{x}} \to -\underline{\mathbf{x}} + \underline{\mathbf{x}}_0 \quad & t \to t + \tau \\ \hat{T}_2 : \quad & t \to -t + t_0 \quad & \underline{\mathbf{x}} \to \underline{\mathbf{x}} + \underline{\chi}\,. \end{aligned}$$

We will now apply these transformations to the Langevin equation in order to determine the regimes for which transport is forbidden. In the following symmetry analysis we drop the noise term $\underline{\xi}$ from the Langevin equation, as it is symmetric Gaussian noise and so should not contribute to the long-time macroscopic drift velocity.

The $\hat{T}_1$ transformation and "shift-symmetry"

Applying the $\hat{T}_1$ transformation

$$\hat{T}_1 : \qquad \underline{\mathbf{p}} \to -\underline{\mathbf{p}} \qquad \underline{\mathbf{x}} \to -\underline{\mathbf{x}} + \underline{\mathbf{x}}_0 \qquad t \to t + \tau$$

to the Langevin equation

$$\begin{gathered} \dot{\underline{\mathbf{p}}} = -\frac{\gamma}{m}\underline{\mathbf{p}} - \underline{\mathbf{U}}'(\underline{\mathbf{x}}) + \underline{\mathbf{f}}(t) \\ \hline \longrightarrow -\dot{\underline{\mathbf{p}}} = -\frac{\gamma}{m}\left(-\underline{\mathbf{p}}\right) + \underline{\mathbf{U}}'(-\underline{\mathbf{x}} + \underline{\mathbf{x}}_0) + \underline{\mathbf{f}}(t+\tau) \\ \dot{\underline{\mathbf{p}}} = -\frac{\gamma}{m}\underline{\mathbf{p}} - \underline{\mathbf{U}}'(-\underline{\mathbf{x}} + \underline{\mathbf{x}}_0) - \underline{\mathbf{f}}(t+\tau)\,. \end{gathered}$$

Using the fact that the optical potential is spatially symmetric $\underline{\mathbf{U}}'(-\underline{\mathbf{x}} + \underline{\mathbf{x}}_0) = \underline{\mathbf{U}}'(\underline{\mathbf{x}})$, a condition on the driving is obtained:

$$\underline{\mathbf{f}}(t+\tau) = -\underline{\mathbf{f}}(t)\,.$$

Applying the transformation twice gives $\underline{\mathbf{f}}(t+2\tau) = \underline{\mathbf{f}}((t+\tau)+\tau) = -\underline{\mathbf{f}}(t+\tau) = \underline{\mathbf{f}}(t)$. From this fact that $\underline{\mathbf{f}}(t+2\tau) = \underline{\mathbf{f}}(t)$ it is deduced that $\tau = T/2$ where T is the characteristic time-period of the driving.

So the condition for the system to be symmetric under the $\hat{T}_1$ transformation is that the driving has the form

$$\underline{\mathbf{f}}\,(t+T/2) = -\underline{\mathbf{f}}\,(t)\,. \tag{2.2}$$

When the driving has this property we say the driving possesses "shift-symmetry".

The $\hat{T}_2$ transformation and "time-reversal symmetry"

Applying the $\hat{T}_2$ transformation

$$\hat{T}_2: \qquad \underline{\mathbf{p}} \to -\underline{\mathbf{p}} \qquad t \to -t + t_0 \qquad \underline{\mathbf{x}} \to \underline{\mathbf{x}} + \underline{\chi}$$

to the Langevin equation

$$\begin{gathered} \underline{\dot{\mathbf{p}}} = -\frac{\gamma}{m}\underline{\mathbf{p}} - \underline{\mathbf{U}}'\,(\underline{\mathbf{x}}) + \underline{\mathbf{f}}\,(t) \\ \hline \longrightarrow \underline{\dot{\mathbf{p}}} = -\frac{\gamma}{m}\left(-\underline{\mathbf{p}}\right) - \underline{\mathbf{U}}'\left(\underline{\mathbf{x}} + \underline{\chi}\right) + \underline{\mathbf{f}}\,(-t + t_0)\,. \end{gathered}$$

To simplify this consider first the dissipationless case of a Hamiltonian ratchet where the damping term is zero. The following condition on the driving is then obtained:

$$\underline{\mathbf{f}}\,(-t + t_0) = \underline{\mathbf{f}}\,(t)$$

for the system to be invariant under the $\hat{T}_2$ transformation. When the driving obeys the above condition we say it possesses "time-reversal symmetry".

When the driving possesses shift-symmetry or time-reversal symmetry then transport is forbidden.

We now consider specific forms of the driving, and the conditions for them to be shift-symmetric and time-reversal symmetric.

2.4.2 Specific forms of driving $f(t)$

Single harmonic driving

Consider a periodic drive consisting of a single harmonic $f(t) = \cos(\omega t + \phi)$. The driving is shift-symmetric ($f(t + T/2) = -f(t)$) for all ϕ because $\cos(\omega(t + T/2) + \phi) = \cos(\omega t + \phi + \pi) = -\cos(\omega t + \phi)$. Therefore transport is forbidden for this form of driving for all values of phase ϕ.

The situation changes, however, when we add an additional harmonic to form the biharmonic drive.

Biharmonic driving

Consider a general periodic driving force formed from the sum of two harmonics

$$f(t) = A\left[\cos(\omega_1 t) + \epsilon\cos(\omega_2 t + \phi)\right].$$

The frequency ratio can be written as $\frac{\omega_2}{\omega_1} = \frac{p}{q}$, where p and q are two co-prime integers (ie: they share no common factors).

Since, by definition, $\omega_1 = \frac{2\pi}{T_1}$ and $\omega_2 = \frac{2\pi}{T_2}$, then we have $\frac{p}{q} = \frac{\omega_2}{\omega_1} = \frac{T_1}{T_2}$ and so $qT_1 = pT_2 = T$, where T is the characteristic time-period of the driving.

We now look for when the driving is shift-symmetric such that $f(t+T/2) = -f(t)$. We have

$$\begin{aligned} f(t+T/2) &= A\left[\cos(\omega_1(t+T/2)) + \epsilon\cos(\omega_2(t+T/2)+\phi)\right] \\ &= A\left[\cos(\omega_1 t + q\omega_1 T_1/2) + \epsilon\cos(\omega_2 t + p\omega_2 T_2/2 + \phi)\right] \\ &= A\left[\cos(\omega_1 t + q\pi) + \epsilon\cos(\omega_2 t + p\pi + \phi)\right]. \end{aligned}$$

We see that if p and q are both odd, then $f(t+T/2) = -f(t)$ and the driving is shift-symmetric. So no transport can occur if p and q are both odd. Since we know that p and q aren't both even, as they were defined as co-prime, we can determine that p and q must have opposite parity in order for the shift-symmetry to be broken.

Let us now consider when the driving is time-reversal symmetric such that $f(-t+\tau) = f(t+\tau)$ for some time τ, which is exactly equivalent to $f(-t+\tau) - f(t+\tau) = 0$.

$$\begin{aligned} f(-t+\tau) &= A\left[\cos(-\omega_1 t + \omega_1\tau) + \epsilon\cos(-\omega_2 t + \omega_2\tau + \phi)\right] \\ &= A\left[\cos(\omega_1 t - \omega_1\tau) + \epsilon\cos(\omega_2 t - \omega_2\tau - \phi)\right] \end{aligned}$$

and

$$f(t+\tau) = A\left[\cos(\omega_1 t + \omega_1\tau) + \epsilon\cos(\omega_2 t + \omega_2\tau + \phi)\right].$$

Subtracting the two equations gives us terms like $\cos(\alpha-\beta) - \cos(\alpha+\beta)$ for which we can substitute $2\sin(\alpha)\sin(\beta)$ to get:

$$f(-t+\tau) - f(t+\tau) = 2A\left[\sin(\omega_1 t)\sin(\omega_1\tau) + \epsilon\sin(\omega_2 t)\sin(\omega_2\tau+\phi)\right] = 0.$$

Since the time-reversal symmetry must hold for all time t we have the conditions $\sin(\omega_1\tau) = 0$ and $\sin(\omega_2\tau+\phi) = 0$ and therefore

$$\begin{aligned} \omega_1\tau &= m\pi \\ \omega_2\tau + \phi &= m'\pi \end{aligned}$$

for integers m, m'. Substituting $\omega_2\tau = \frac{p}{q}\omega_1\tau = \frac{p}{q}m\pi$ into the second line and multiplying through by q gives the condition:

$$q\phi = \overbrace{(qm' - pm)}^{integer}\pi = n\pi\,. \tag{2.3}$$

Therefore, the driving is time-reversal symmetric when $q\phi = n\pi$ for n integer, and we expect to see no transport at these values of ϕ. This suggests that a function describing the transport $v_c(\phi)$ will have zeros at $q\phi = n\pi$, which implies that the velocity measurements will have some periodic structure corresponding to the time-reversal symmetry breaking governed by ϕ.

We note that if the first harmonic had a phase ϕ_1, then the conditions would become

$$\begin{aligned}\omega_1\tau + \phi_1 &= m\pi \\ \omega_2\tau + \phi_2 &= m'\pi\,.\end{aligned}$$

Upon substituting $\omega_2\tau = \frac{p}{q}\omega_1\tau = \frac{p}{q}m\pi - \frac{p}{q}\phi_1$, we would get the condition:

$$q(\phi_2 - \frac{p}{q}\phi_1) = q\phi_r = n\pi\,, \tag{2.4}$$

where we have defined the relative phase $\phi_r = \phi_2 - (p/q)\phi_1$. Therefore, we see that the time-reversal symmetry condition of $q\phi = n\pi$ applies to the relative phase. Usually we take $\phi_1 = 0$ so that the relative phase is determined by ϕ_2.

The role of dissipation

When deriving the condition for the time-reversal symmetry to hold, the friction term that expresses the dissipation in the system was neglected. Therefore the above results apply to the dissipationless Hamiltonian regime. When dissipation is introduced to the system it breaks the time-reversal symmetry, and so transport should be expected even when $q\phi = n\pi$.

Theoretical work in this field [24, 89] has demonstrated that the introduction of dissipation results in an additional phase-shift θ_0 on the resultant current, meaning that the condition for time-reversal symmetry to hold becomes $q\phi + \theta_0 = n\pi$. This additional phase-shift can be used to characterise the degree of dissipation in the system [27].

The two-dimensional case

The derivations of the symmetry conditions were vector equations, meaning that each component of the vector must satisfy the conditions independently. If a particular component does not satisfy the shift-symmetry condition then the symmetry is broken along that direction, while the other direction might retain its shift symmetry.
Explicitly, the requirement for the shift-symmetry to hold is

$$f_x(t + T/2) = -f_x(t)$$
$$f_y(t + T/2) = -f_y(t),$$

where we can see that the symmetries for each direction appear to be decoupled (that is f_x does not depend on f_y and vice-versa). There is one connecting factor that prevents the vector components being entirely decoupled, however, and that is the time-period T appearing in both transformations. This T represents the characteristic time-period for the entire vector driving force $\underline{\mathbf{f}}(t)$, and so depends on both components. It is the lowest common multiple of the time-periods of each driving frequency, and it represents the time at which the summed waveform starts repeating itself. The various time-periods associated to a biharmonic driving are portrayed in figure 2.4.

To elaborate on this point, let us consider the case of a split-biharmonic driving of the form

$$f_x(t) = A_x \cos(\omega_1 t)$$
$$f_y(t) = A_y \cos(\omega_2 t + \phi),$$

where $\omega_2/\omega_1 = p/q$. In this case the time-period of the entire driving is given by $T = q\,T_1 = p\,T_2$. Applying the shift-symmetry transformation gives:

$$f_x(t + T/2) = A_x \cos(\omega_1 t + q\pi)$$
$$f_y(t + T/2) = A_y \cos(\omega_2 t + p\pi + \phi).$$

If both p and q are odd then the shift-symmetry holds, but if either of them are even then the shift-symmetry is broken along that direction and transport can occur along that direction. Even though the driving component along each direction is a single harmonic, which was shown to always retain shift-symmetry, transport still occurs because the time-period T appearing in the shift-symmetry condition is determined by both components in conjunction. This is the coupling between the transverse degrees of freedom that is explored later in the thesis, specifically in chapter 6.

The quasiperiodic case

The previous section highlighted that the key to coupling comes from the same overall time-period T applying to the different directions. This means that

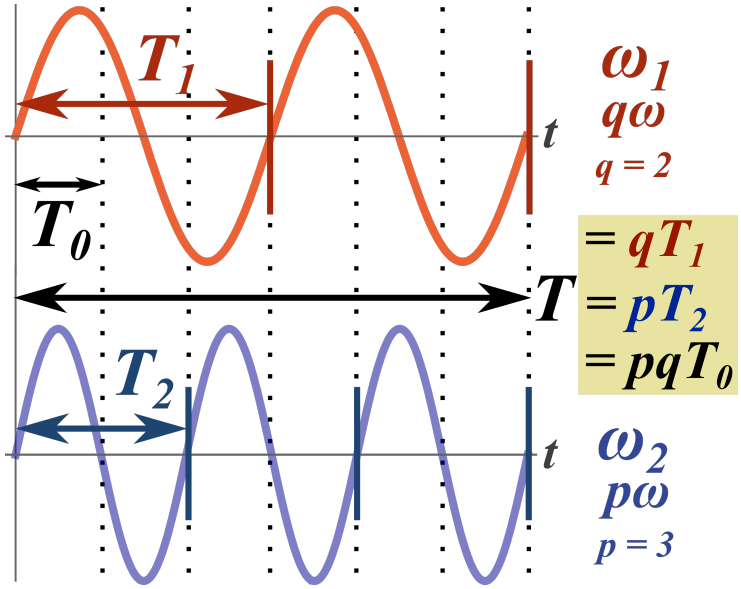

Figure 2.4: The various time-periods associated to a typical biharmonic driving. Each harmonic has an associated time-period T_1 and T_2, which comes from the fundamental relation $T_i = 2\pi/\omega_i$. Then there is the overall time-period T, which represents the time for the entire summed waveform to start repeating. It is the lowest common multiple of T_1 and T_2 and is the time-period relevant for the shift-symmetry condition. Yet another time-scale is T_0 – the highest common factor of T_1 and T_2 – which represents the time 'unit' that fits into both T_1 and T_2 by an integer multiple.

even though the shift-symmetry applies to each direction independently, they are still coupled via this time-period T. When we make the driving frequencies quasiperiodic something rather interesting happens. Since quasiperiodity increases the number of degrees of freedom in the system [52, 14, 9], there now exists two effectively independent variables $\Psi_1 = \omega_1 t$ and $\Psi_2 = \omega_2 t$.

The shift-symmetry condition is then modified so that it is a function of the two phases Ψ_1, Ψ_2, ie: $\underline{\mathbf{f}}(t)$ becomes $\underline{\mathbf{f}}(\Psi_1, \Psi_2)$. Then the shift-symmetry condition becomes

$$\underline{\mathbf{f}}(\Psi_1 + \Psi_1^{(0)}, \Psi_2 + \Psi_2^{(0)}) = -\underline{\mathbf{f}}(\Psi_1, \Psi_2).$$

Applying this twice gives the condition

$$\underline{\mathbf{f}}(\Psi_1 + 2\Psi_1^{(0)}, \Psi_2 + 2\Psi_2^{(0)}) = \underline{\mathbf{f}}(\Psi_1, \Psi_2),$$

and since the Ψ's represent phase, which is 2π periodic, then it is possible to identify $\Psi_1^{(0)} = \Psi_2^{(0)} = \pi$ and the shift-symmetry condition is

$$\underline{\mathbf{f}}(\Psi_1 + \pi, \Psi_2 + \pi) = -\underline{\mathbf{f}}(\Psi_1, \Psi_2).$$

In our specific case of the split-biharmonic driving expressed in terms of the Ψ_1 and Ψ_2

$$f_x(\Psi_1) = A_x \cos(\Psi_1)$$
$$f_y(\Psi_2) = A_y \cos(\Psi_2 + \phi),$$

the shift-symmetry condition $\underline{\mathbf{f}}(\Psi_1 + \pi, \Psi_2 + \pi) = -\underline{\mathbf{f}}(\Psi_1, \Psi_2)$ is always satisfied, which means that transport is always forbidden when ω_2/ω_1 is irrational for the split-biharmonic driving.

To summarise, in the quasiperiodic regime, when ω_2/ω_1 is irrational, the variables $\Psi_1 = \omega_1 t$ and $\Psi_2 = \omega_2 t$ are treated as independent variables, which increases the number of degrees of freedom - or dimensionality - of the system; from a single time variable to two incommensurate phase variables. This means that the shift-symmetry condition, which was $\underline{\mathbf{f}}(t + T/2) = -\underline{\mathbf{f}}(t)$ for commensurate frequencies, is modified to $\underline{\mathbf{f}}(\omega_1 t + \pi, \omega_2 t + \pi) = -\underline{\mathbf{f}}(\omega_1 t, \omega_2 t)$ for incommensurate frequencies. In the specific case of the split-biharmonic driving this condition is always satisfied and so it is concluded that transport is forbidden for split-biharmonic driving in the quasiperiodic regime.

This increase in the dimensionality of the system is entirely analogous to the situation we came across in the introduction, with the right-angled triangle having sides of length 1 and $\sqrt{2}$. There it was shown that we can not use a single ruler to measure both sides, but instead would need two incommensurable rulers. This amounts to an increase in the number of degrees of freedom needed to fully represent the system. With commensurate magnitudes we can use a single parameter – the single ruler, or shared time variable – but with incommensurate magnitudes we require two independent parameters – two rulers, or two time-dependent phases. Since, in the case of our driving field, the single time-variable couples the x and y directions, when the dimensionality of the system is increased the x and y directions acquire their own independent phase parameters and so become decoupled. This decoupling has a discernible impact on the dynamics of the split-biharmonic drive, which relies on the coupling in order to produce transport. This is explored further in chapter 6.

Chapter 3

Experimental Set-up

This chapter describes the experimental set-up used to produce and measure the ratchet effect with cold caesium atoms in a two-dimensional dissipative optical lattice.

It begins by describing the vacuum, laser and magnetic systems used to obtain a cloud of cold atoms. It then describes the optical lattice set-up and corresponding modulation control, which supplies the driving forces for the ratchet. Finally a brief outline of the experimental procedure is given.

3.1 The science chamber

The ultra-high vacuum chamber was inherited from a previous experiment [86]. The basic structure is depicted in figure 3.1 but a more detailed and, dare I admit, attractive diagram of the vacuum chamber can be found in [86], figure 3.2 on page 40. The main chamber has eight 1 inch viewports around the circumference and two large 8 inch viewports on the faces. Through the four pairs of 1 inch viewports and the two large viewports there are passed the retro-reflected MOT beams, the repumper beam, and the three lattice beams orientated at 120° to each other. In addition to this, a camera with an objective lens is positioned to observe the atomic cloud.

Our experiment uses caesium-133 alkali metal element, for which the energy level structure of the caesium D_2 line at 852 nm is displayed in figure 3.2.

Another popular alkali metal is rubidium, which comes in two isotopes (^{87}Rb and ^{85}Rb) both of which are used extensively in laser cooling experiments. Rubidium-87 is used by our group at UCL on a separate Bose-Einstein Condensation (BEC) experiment, and was also the element of choice for the NPL atomic fountain that I had the privilege of working on and is described in the final chapter of this thesis.
There is wisdom in choosing rubidium over caesium for a BEC experiment and for an atomic fountain clock, and this is due to the smaller collisional cross-

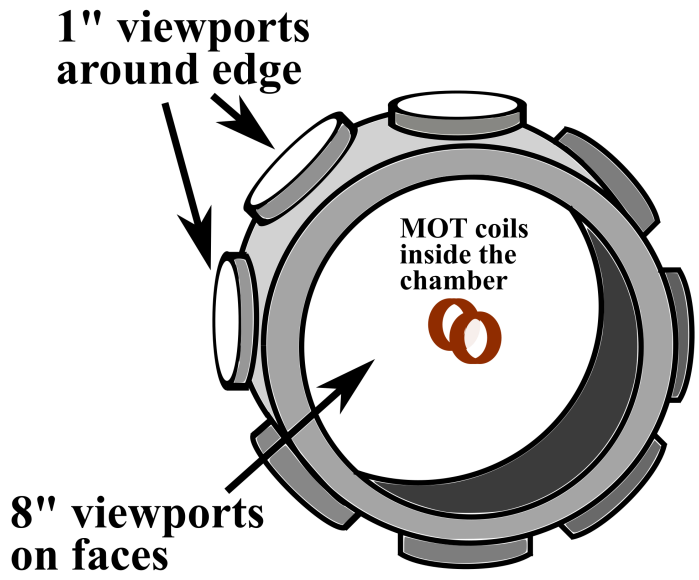

Figure 3.1: A sketch of the vacuum chamber showing the general layout of the viewports as well as the representative size and position of the pair of anti-Helmholtz coils that are fixed inside the vacuum chamber.

section of rubidium compared to caesium. For the purposes of producing a BEC, where atomic collisions contribute to heating the atomic cloud, and for an atomic clock, where collisions produce a frequency shift, it is preferable to have a smaller collisional cross-section. In our experiment we are not seeking the low temperatures required by a BEC nor the precision promised by an atomic clock, so it was sufficient to use caesium atoms.
The caesium is provided to our system using alkali-metal dispensers from SAES getters. These consist of metal doped with caesium such that by running current through the dispenser it is heated and the caesium atoms are released as vapour in a controllable manner. There is also an ion-pump[1] connected to the chamber in order to maintain the ultra-high vacuum. The operating pressure within the chamber is deduced from the electrical current reading produced by the ion-pump, which in our case indicates a pressure below 10^{-8} mbar.

3.2 Magneto-optical trap system

This section describes the laser and magnetic coil systems used to produce the magneto-optical trap (MOT) of caesium atoms.

[1]Varian (now Agilent) *VacIon Plus* 20 *Starcell*, 20 litre/second ion-pump

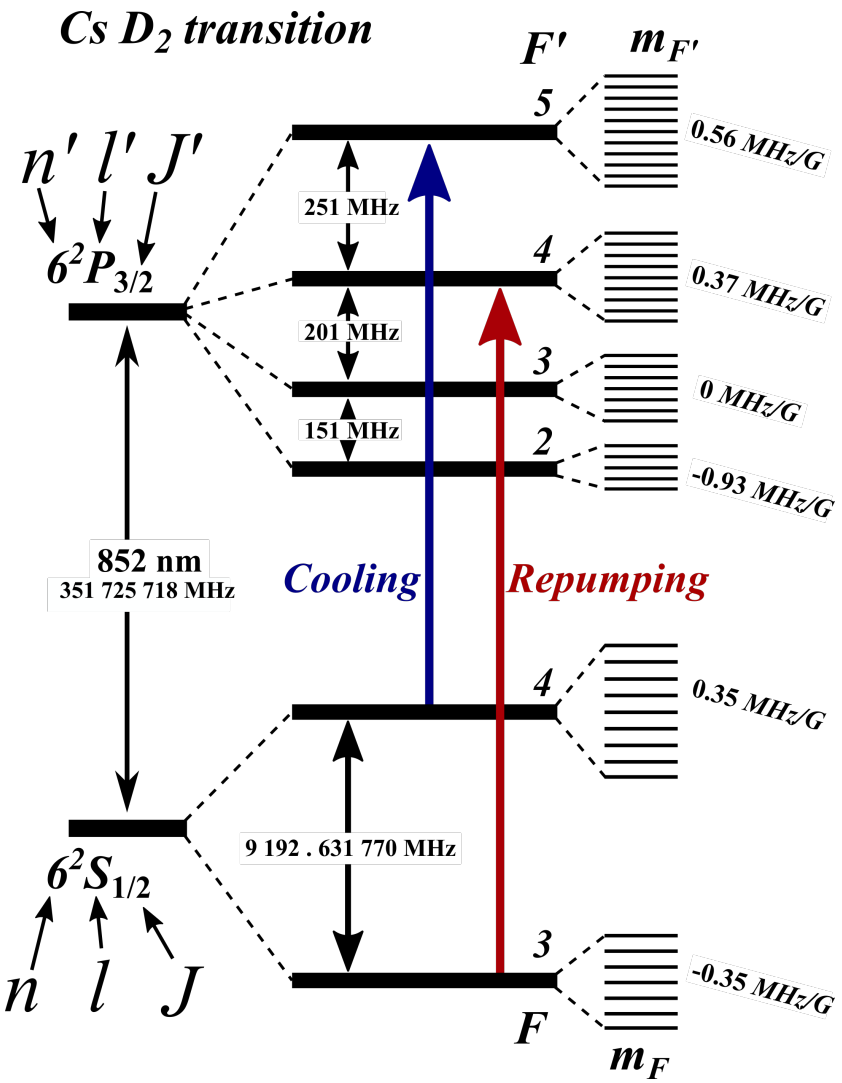

Figure 3.2: The caesium D_2 line at 852 nm, showing the cooling and repumping transitions. This image was inspired by Daniel Steck's caesium D-line data [78], and the values were taken from that paper.

3.2.1 External cavity diode lasers

The lasers used in our experiment are home-built external cavity diode lasers (ECDLs) in the Littrow configuration [70], as depicted in figure 3.3. In this configuration the light from the laser-diode is incident on a diffraction grating several centimetres away. The zeroth-order diffracted beam is reflected back into the laser-diode, effectively creating an extended cavity, and the first order is diffracted to be used in the experiment. The benefit of having this extended cavity is a reduction in the linewidth of the laser light. Our ECDLs

were previously measured [60] to have a linewidth of less than 300 kHz when locked, which can be compared to the natural linewidth of the cooling transition $\Gamma = 5.22\,\text{MHz}$. Comparing the natural linewidth of 5.22 MHz to the lasing frequency of 351 THz (corresponding to 852 nm) reveals just how precisely tuned the laser frequency must be in order to be on resonance with the transition. Such fine tuning is analogous to a positional accuracy of a hair's breadth over five kilometres! Alternatively, if the excited state linewidth as shown in figure 3.2 were to scale (ie: 2 mm = 5.22 MHz), then the page would need to extend 135 km in order to accommodate the ground-state line – a proposition that my bookbinder will surely refuse.

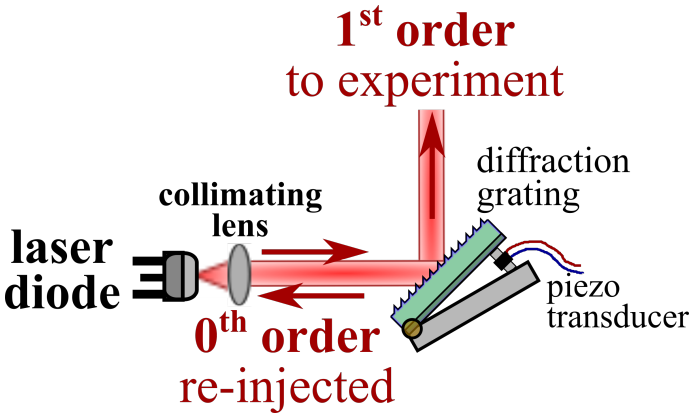

Figure 3.3: An external cavity diode laser in the Littrow configuration. Light from the laser-diode is incident on a holographic diffraction grating that has an angle controlled by a piezo transducer. The zeroth-order diffracted beam allows the formation of an extended optical cavity, and the first-order diffracted beam is used for the experiment.

The frequency of the zeroth-order re-injected light is determined by the angle of the diffraction grating. For our lasers this angle is controlled by a piezo transducer and modulation of the laser frequency can be achieved by modulating the piezo about some prescribed value. The temperature also affects the lasing frequency and so the entire system sits on a platform above a peltier element, which has its temperature carefully stabilised by a PID[2] controller.

3.2.2 Cooling light

The cooling light is used to drive the cycling transition $F = 4 \rightarrow F' = 5$. This transition has a high probability of decaying back to the $F = 4$ ground-state, for the process of absorption and emission to repeat.

[2]PID stands for **P**roportional-**I**ntegral-**D**erivative, representing the three feedback mechanisms used for stabilisation.

Our cooling laser system is in a so-called 'master-slave' configuration. In this scheme, one laser (the master) has its light injected into another laser (the slave). If properly injected, the slave laser's emission follows the frequency distribution of the master laser. Contrary to conventional master-slave relationships, it is in fact the slave that has more power than the master. The master only governs the slave's frequency.
Our master laser is a low power ($\approx 20\,\mathrm{mW}$ at output) diode[3] laser in the Littrow configuration (as described above). The laser emission has an elliptical cross section, so a pair of anamorphic prisms is used to shape the beam and achieve a circular cross section. An anamorphic prism pair is used to expand (or reduce) the beam in one dimension, with the magnification being dependent on the angle of incidence of the incoming beam. By a suitable configuration of the prisms, one can produce a circular collimated beam. The anamorphic prism pair works just like a cylindrical lens telescope but it has a couple of advantages, which are that it is compact and it is easily adjustable. The latter is a significant advantage for the long-term, spanning laser diode lifetimes and generations, since separate laser diodes tend to have different elliptical eccentricities and so the same anamorphic prism pair can simply be re-adjusted for each laser diode.

After this shaping the beam is passed through an optical isolator, which is used to prevent back-scattered light from re-entering the laser cavity as this optical feedback reduces the stability of the laser lock.

The beam is then split using a half-wave plate (HWP) and polarising beam-splitter (PBS), a small portion for the spectroscopy and locking, and the rest is passed through an acousto-optic modulator (AOM) in the double-pass configuration. This AOM is used as the main frequency control of the cooling laser, as the double-pass configuration permits us to change the frequency of the beam without worrying about the corresponding change in beam angle.

The set-up of the double-pass configuration has a few subtleties, which are depicted in figure 3.4 and are described next. Firstly, we require a system where the output beam does not change position, even though there is a frequency change and corresponding change in angle of the diffracted beam. This is achieved by suitably positioning a lens and a mirror to reflect the light back through the AOM. The lens is positioned at a distance equal to its focal length away from the AOM. In this way, an angular shift in the beam is translated into a parallel shift after the lens. The light is then reflected directly back through this lens, which focusses it back into the AOM where it undergoes a second frequency shift. The twice diffracted beam exits the AOM such that it is counter-propagating over the original input beam. What now remains is to separate the input beam and the frequency-shifted output beam. This is done neatly by using a polarising beam-splitter before the AOM and a quarter-wave plate (QWP) after it, such that the reflected light has a

[3]Hitachi *HL8342-MG*, 852 nm, 50 mW laser-diode

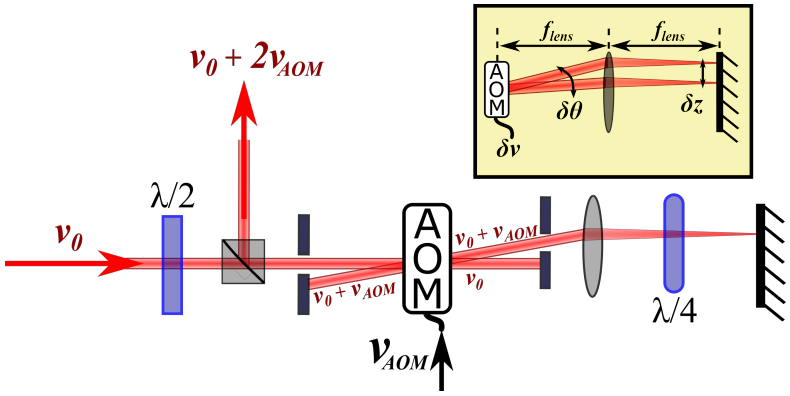

Figure 3.4: The configuration of the double-pass AOM setup. The outgoing beam is frequency-shifted twice by the AOM and filtered out using a HWP/PBS pair and two passes through the QWP. The **inset** shows how a change in AOM frequency produces a lateral shift after the lens. By appropriate positioning of the lens and mirror, the beam remains collimated and its output path unchanged with changes in AOM frequency.

polarisation that is orthogonal to the original beam, and so is separated by the polarising cube. An additional benefit gained from using the double-pass configuration is that it effectively doubles the AOM's bandwidth, meaning a larger range of detunings is available.

After passing through the double-pass AOM, the light is injected into two slave lasers, one for the MOT beams and one for the lattice beams. This is achieved by feeding light through the input polariser of the slave lasers' respective optical isolators. This light is then incident directly onto the slave laser diodes, causing them to be injection-locked to the master laser. The slave laser[4] has higher power (around 70 mW at output), which is reserved entirely for the experiment, as opposed to the master laser power, which was reduced essentially by its use in spectroscopy and by passing it through the double-pass AOM.

The light from the MOT slave laser then passes through an AOM (in single-pass), which holds a fixed frequency of 80 MHz and is used for the purpose of intensity control and fast-switching of the MOT beams. This AOM sits at the focal point of a telescope system that magnifies the beam to approximately $\frac{1}{2}$cm $1/e^2$ beam diameter. This beam is then split into three beams using two HWP/PBS pairs, to form the three retro-reflected MOT beams. Each of the MOT beams pass through a QWP in order to establish their circular polarisations and a QWP is also positioned in front of each of

[4] *SDL-5422-H1*, 852 nm, 100 mW laser diode

the retro-reflecting mirrors such that the counter-propagating MOT beams are orthogonally polarised. The orientation of the retro-reflected beams through the science chamber is depicted in figure 3.5. Each MOT beam has a power of around 5 mW at the chamber, producing an intensity of approximately 13 mW/cm^2 per beam. The beams are red-detuned by $2\,\Gamma$ ($2\pi \cdot 10.5$ MHz) from the cooling transition.

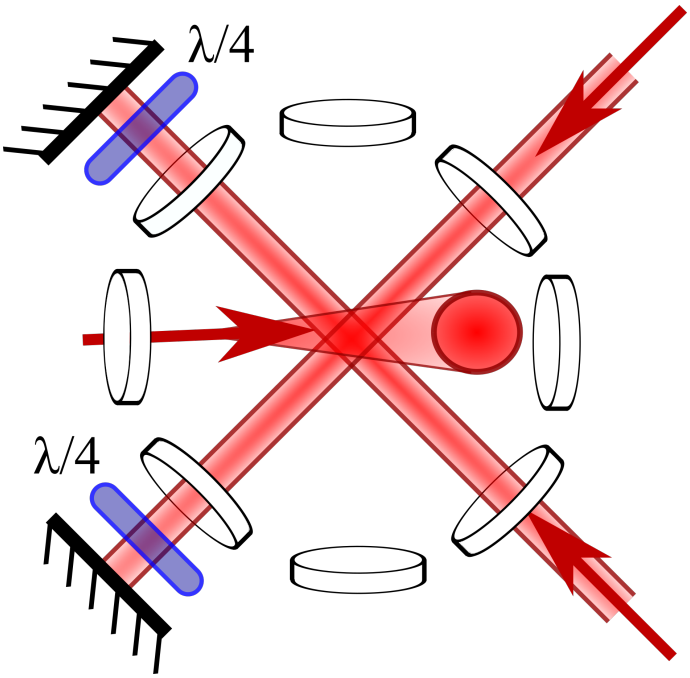

Figure 3.5: The orientation of the three retro-reflected MOT beams passing through the vacuum chamber. The beam protruding from the page has been orientated so that it doesn't hit the reader in the eye.

DF-DAVLL locking

The cooling light is locked to the $F = 4 \rightarrow F' = 4/5$ cross-over transition, using a DF-DAVLL[5] locking technique. In this scheme, linearly-polarised light is incident on a caesium vapour cell in the presence of a magnetic field. This linear polarisation can be decomposed into σ^+ and σ^- circular polarisation components of equal magnitude. In the presence of the magnetic field the Zeeman sub-states are perturbed and consequently the absorption spectra for the two polarisation components exhibit a relative shift to one another. When the light is decomposed and the two spectra are subtracted there is a zero-crossing about the unperturbed frequency, which can be electronically locked to. This is represented in figure 3.6.

[5]DF-DAVLL stands for **D**oppler-**F**ree **D**ichroic **A**tomic **V**apour **L**aser **L**ock

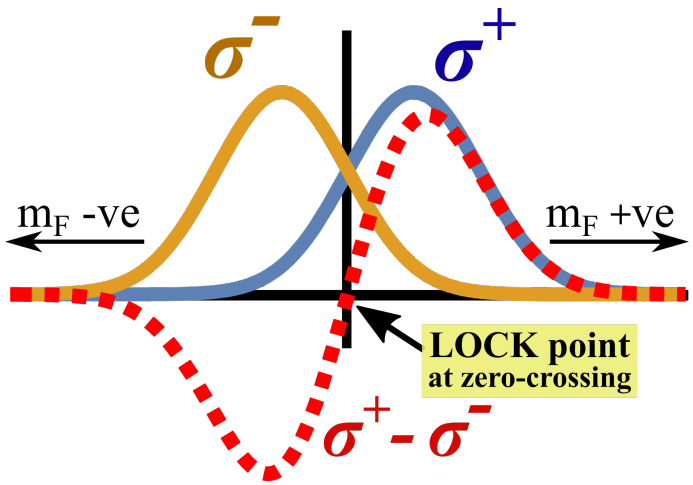

Figure 3.6: Principle of the DF-DAVLL locking technique. In the presence of a magnetic field, the spectra for σ^+ and σ^- light are shifted with respect to each-other due to the Zeeman shift of the magnetic sub-levels. Since the shifts are symmetric about the centre frequency, subtracting the signals gives a zero-crossing at the required transition frequency.

Our DF-DAVLL set-up is rather unique in that instead of a solenoid, permanent neodymium magnets are used to produce the magnetic field. The use of permanent magnets has several advantages over using solenoids: firstly the permanent magnets are cheap, compact, and do not entail the tedious task of winding a coil. Also, being fixed magnets, they do not consume power and don't require a power supply, which are often in high demand in an experimental physics lab. Another benefit is that they are not dependent on the stability of the electrical supply. This is particularly beneficial for the DF-DAVLL locking, where the stability of the magnetic field affects the stability of the laser lock.

Since the light from the master laser is locked to the $F = 4 \rightarrow F' = 4/5$ cross-over transition, which is 125 MHz below the cooling transition, this light must be brought closer to resonance. For this purpose AOMs are used in order to provide the fine-tuning frequency shifts. The frequency tuning of the AOMs used in this experiment with respect to the hyperfine energy levels is shown in figure 3.7.

3.2.3 Repumper system

For the cooling beam we use the cycling transition $F = 4 \rightarrow F' = 5$, which decays mostly to the $F = 4$ ground-state, but it also has a likelihood to decay to the $F = 3$ ground-state. It is a small probability but nonetheless, with

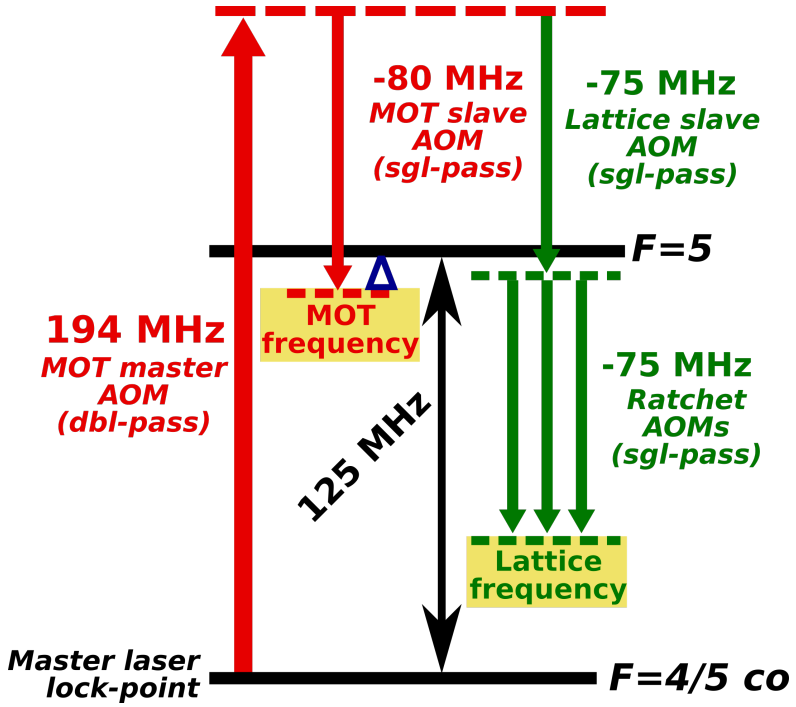

Figure 3.7: The laser frequencies in relation to the atomic hyperfine transition frequencies, showing how the AOMs in the experiment are used to shift the frequency of the light and bring it to our desired detunings for the MOT and lattice.

millions of atoms and millions of Rabi cycles per second, this small probability becomes a considerable factor. This $F = 3$ ground-state is transparent to our cooling laser and so, with just the cooling light on, all of the atoms soon decay into this invisible state and stop being cooled. In order to address this problem we introduce another laser, the aptly named repumping laser, which pumps atoms from $F = 3 \rightarrow F' = 4$, which then decays to the $F = 4$ ground-state and back into the cooling cycle.
The repumper laser is a home-built ECDL laser, similar to the master laser.

3.2.4 Magnetic coils

There are two sets of magnetic coils in our experiment – the MOT coils and the compensation coils. The MOT coils produce the magnetic field necessary to trap the atoms. The compensation coils are used to counter the Earth's magnetic field in the vicinity of the chamber, so that the magnetically sensitive states of the atom aren't affected by it.

MOT coils

The MOT coils are a pair of coils in the so-called anti-Helmholtz configuration. The anti-Helmholtz configuration constitutes two identical coils facing each other, separated by a distance equal to their radius, with the same current flowing through them but in opposite directions (clockwise/anti-clockwise) as illustrated in figure 3.8. Since the direction of current flow determines the parity of the magnetic field, and their magnitudes are equal, it can be observed by symmetry that the total magnetic field must be zero at the centre between the coils. Since atoms in the MOT are trapped at the magnetic field minimum, the MOT trapping centre corresponds to the geometrical centre between the coil pair. In the vicinity around the MOT centre, the gradient of the magnetic field is approximately linear. The magnetic field gradient depends on the radius of the coils (1 inch in our case), the number of turns (approximately 80), and the current supplied to the coils (typically 1 amp). This produces a magnetic field gradient of approximately 13 G/cm at the centre between the coils.

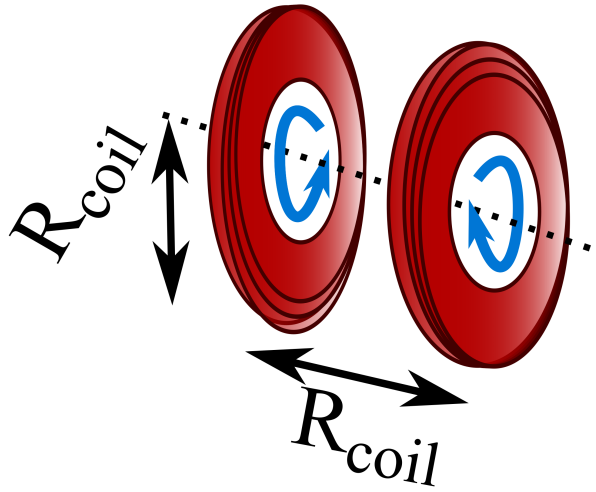

Figure 3.8: The MOT coil anti-Helmholtz configuration, where the coils are separated by a distance equal to their radius and the same current is flowing through them but in opposite directions.

The MOT coil pair are connected in series (to ensure equal current in both coils) and are connected to a power supply via a MOSFET[6] box, which permits us to regulate the current flowing to the coils by a control (gate) voltage. This control voltage is set through the computer, so this MOSFET box acts as our interface between the computer and the MOT field strength. Since the MOSFET chip can be used for switching high current loads, it sits

[6]MOSFET stands for **M**etal-**O**xide-**S**emiconductor **F**ield-**E**ffect **T**ransistor

on a metal plate that is water-cooled. The MOSFET box was used as it was already implemented in the set-up from the previous experiment [86], but just as effective for our purposes is a solid-state relay (SSR) switch, which was in fact used during the initial stages of the experiment. The SSR switch is a triggerable switch allowing on-off switching of the coil current, but not control of the actual current magnitude.

Compensation coils

The compensation coils are used to reduce the effect of the Earth's magnetic field so that the magnetically sensitive Zeeman sub-states aren't affected by it. Coils in the Helmholtz configuration are used to provide a magnetic field strength equal and opposite to the Earth's magnetic field. The Helmholtz configuration is the same as the anti-Helmholtz configuration but the current is flowing through the coils in the *same* direction. This provides an approximately constant magnetic field offset in the space between the coils. By forming a cube with three pairs of coils, each independently controlled by a separate power supply, one is able to compensate for Earth's magnetic field in all three dimensions of space. The compensation coil arrangement is illustrated in figure 3.9.

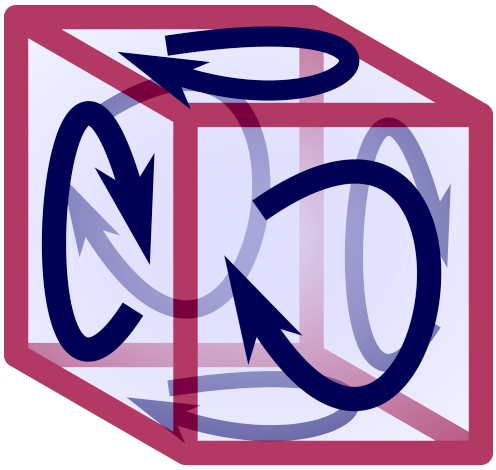

Figure 3.9: The compensation coil Helmholtz configuration, where there is a pair of coils for each dimension of space, forming a cube. Each pair has the same current flowing in the same direction, which provides an approximately constant offset field in the cube's interior to compensate for Earth's magnetic field.

Since each coil is controlled independently by a separate power supply, it is non-trivial finding the optimal setting to absolutely compensate the Earth's magnetic field. There are certain methods we can employ, but none of them provide the prime solution. On the up-side, since the Earth's magnetic field

doesn't vary substantially for a given location, once the prime settings are found they generally remain set and unchanged.

3.2.5 MOT temperature measurements

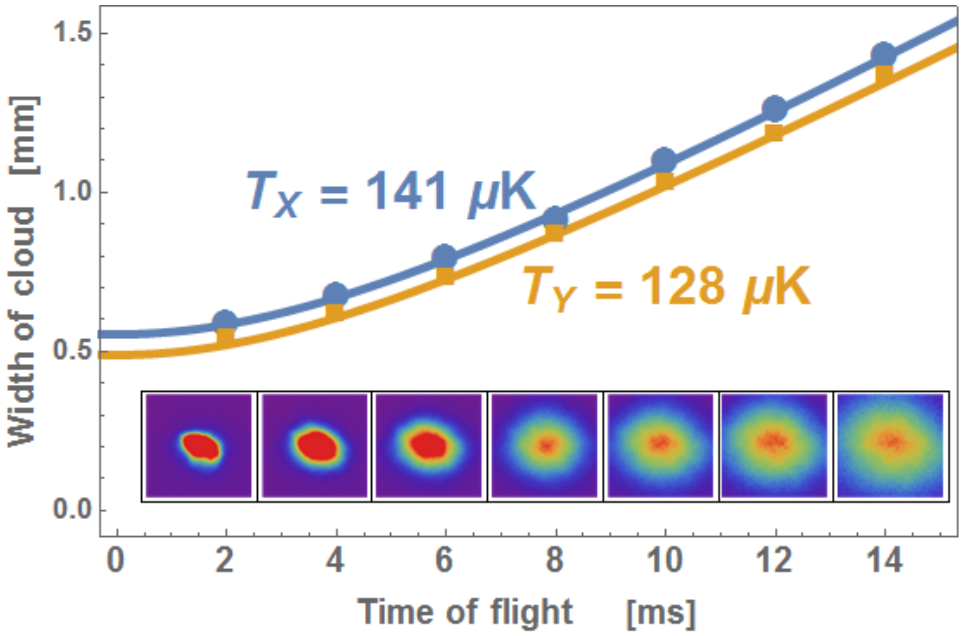

Figure 3.10: Time-of-flight imaging of the atoms in the MOT. The temperature of the cloud in the x and y direction is extracted by fitting the width of the cloud to equation 3.1.

The temperature of atoms in the MOT can be measured using time-of-flight imaging, where atoms in the MOT are left to freely diffuse for a specified time and the width of the atomic cloud is measured. The width of an atomic cloud in free diffusion is presumed to evolve according to $\sigma(t)^2 = \sigma_0^2 + v_{rms}^2\, t^2$, where σ represents the width (standard deviation) of a Gaussian distributed cloud of atoms (σ_0 being the initial width), v_{rms} is the root-mean-squared velocity of the atoms presumed to obey Maxwell-Boltzmann statistics, and t is the free diffusion time (the time-of-flight). The temperature of the atoms is related to the root-mean-squared velocity by $k_B T = m v_{rms}^2$, where k_B is the Boltzmann constant and m is the atomic mass (of caesium in our case), and so the width of the cloud evolves according to

$$\begin{aligned} \sigma(t) &= \sqrt{\sigma_0^2 + \frac{k_B T}{m}\, t^2} \\ &= \sigma_0 \sqrt{1 + \frac{k_B T}{m\, \sigma_0^2}\, t^2}\ . \end{aligned} \tag{3.1}$$

Therefore by measuring the width σ for various diffusion times t we are able to extract the temperature T of the atoms. The results of our time-of-flight temperature measurements are shown in figure 3.10.

3.3 Optical lattice system

The two-dimensional optical lattice is formed by intersecting laser beams orientated as shown in figure 3.11.

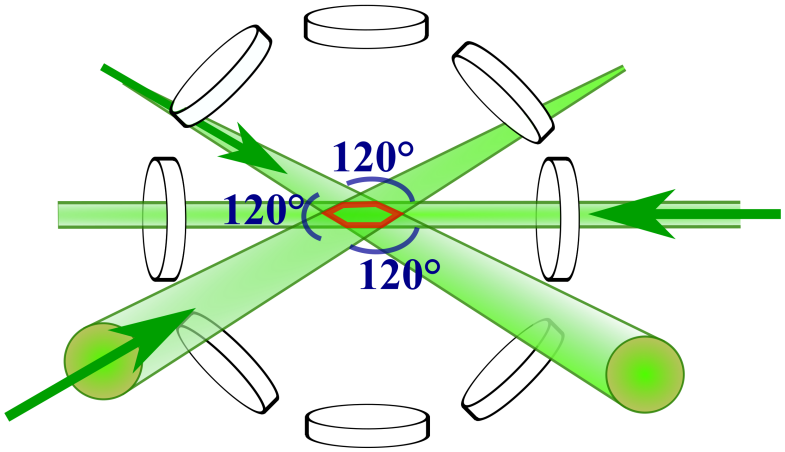

Figure 3.11: The orientation of the lattice beams used to create the two-dimensional optical lattice. The small circles represent the 1 inch viewports and the front and back faces also have large 8 inch windows. The red border indicates the region where the beams intersect and form a two-dimensional hexagonal optical lattice.

In this configuration the three lattice beams are orientated with a mutual 120° angle between them, and are each linearly polarised such that gravity is perpendicular to the plane of the lattice. The beams are red-detuned by approximately $15\,\Gamma$ to form a near-detuned dissipative two-dimensional optical lattice.

When the beams have the same frequency the lattice that is formed is stationary. When the beams have a relative frequency difference, however, the lattice moves with a velocity proportional to the frequency difference. Therefore we are able to impose a driving force on the atoms in the lattice by applying a time-varying frequency shift of the lattice beams. This is the lattice modulation that is used to create the driving force for our ratchet.

The light for the three lattice beams is obtained from a single slave laser, which is injection-locked to the cooling master laser. Therefore the frequency

of this beam is also controlled by the double-pass AOM in the master laser's beam path. The beam from the lattice laser passes through an anamorphic prism pair and an optical isolator and is then guided through an AOM, which shifts its frequency down by 75 MHz so that it is close to atomic resonance. This single AOM also allows intensity control and fast synchronous switching of all three lattice beams. The beam after this AOM is then split into three separate beams, which pass through an additional AOM each. These AOMs have a carrier frequency of 75 MHz and can be individually modulated. Thus it is by modulating these final AOMs that the driving force on the atoms in the optical lattice is realised.

Each lattice beam has a power of around 5 mW at the chamber and a radius just under 2 mm, giving a peak intensity of approximately 80 mW/cm^2. With a typical detuning of 15 Γ the lattice depth is expected to be of the order of $\sim 100\,\mu$K.

There was a continuous effort on my part to try to improve the lifetime of atoms in the lattice as this lifetime limits the duration that the atoms can experience the rocking forces. Optimisation of the lattice loading was achieved by careful alignment of the lattice beams and by varying their relative intensities (via HWP/PBS pairs).
The procedure for optimising the loading of the lattice was as follows:
The three lattice beams are initially aligned by individually overlapping them with the MOT. When properly overlapped, the atoms in the MOT are blown away by the free-running lattice beam and so a rough alignment of the lattice is achieved.
Then the experimental sequence is run so that the lattice is loaded and then imaged very soon after. At the early stages, if necessary, the MOT beams are left on for some time in order to provide additional confinement. The fluorescence images provide an indication of whether any atoms are being held in the lattice and, if not, which direction they are being pushed away in. The beams' alignments and relative powers are then altered iteratively to get atoms loaded in the lattice.
The experimental sequence is then changed so that the lattice holding time is longer and the sequence of optimisation is repeated until the atoms are being trapped for a sufficient time in the lattice. As the lattice holding times get longer any small imbalances between the beams become clearly exposed.

Figure 3.12 shows some lattice lifetime measurements taken at different stages of the experiment. The data was taken by observing the atomic fluorescence of the atoms after a specified holding time in the lattice. When the fluorescence became small the gain of the camera was increased, and then this gain was factored out in the analysis. The fluorescence (in arbitrary units) is plotted against the lattice holding time t and fitted to an exponentially

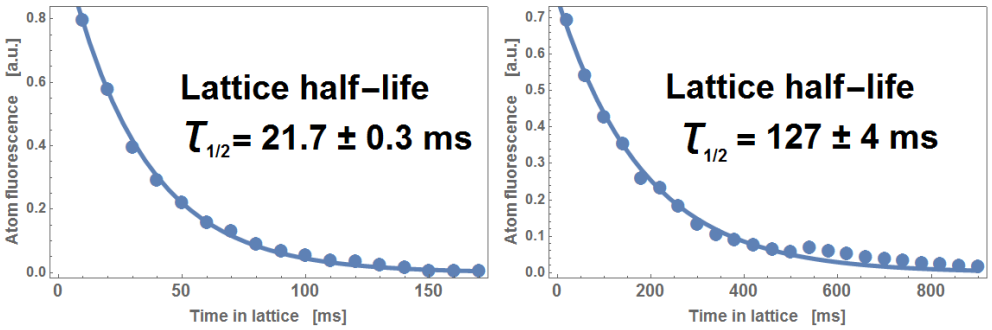

(a) $\tau_{\frac{1}{2}} = 22\,\text{ms}$ (b) $\tau_{\frac{1}{2}} = 127\,\text{ms}$

Figure 3.12: The lattice lifetimes at the 'best' of times (right) and the 'worst' of times (left).

decaying function $e^{-\lambda t}$ with decay constant λ, from which the half-life can be extracted (the half-life of the lattice – the time at which the number of atoms remaining in the lattice diminishes by half – is given by $\tau_{\frac{1}{2}} = \ln(2)/\lambda$).

The total layout of the experiment's optical elements is shown in figure 3.13 and the general schematic of light distribution is given in figure 3.14.

3.4 Generating a rocking ratchet

The three ratchet AOMs are supplied with a frequency of 75 MHz by separate Marconi function generators[7], which can be mutually phase-locked and can also accept frequency modulation inputs. These modulation inputs are supplied externally by two Agilent function generators[8], which are also phase-locked and are used to implement the rocking forces on the lattice by modulating the frequency of the Marconi generators. They are connected to the Marconi generators via an intermediate buffer-box, which adds and subtracts the Agilent signals. As a result of this and the lattice geometry, the two Agilent generators produce motion along the x and y direction respectively, as is demonstrated in figures 3.15 and 3.16.

According to the geometry of the lattice, the force experienced by the atoms is given by

$$\underline{\mathbf{F}} = (F_x,\, F_y) = -m\,(a_x,\; a_y) = -\frac{m}{3k}\left(\dot{\Sigma},\; \sqrt{3}\dot{\Delta}\right), \tag{3.2}$$

where $\Sigma = \psi_1(t) + \psi_2(t)$ is the sum of the frequency-modulations, and $\Delta = \psi_1(t) - \psi_2(t)$ is the difference of the frequency-modulations.

In this experiment we use two function generators producing the signals:

[7] Marconi 2024 9 kHz–2.4 GHz signal generator
[8] Agilent A33220

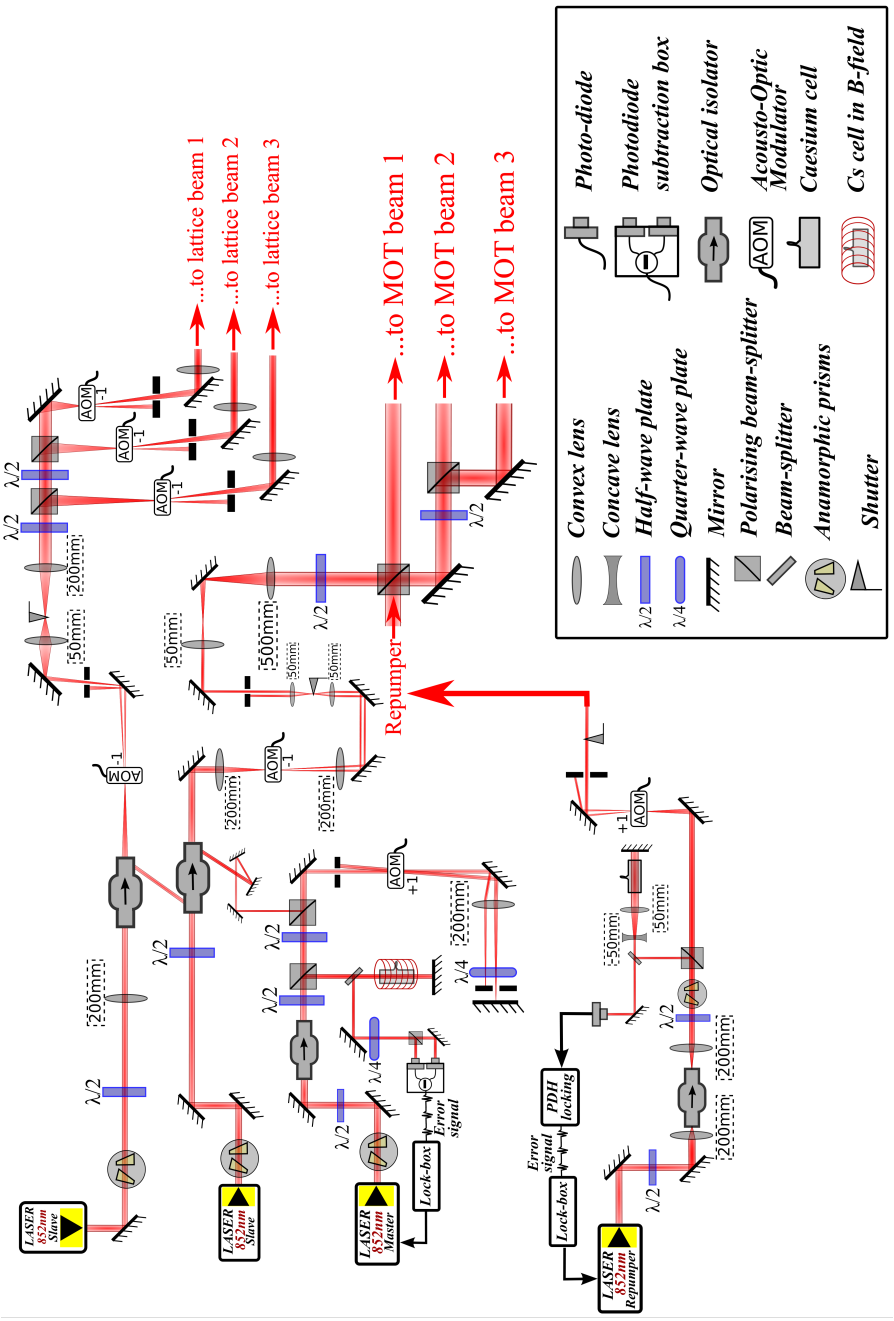

Figure 3.13: The experiment's optical layout showing the path of light through our experimental set-up.

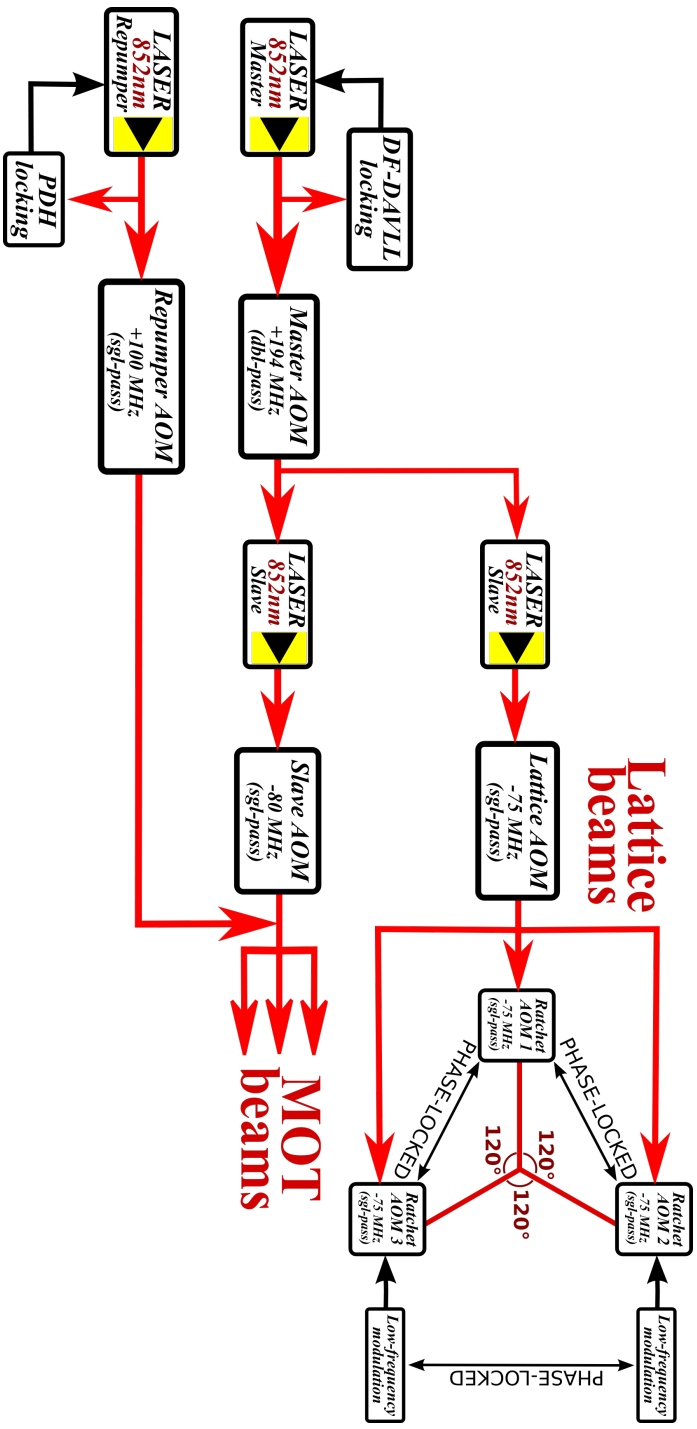

Figure 3.14: A general schematic of the flow of light through our experiment, showing the four laser sources and the seven AOMs in the beam paths.

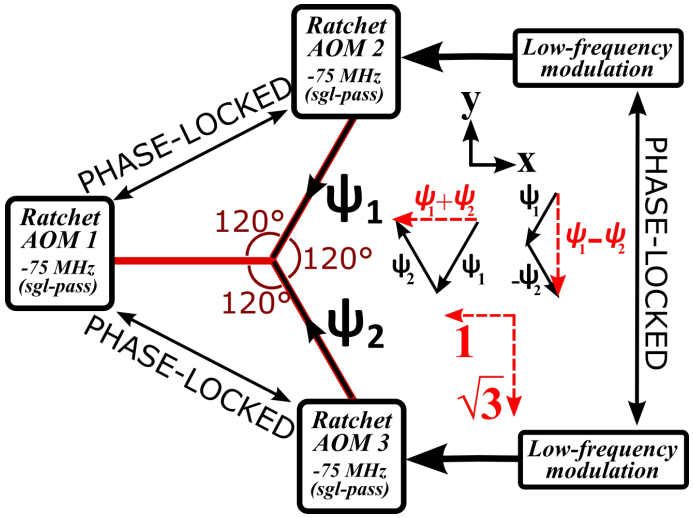

Figure 3.15: The configuration of the lattice beams, as well as the force vectors associated with the modulation forces. Because of the lattice geometry, the sum and difference of the lattice modulation vectors ψ_1, ψ_2 produce modulation along the x and y axis respectively.

$$V_x(t) = A_1\left[\sin(\omega_1 t) + \frac{1}{2}\epsilon_1 \sin\left(2\omega_1 t + \phi_1\right)\right]$$
$$V_y(t) = A_2\left[\sin(\omega_2 t) + \frac{1}{2}\epsilon_2 \sin\left(2\omega_2 t + \phi_2\right)\right].$$

Then, with the help of a buffer box that adds and subtracts the signals, we use $\psi_1 = V_x + V_y$ to drive one of the AOMs and $\psi_2 = V_x - V_y$ to drive another. There is one AOM that is left unmodulated, as is shown in figure 3.15.
From our definitions of Σ and Δ,

$$\Sigma \equiv \psi_1 + \psi_2 = (V_x + V_y) + (V_x - V_y) = 2V_x$$
$$\Delta \equiv \psi_1 - \psi_2 = (V_x + V_y) - (V_x - V_y) = 2V_y\,,$$

and so differentiating yields

$$\dot{\Sigma} = 2\dot{V}_x = 2\omega_1 A_1\left[\cos(\omega_1 t) + \epsilon_1 \cos\left(2\omega_1 t + \phi_1\right)\right]$$
$$\dot{\Delta} = 2\dot{V}_y = 2\omega_2 A_2\left[\cos(\omega_2 t) + \epsilon_2 \cos\left(2\omega_2 t + \phi_2\right)\right].$$

Thus, from equation 3.2 we see that the force is given by: $\underline{\mathbf{F}} = (F_x,\ F_y)$

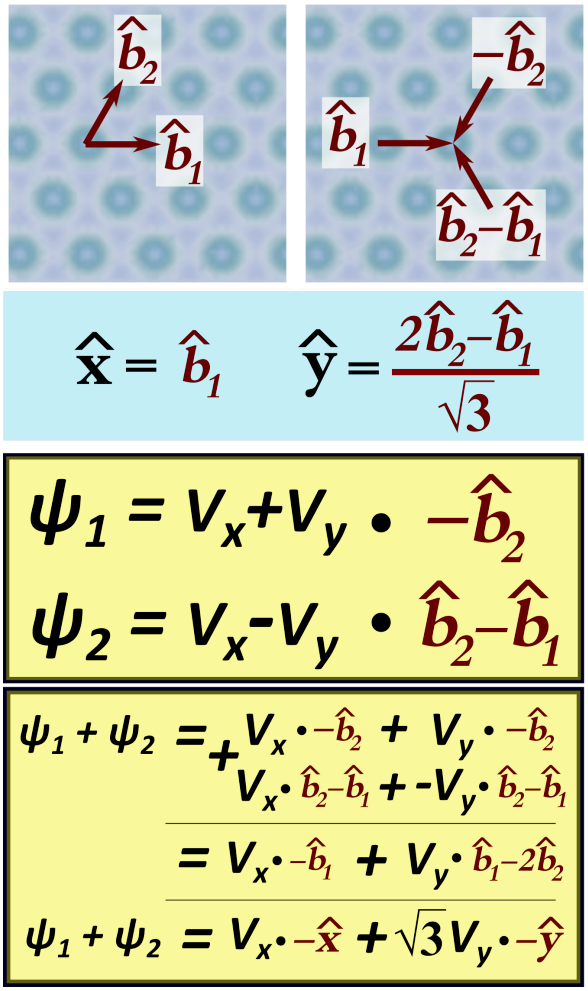

Figure 3.16: The hexagonal lattice geometry and associated lattice vectors $\hat{b}_1$, $\hat{b}_2$. The function generators produce signals V_x, V_y, which are added and subtracted to form $\psi_1 = V_x + V_y$ and $\psi_2 = V_x - V_y$. ψ_1 is implemented along the $-\hat{b}_2$ direction and ψ_2 is implemented along the $\hat{b}_2 - \hat{b}_1$ direction, which then ensures that the V_x driving is along the (negative) x direction and the V_y driving is along the (negative) y direction.

with:

$$F_x = -\frac{2m\omega_1 A_1}{3k}\left[\cos(\omega_1 t) + \epsilon_1 \cos\left(2\omega_1 t + \phi_1\right)\right] \tag{3.3a}$$

$$F_y = -\frac{2m\omega_2 A_2}{\sqrt{3}k}\left[\cos(\omega_2 t) + \epsilon_2 \cos\left(2\omega_2 t + \phi_2\right)\right], \tag{3.3b}$$

which are of the form of the general biharmonic driving given in equation 2.3 on page 40, which is used throughout this thesis.

3.5 The imaging

There are two types of imaging that are used most often in cold atom experiments: fluorescence imaging and absorption imaging, both of which have benefits as well as drawbacks.

Fluorescence imaging collects the light emitted from atoms undergoing the cycling cooling transition. Thus the fluorescence image produced is a glowing cloud. It is useful because it is a direct image of the MOT and its position, and it can be set up by simply pointing an infra-red sensitive camera at the radiant cloud. Its drawback, however, is that it must be calibrated carefully to provide accurate results for the number of atoms. The fluorescence picked up by the camera is directly related to the number of atoms but its proportionality is determined by several empirical factors, such as the camera's shutter speed and numerical aperture, the quantum efficiency of the CCD at the specified wavelength, and losses occurring due to optics in the path of the beam, such as viewports or lenses. Performing this calibration accurately can be an extensive task and so, for measurements of atom number, another type of imaging – called absorption imaging – is usually favoured.

In absorption imaging a resonant probe beam is used to cast a shadow of the atomic cloud on the CCD camera. Then the cloud is removed and another image is taken of the probe beam without the cloud present. By dividing the images one can get an image of the optical depth of the cloud, from which the atom number can be extracted directly. In most schemes an additional third image is taken with the cloud removed and all beams off entirely in order to subtract any dark current produced by the camera itself. The drawback of absorption imaging is that it is a destructive imaging technique, as the cloud must be removed to take the second (and third) image. Also, an additional resonant probe beam and corresponding optical elements must be introduced into the experiment, thereby increasing its complexity.

Since our experiment involves determining the centre-of-mass position of the cloud, and atom number does not play a primary role, we chose fluorescence imaging as this gives a straightforward means of determining the cloud position. The number of atoms can be estimated, however. Assuming a typical peak MOT density of some $10^{10}\,\mathrm{atoms/cm^3}$, and a cloud size of around one millimetre, gives something of the order of tens of millions of atoms in the MOT.

The camera we use is an AVT Guppy NIR with a variable objective lens allowing variable magnification. In order to determine the velocity of atoms from the displacement in the image it was necessary to calibrate the camera pixel-size. This was achieved initially by imaging a piece of graph paper. First the fluorescence from the cloud of atoms in the MOT was observed generally and the objective lens was adjusted to magnify and bring the cloud into focus. Then, with the objective lens fixed, the camera was directed towards a sheet of graph paper. The graph paper was carefully positioned so that it was in sharp focus, where it was fixed and an image was taken. Using computer software the number of pixels forming a 1 millimetre grid-line was determined for several portions of the graph paper; 115 pixels/mm for the x direction and 100 pixels/mm for the y direction. This gives a size of 8.7 μm/pixel and 10 μm/pixel for the x and y direction respectively. Comparing this value to the CCD pixel size for our camera (8.4 μm and 9.8 μm) gives a magnification very close to unity.

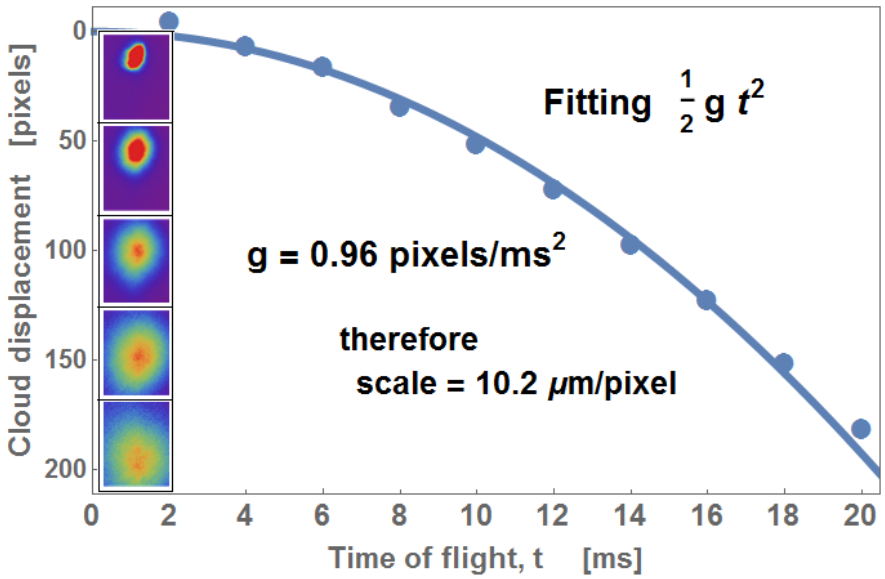

Figure 3.17: Measurement of the pixel size using TOF imaging of the centre of mass falling under gravity. Since all masses free-fall under gravity in the same way, the pixel size can be derived from the parabolic trajectory of the atoms under the influence of gravity. The value agrees well with that measured by imaging the graph paper (measured as 10 μm/pixel).

A more robust method of determining the magnification is by using time-of-flight (TOF) imaging of a cloud falling freely under gravity, although this only allows the determination along one axis (along the direction of gravity). The idea is that under the influence of gravity the acceleration is the same for all masses – that is, it's purely geometrical – and so by imaging the trajectory

of a cloud falling under the influence of gravity one can determine what the image magnification must be. Results for the camera magnification calibration[9] using TOF imaging are shown in figure 3.17. In our case the atoms accelerate at just under $1\,\text{pixel/ms}^2$, which must correspond to the gravitational acceleration $g = 9.8\,\text{m/s}^2$, and so from this it is deduced that the pixel size is $10.2\,\mu\text{m}$. This corresponds well with the value obtained by the graph paper camagnifibration.

The camera is controlled by imaging software that was developed using LabVIEW. This software obtains images from the camera, displays them and saves them, as well as providing some in-situ measurements of the intensity distribution. It is also used to control the camera's shutter speed, gain, and trigger delay. The camera is triggered externally by a digital signal delivered from the NI PCI boards that are controlled by a separate software. Details of the computer control and acquisition are given in the dedicated chapter 4, as its development formed a significant part of the project.

3.6 Experimental procedure

To sum up the experimental sequence by a single function, it is to input different driving forces for the atoms, and to output the resulting velocity of the atomic cloud.
How this is accomplished forms the subject of this section.

Experimental stages

The general programme of operation is shown in figure 3.18 and a typical experimental cycle is shown in figure 3.19.

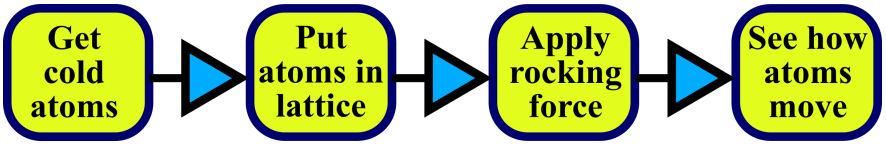

Figure 3.18

Atoms are trapped and cooled in a magneto-optical trap and are then loaded into an optical lattice. The atoms in the lattice are then rocked according to the driving $f(t)$ for a certain duration T_d. The lattice is then switched off and, after some short diffusion time, the centre-of-mass (CoM) position of the cloud is read off from an image by fitting a 2D Gaussian profile to the atomic cloud. Combining this CoM position with the duration of the modulation and diffusion, as well as knowledge of the initial CoM position,

[9] *camagnifibration* for "short"

we are able to deduce the CoM velocity of the cloud. It is this velocity v that we seek to measure for different driving forces $f(t)$ and driving times T_d.

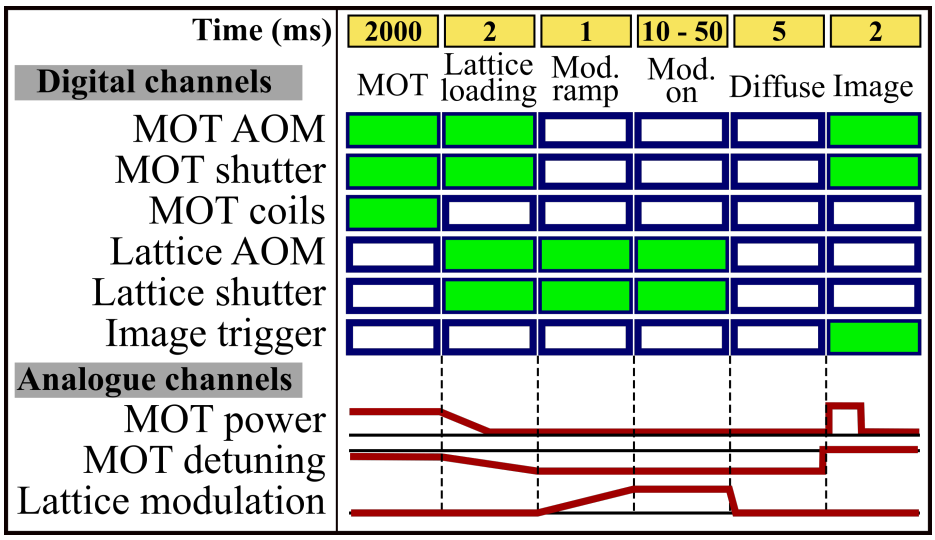

Figure 3.19: A typical experimental cycle, showing the settings for the digital and analogue channels. The entire sequence typically lasts around 3 seconds.

Each cycle produces one image of the cloud. An average of 5 images is taken for a single data point. A graph, such as the one shown in figure 5.1 on page 81, requires 13 velocity measurements to cover the range of 0 to 2π in steps of $\pi/6$, requiring $13 \times 5 = 65$ images. A graph like that shown in figure 6.5 on page 97, is such that each and every data point requires a graph with 13 velocity measurements, so that in total it is made from just under 14 000 images!
It soon became painfully apparent that I needed an efficient means of (a) changing the parameters to take all the data necessary for a plot, (b) meaningfully naming and organising those images, (c) analysing the copious images, so that I wouldn't have to crop and upload each one individually. In order to accomplish these repetitive but crucial tasks I developed a primitive yet powerful command language that allowed me overarching control over the experiment. This software is described in the next chapter.

Chapter 4

Computer control

LabVIEW's controlling.
Mathematica's analysing.
MATLAB's matrix making.
Excel tabulating.
Inkscape for art making.
Powerpoint for showcasing.
Word use for jotting.
LaTeX for producing.
JabRef does job ref'ing.

These are a few of my
fa-vour-ite things.

This chapter describes the software, developed chiefly in LabVIEW, that is used to control the experiment.

It is standard practice in modern atomic physics experiments to have some software that controls the experimental sequence. This software interfaces with a digital and/or analogue PCI board that can provide output voltage signals with μs temporal resolution. These voltage signals are then connected to various components to achieve some control over the experimental apparatus.

The problem, however, is that some devices can not be controlled by basic voltage signals, such as the Agilent function generators used in this experiment to control the driving force on the ratchet. These generators can be remotely controlled but only via a USB connection with device-specific instructions and appropriate drivers installed. Therefore I set about developing a software to control the multiple generators.

The next issue, however, was how to interface these generators with the

sequence and imaging programs. The reason this was necessary is because the general scheme of operation is:
(1) set and output driving parameters – **controlled by Agilent software**
(2) run sequence with new parameters – **controlled by sequencing software**
(3) image cloud a prescribed number of times – **controlled by imaging software**
(4) repeat...

As can be seen, the programs require some degree of communication between them in order to ensure, for example, that the imaging doesn't start until the new settings are in place or that the settings don't get changed while the imaging is still happening!
It is worth noting that the imaging and sequencing programs were already developed before the Agilent program was required, as they had been used for first production of the MOT and lattice loading before the ratchet driving was necessitated. Therefore the new Agilent software required some special features in order to be able to communicate with the pre-existing programs.

This chapter describes the software architecture that was developed in order to accomplish this. It also gives a brief description of the primitive command language I developed that allows the user to specify the ratchet driving forces as well as control all elements of the apparatus.

4.1 Control programs

There are three LabVIEW programs that make up the experiment's computer control – the sequencing, the imaging, and The Controller. The Controller is the main software I developed, incorporating a novel primitive command language that establishes control over the ratchet driving parameters, as well as the ability to disrupt and alter both the sequencing and imaging programs.

The three LabVIEW programs all run independently whilst maintaining some degree of communication between them. The sequencing program is used to control the experimental cycle and analogue/digital outputs; the imaging program controls the camera settings, takes images and saves them; The Controller chiefly manipulates the Agilent function generators but it can also alter parameters on both the imaging and sequencing programs. The general architecture of the computer controlled apparatus is given in figure 4.1.

4.1.1 The sequencing program

The sequencing program is based on an inherited software, to which I added some additional features and also added the capability for it to communicate

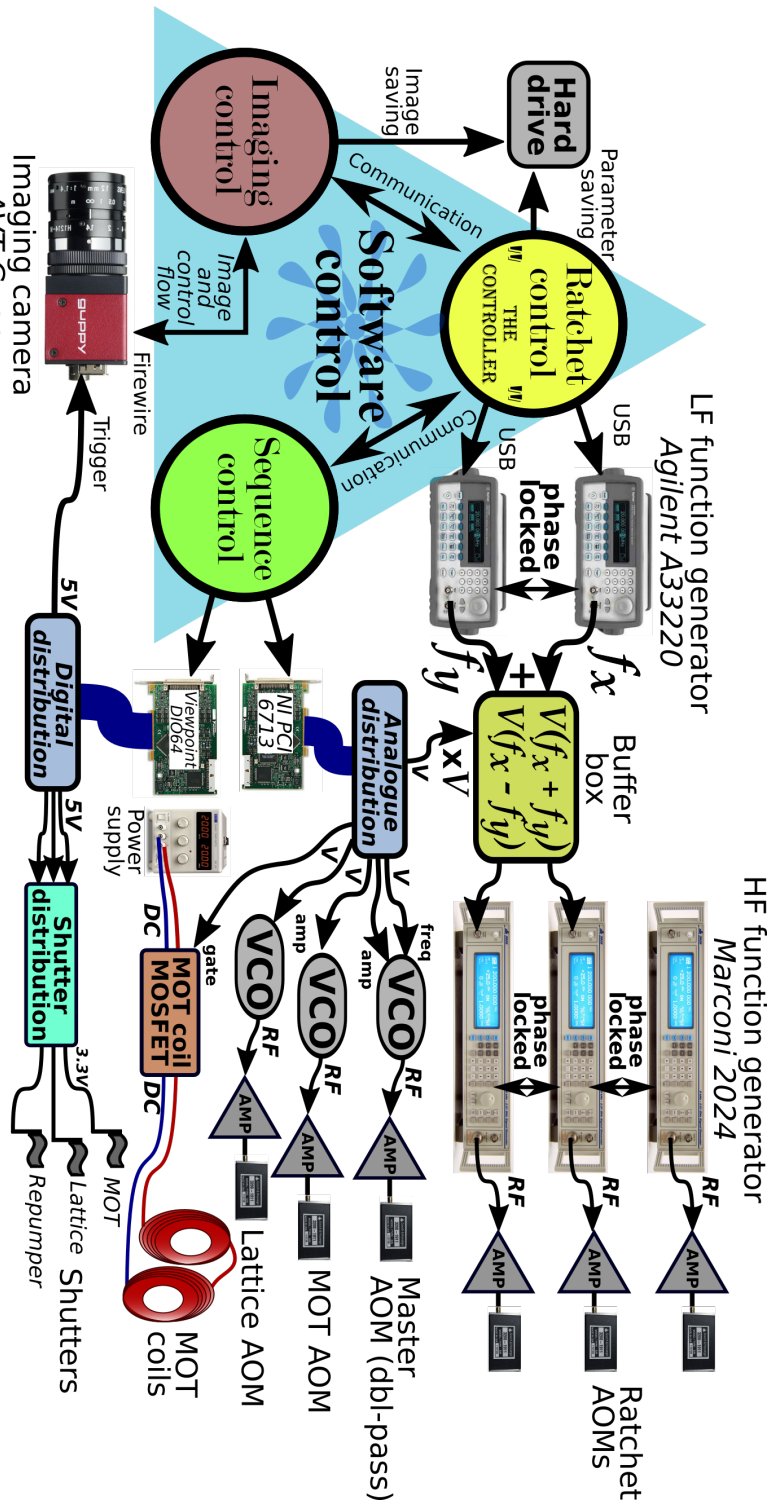

Figure 4.1: Schematic of the computer control for our experimental apparatus and rocking ratchet forces, showing all of the experimental components that are controlled by the computer software.

with The Controller. The sequencing software controls analogue[1] and digital[2] boards, which are connected to BNC distribution boards to allow transmission of analogue voltage signals and digital triggers to the experimental apparatus. The boards are used to electronically control the AOM frequency and amplitude (via the VCO controllers), the MOT coil current (via the MOSFET), the lattice modulation amplitude (via the ratchet buffer-box), the camera triggering, and the shutters.
The layout of the sequence control program is a 2D array much like that shown in figure 3.19 on page 66, with the columns corresponding to time-steps and the rows corresponding to different output channels (analogue or digital). The time interval of each step is user-set, and the channels' values at each time-step can be typed in (or toggled on and off for digital channels). For analogue channels, the program can also produce a linear ramp between two values over a given time. This feature was used to ramp the modulation forces on and off.
I included features to calibrate the analogue channels, so that the user enters values that are more intuitive than basic voltages, as the relationship between the voltage control and the parameter value is unscaled and not necessarily linear. An example is the AOM detuning, which is calibrated to be measured in units of the natural linewidth of the transition, and the AOM intensity, which is input as a percentage of the maximum possible power (type 50 for 50% laser power).

4.1.2 The imaging program

The imaging program was developed specifically for this project. It is built in LabVIEW and communicates with the camera via a firewire cable. This firewire allows the transmission of images from the camera buffer to the computer, and is also able to change the camera's settings, such as the exposure time and trigger delay. It can also change the mode of the camera, from triggered mode to video mode (the latter mode was developed as part of the software).
When in triggered mode, the software reads the camera buffer and waits until it encounters an image. The camera is triggered separately from the NI boards, which in turn are controlled by the sequencing program, which means that the sequencing program controls when the camera exposure starts. Even while the camera is awaiting an external trigger, the software permits one to force the trigger and obtain an image.
Video mode was also developed as part of the software. In this mode, two buffers are allocated on the camera, which are read out consecutively. This is done to optimise the frame-rate, as one buffer is read off and transmitted

[1] NI PCI-6713
[2] Viewpoint DIO-64

while the other is being filled. This way the waiting time between frames is not limited by the buffer readout time. Video mode was very useful for general observation of the MOT fluorescence.

Smart naming

Aside from controlling the camera and extracting and viewing its images, the imaging program had the role of naming and saving the images to the computer. Since we were dealing with a large quantity of images, it was necessary to have some meaningful and automated naming scheme that could include information about the current parameter settings. To this end a "smart name" program was developed, which allows the user to define a relevant name that incorporates updated parameter values.

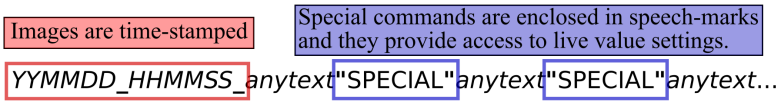

Table of "SPECIAL" commands

Description	Input syntax*	Output string
Image shutter speed	**"imsh"**	Value integer
Image gain	**"imgn"**	Value integer
Image gamma correction	**"imgm"**	Value boolean
Sweep generator name	**"swpGenNm"**	Name string
Alternative generator name	**"altGenNm"**	Name string
Sweep parameter name	**"swpParNm"**	Name string
Sweep parameter value	**"swpPar"**	Value float
Generator state	**"swpGenState"**	State boolean
	"altGenstate"	State boolean
	"gen1State"	State boolean
	"gen2State"	State boolean
Generator parameter value ***(where __?__ stands for any of the ratchet parameters eg: ph1, A, f1,...)***	**"swpgen__?__"**	Value float
	"altgen__?__"	Value float
	"gen1__?__"	Value float
	"gen2__?__"	Value float

**all SPECIAL commands are case insensitive*

Figure 4.2: Decomposition of the "smart name" scheme. By inputting special commands between inverted commas the image names become relevant to the current experimental settings.

The current parameter values are fed to the imaging program by The Controller every time they are updated and by using the specified syntax (figure 4.2) the file names provide relevant and specific information about the parameter settings.

4.1.3 The Controller

The Controller has the primary function of controlling the Agilent function generators that are used to produce the rocking force on the atoms in the lattice, but it also possesses control over the imaging and sequencing programs and, by extension, controls the entire experiment.
In order to achieve this control I developed a primitive command language within LabVIEW itself. The intention of this was to make data-taking more efficient and less prone to human error. Indeed, when I first started taking measurements, hand-changing all the parameters could sometimes lead to instances where I mistakenly entered incorrect values, or forgot to change an image name, or skipped a data-point, etc..., so in order to achieve a more coherent data-taking regime I undertook the task of developing the computer control language.
The language allows the user to enter an arbitrary list of parameter scans with arbitrary settings that are executed procedurally. When the user enters the code, subject to the syntax rules developed, they are simply entering text into a LabVIEW text box. The real programming task was in parsing and translating this code into a sequence of commands, and then programming the response to these commands.
The structure of the language is relatively simple and can perform a great number of unique parameter scans by a concise expression. For example the following snippet of code provides $44,550$ unique (and error-free!) settings of driving for the ratchet:

```
!
gen1_ph[0:15:360] *phase: 0 to 360 degrees in 15 degree steps*
(A=[1:0.5:5];     *amplitude: 1V to 5V in 0.5V steps*
f=[50k:20k:250k]) *frequency: 50kHz to 250kHz in 20kHz steps*
{t#5=[20:10:100]} *time: 20ms to 100ms in 10ms steps*
!
```

Each setting will have 5 associated images, resulting in over $222,000$ images in all. Needless to say, automated image smart-naming was invaluable.

Software flow and architecture

To summarise the general architecture of the software is loops within loops. This reflects the experimental procedure because for each parameter setting we require several images, and for each graph we require several parameter settings, and we may require several parameters changing and several graphs. This all resembles nested loops and so The Controller's main structure is that of nested loops. This is represented in figure 4.3, where the different levels of the loops within loops are portrayed.

This nested loop structure is also representative of how the files were saved in the directories. This means that I was able to write some Mathematica

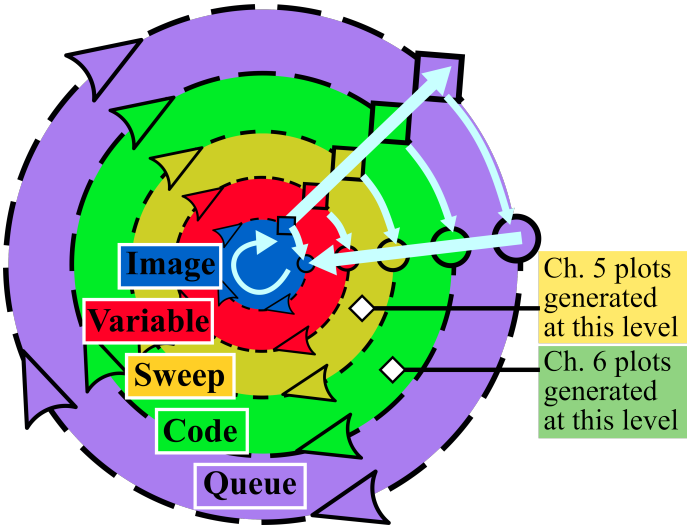

Figure 4.3: The nested loop architecture of the software showing the five main loops. Inner loop (1): each data point requires an imaging loop. (2): multiple data points require a variable loop. (3): multiple variables require a sweep loop. (4): multiple sweeps require a code loop. Outer loop (5): multiple codes require a queue loop.

code that would analyse the copious number of images in a systematic and efficient manner, making it able to decipher the sweep code and plot graphs accordingly. The ambition was to input the location of the code directory and to have as an output the final graphs.

Sweep code

The 'sweep code' refers to the code that the user inputs in order to control the experiment. This sweep code was developed in order to make data-taking more efficient and error-free. It is input in The Controller LabVIEW program as a string according to the syntax rules described below. This string is then translated by LabVIEW and the experimental parameters are changed accordingly. The sweep code was developed in order to have total control over the ratchet driving parameters as well as the sequencing and imaging programs. This section describes the primitive control language that is used to set the ratchet driving parameters via the Agilent function generators as well as to control the imaging and sequencing programs. The general structure of the sweep code is given in figure 4.5, and the specific parameter name values are provided in figure 4.6

The settings are applied in the order they are written, meaning that it is possible to over-ride an existing value by redefining it after.

When inputting a parameter, the values it can take can be either floats,

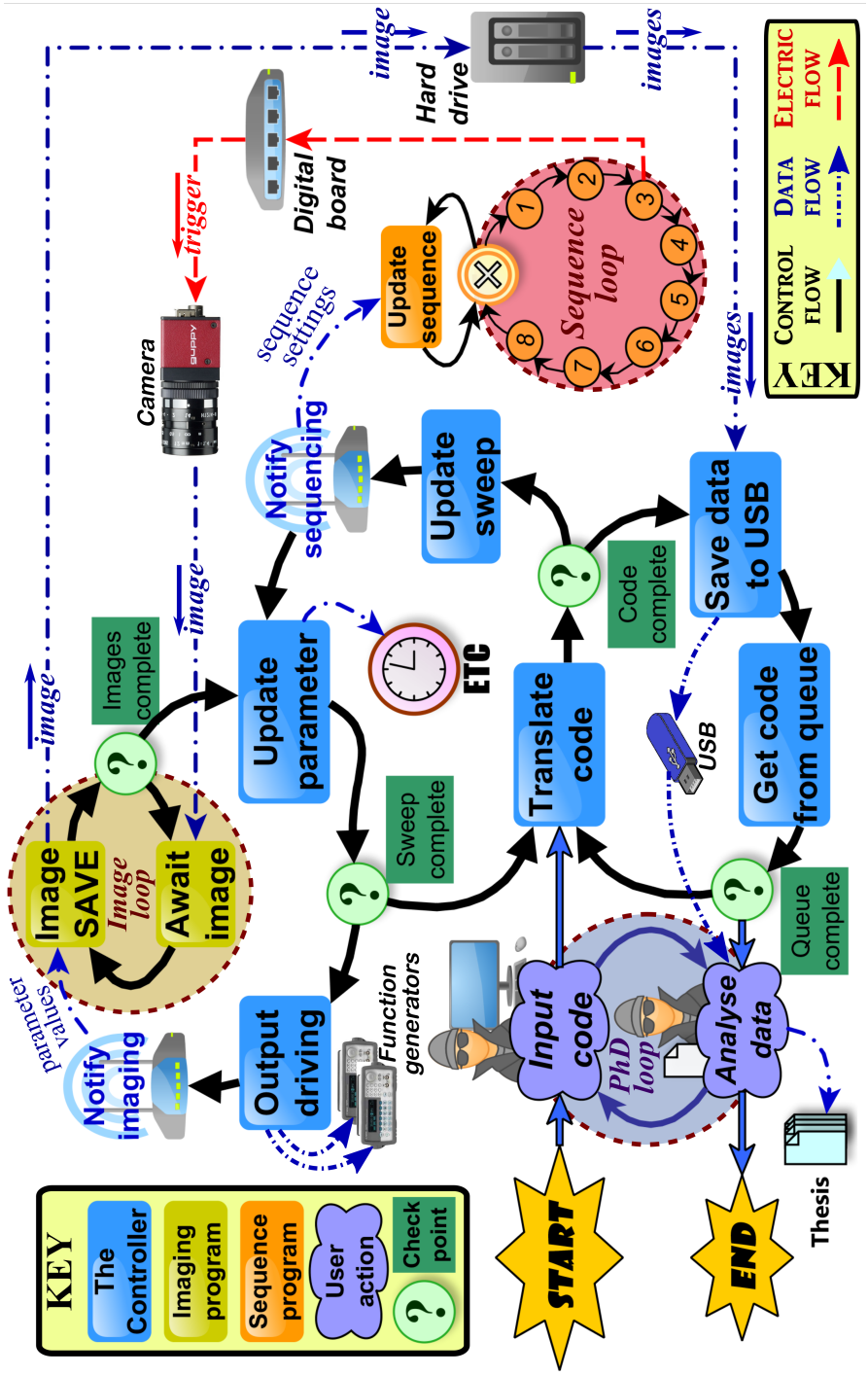

Figure 4.4: Network graph of the software control flow showing how The Controller rules the data-taking process using notifications to affect the 'image loop' and 'sequence loop', which represent independent stand-alone programs that were developed *before* The Controller. With minor modifications to the existing programs plus a touch of creative programming The Controller was able to completely take charge of the entire system. This automation made data-taking more stream-lined and efficient as well as less prone to 'student error'.

integers, or booleans. The floats can be entered as a decimal or as a fraction function, which takes the form *frac(p,q,m)*, which outputs the number *(p/q)*m*. Boolean values can be input as a 0/1, *FALSE*/*TRUE*, *OFF*/*ON*, *NO*/*YES*. The input value formats are summarised in figure 4.7

A particularly helpful feature of the sweep code is the ability to input nested loops. This saves a lot of effort when inputting the code. As an example consider we wish to scan the phase (eg: from 0 to 2π in steps of $\pi/6$) for five different frequencies (eg: 100 kHz to 300 kHz), and to do this for five different values of amplitude (eg: 1 V to 5 V).
This can be written as twenty-five separate lines (one line for each frequency setting at each amplitude setting), but a neater way to do it is by using the in-built nested loop feature of the code. So rather than writing:

```
gen1_ph[0:15:360]    (A=1;f=100k)  &    *scan 1*
gen1_ph[0:15:360]    (A=1;f=150k)  &    *scan 2*
...    ...    ...   ...    ...   ...
gen1_ph[0:15:360]    (A=2;f=100k)  &    *scan 6*
...    ...    ...   ...    ...   ...
gen1_ph[0:15:360]    (A=5;f=300k)       *scan 25*
```

the user may instead simply write in a single succinct line:

```
gen1_ph[0:15:360]    (A=[1:1:5];f=[100k:50k:300k])
```

One point worth bearing in mind is that the nested loops are expanded out in the order they are written. This ordering may be important for appropriate file management.

4.2 Summary

This chapter described the three main computer programs that were developed in order to control the ratchet experiment. It presented the software architecture and then outlined the structure of the command language that was developed specifically for the experiment.

So what's new?

The sophisticated software architecture and basic command language have been developed specifically to enable overarching control over the experiment.

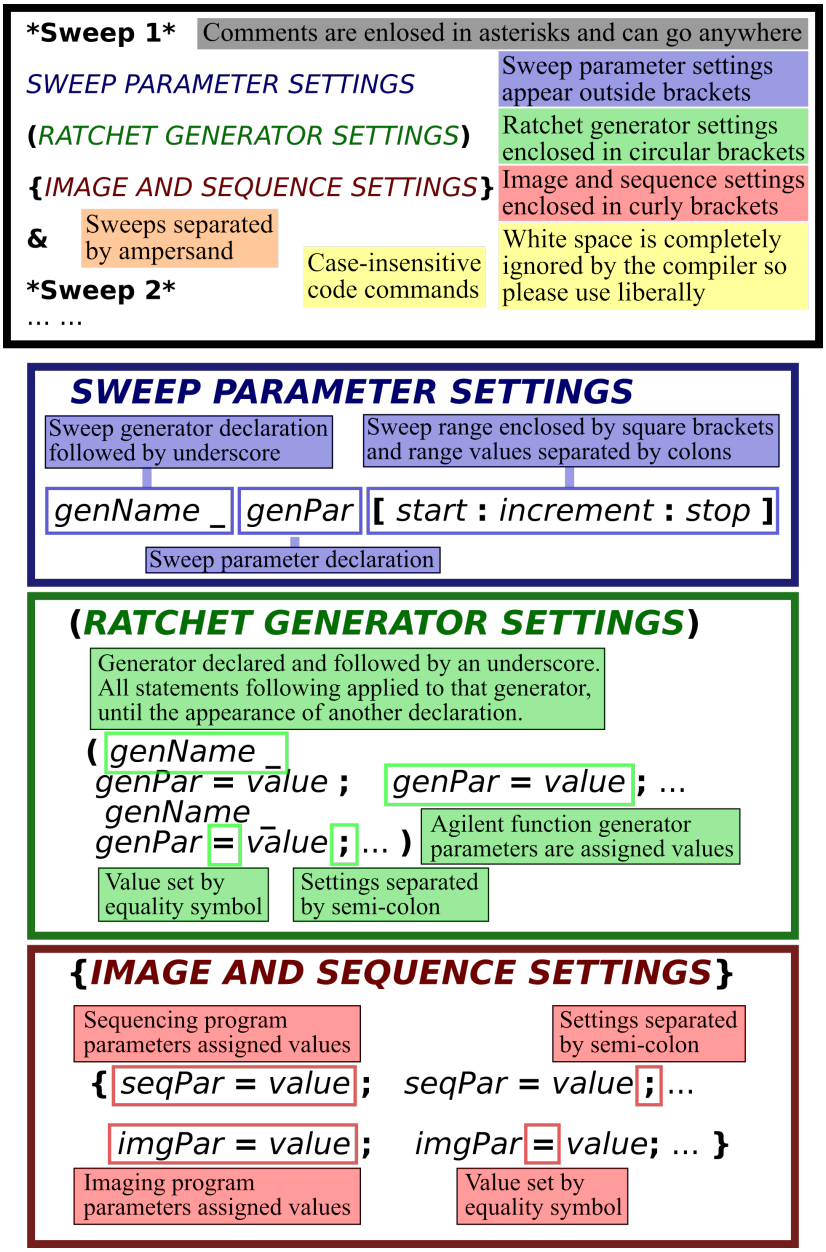

Figure 4.5: Deconstruction of the sweep code format in order to generate arbitrary experimental sequences. The box at the top gives the general layout, which is further expanded in the boxes below it. The code is modularised; different sweeps are separated by an '&' symbol and, within each sweep, the different command sets are distinguished by brackets and, within each bracket, commands are separated by semi-colons. The acceptable syntax of *genName*, *genPar*, *seqPar* and *imgPar* are given in the tables of figure 4.6.

Table of ratchet parameters

Description	Input syntax	Value format	Units	Example
Active generator	**A_ , L_ , gen1_ , gen2_**	Boolean	*no unit*	gen1_=OFF
Amplitude	**A, Amp**	Float/Range	*V*	A = 1.5;
Frequency	**F, Freq**	Float/Range	*Hz*	f = 50.0k;
Harmonic 1 amplitude	**a1, amp1**	Float/Range	*Amp units*	a1 = 1.0;
Harmonic 2 amplitude	**a2, amp2**	Float/Range	*Amp units*	a2 = 0.5;
Harmonic 1 frequency	**f1, freq1**	Float/Range	*Freq units*	f1 = 1.0;
Harmonic 2 frequency	**f2, freq2**	Float/Range	*Freq units*	f2 = 2.0;
Harmonic 1 phase	**ph1, phase1**	Integer/Range	*degrees* °	ph1 = 360;
Harmonic 2 phase	**ph2, phase2, ph**	Integer/Range	*degrees* °	ph = 270;
Waves to output	**waves**	Integer	*unitless*	waves=1000;
Biharmonic settings	**BH**	*no value*	*no unit*	BH;
Split-biharmonic settings	**SBH**	*no value*	*no unit*	SBH;
	This column used for genName & genPar			

(a) Commands to control ratchet parameter settings and driving forces. The highlighted column indicates the replacements for *genName* and *genPar* in figure 4.5.

Table of sequence parameters

Description	Syntax	Value format	Units	Example
Time column value	**t#***column*	Integer/Range	ms	t#5 = 30;
Analog channel value	**a#***channel*,*column*	Float/Range	V	a#2,5 = 0.5;
Digital channel state	**d#***channel*,*column*	Boolean	*no unit*	d#4,5 = OFF;
	This column used for seqPar			

(b) Commands to influence sequencing program and experimental apparatus. The highlighted column indicates the replacements for *seqPar* in figure 4.5.

Table of imaging parameters

Description	Syntax	Value format	Units	Example
Image gain	**imgn, imgain**	Integer/Range	unitless	imgn = 100;
Image shutter speed	**imsh, imshutter**	Integer/Range	µs	imsh = 400;
Gamma correction on/off	**imgm, imgamma**	Boolean	*no unit*	imgm = FALSE;
Image name	**imnm, imname**	<String>	*no unit*	imnm = <myimage>;
	This column used for imgPar			

(c) Commands to influence imaging program and data-saving. The highlighted column indicates the replacements for *imgPar* in figure 4.5.

Figure 4.6: Table of the input command format to control all the parameters of the experiment. The highlighted columns correspond to the commands referenced in figure 4.5.

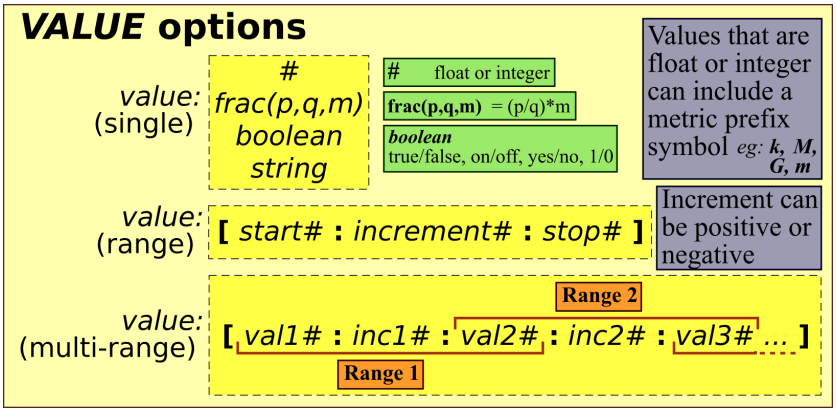

Figure 4.7: The possible formats of the values for the experimental parameters, allowing numerical, boolean and string inputs. Any numerical value can be written as a float or as a fraction using the developed **frac()** function. An arbitrary range of floating point and integer values can also be constructed using the helpful range notation.

Chapter 5

Results of Experiments with the Ratchet Effect in 1D

This chapter looks at the 1D ratchet effect in our two-dimensional optical lattice. The '1D' refers to the fact that a force is applied along one dimension only, be it the x or y direction. A biharmonic driving can be expressed in the following general form:

$$f(t) = A\left[\cos(\omega_1 t + \phi_1) + \epsilon\cos(\omega_2 t + \phi_2)\right],$$

where $\omega_2/\omega_1 = p/q$ for some integers p and q. Our symmetry analysis in chapter 2 revealed that p and q must both be odd for the shift-symmetry to hold, and the relative phase must obey $q\phi_r = n\pi$ for the time-reversal symmetry to hold, where the relative phase is $\phi_r = \phi_2 - (p/q)\phi_1$. Usually we set the phase of the first harmonic to zero ($\phi_1 = 0$) so that the relative phase simply follows the phase ϕ_2 of the second harmonic.
This chapter characterises the dependence of the atomic current on the varying forms of the biharmonic driving force $f(t)$.

5.1 The First Experiment - a simple biharmonic driving

To get a glimpse of this much talked about ratchet effect, let's take a look at a driving of the form

$$f(t) = A[\cos(\omega t) + \cos(2\omega t + \phi)]$$

applied to either the x or y direction. This driving force time-averages to zero, but we can still observe directed transport (ie: the ratchet effect) provided the shift-symmetry and time-reversal symmetry are broken. For the above driving $\omega_2/\omega_1 = p/q = 2/1$ and so the characteristic time-period of the system

is determined by the slow ω harmonic, such that $T = \frac{2\pi}{\omega}$. The shift symmetry requires $f(t+T/2) = -f(t)$, and so the presence of the harmonic at 2ω breaks this shift symmetry since $\cos(2\omega(t+T/2)+\phi) = \cos(2\omega t+\phi) \neq -\cos(2\omega t+\phi)$. The time-reversal symmetry is then determined by the value of ϕ, which is our experimental parameter that we vary from 0 to 2π in steps of $\frac{\pi}{6}$. The time-reversal symmetry holds for values of $\phi = n\pi$, for which values we expect to see no transport.
The results of separate bihamonic driving along the x direction and y direction are shown in figure 5.1, where the leading order sine-like structure of the transport is clearly visible. As suggested by the symmetry analysis, there is zero transport for $\phi = n\pi$.

Atoms moving due to the ratchet effect typically travel with a velocity of the order of the recoil velocity, which is $v_{rec} = 3.5\,\mathrm{mm/s}$, and so they are moving quite literally at a snail's pace.

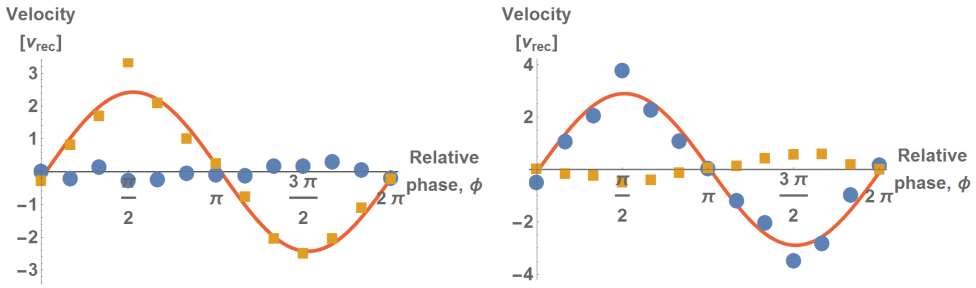

(a) x-axis driving (b) y-axis driving

Figure 5.1: The results of the biharmonic drive along the x and y directions, with $\omega_2/\omega_1 = 2/1$, clearly showing the sine-like structure of the atomic velocity when the relative phase is scanned from 0 to 2π. The motion occurs along the direction of the driving force when the phase corresponds to values that break the time-reversal symmetry. The driving parameters for this experiment were $\omega = 2\pi \cdot 140\,\mathrm{kHz}$, $A = 2\,\mathrm{V}$. Each data point corresponds to the average velocity taken from five images. The velocity is given in units of the recoil velocity, $v_{rec} = 3.5\,\mathrm{mm/s}$.

In figure 5.1 the phase-shift of the driving is small. This occurs when the driving force dominates over the damping force, which can be a result of strong driving or low damping (as in the case of a Hamiltonian ratchet) or both. The damping is controlled by the detuning of the lattice beams, which determines the scattering rate and level of dissipation in the system.

It may be noted that producing transport along each direction independently was reliant on the correct lattice geometry as well as the signals being appropriately added and subtracted in the buffer-box. These results are a good indication that both of these necessities were in place.

5.2 Dependence of transport on the driving amplitude A

In this section we look at the driving form

$$f(t) = A\left[\cos(\omega t) + \cos\left(2\omega t + \frac{\pi}{2}\right)\right]$$

as a function of A, which determines the strength of the force on the atoms. The rocking force is implemented by a voltage signal from the Agilent signal generators that is fed into the Marconi function generators controlling the ratchet AOM frequencies. The maximum modulation depth of the Marconi generators is 100 kHz/V, which means an input of ±1 V will shift the AOM frequency by ±100 kHz about its carrier frequency (typically 75 MHz).
The results in figure 5.2 show that there is an approximately linear dependence of the atomic current on the driving amplitude for our range of voltages.

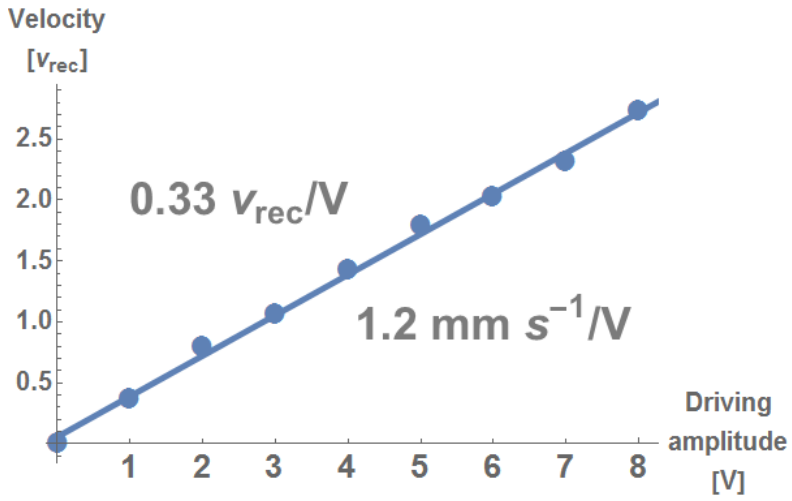

Figure 5.2: The atomic velocity as a function of the driving amplitude, showing a linear dependence with amplitude (as set by user on Agilent function generators). In this experiment $\phi = \frac{\pi}{2}$, $\omega = 2\pi \cdot 90\,\text{kHz}$. Each data point corresponds to the average velocity taken from five images.

As can be seen there are none of the expected current reversals [39] for our range of driving amplitudes. This could be a result of the low dissipation, and only with much stronger driving strengths would a current reversal appear. The fact that the biharmonic curves in figure 5.1 exhibit a small phase-shift corroborates this evidence that we are working in a low-dissipation regime. In general the amplitude was varied on a run-to-run basis in an attempt to optimise the quality of the results.

5.3 Dependence of transport on the relative driving strength ϵ

In this section we look at the driving form

$$f(t) = A\left[\cos(\omega t) + \epsilon \cos\left(2\omega t + \frac{\pi}{2}\right)\right]$$

as a function of ϵ, which determines the relative strength of each harmonic. A plot of the maximum velocity versus the relative driving strength is given in figure 5.3. There it can be seen that there is an optimum balance between the two harmonics that gives maximum transport. It also exhibits the role that both harmonics have to play in manifesting the symmetry breaking. When only one harmonic dominates, the effect of the second harmonic is so reduced that transport is forbidden, because it is as if the atoms are only experiencing a single harmonic and not a biharmonic and so the shift-symmetry is restored. This is represented in the graph by the low velocity near the origin and in the tail end.

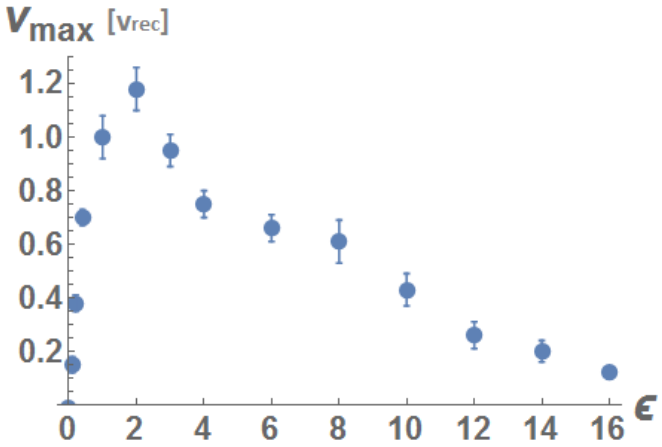

Figure 5.3: The maximum velocity as a function of the relative driving strength of the harmonics, showing that there is an optimum driving ratio. At low and high ratios the velocity drops off because the atoms effectively experience a single harmonic driving, for which transport is forbidden. The driving parameters for this experiment were $\omega = 2\pi \cdot 90\,\text{kHz}$, $A = 2\,\text{V}$. Each data point corresponds to a phase-scan from 0 to 2π in 13 steps, like that shown in figure 5.1, and the maximum velocity was extracted from the fitted sine curves. Therefore each data point represents 65 images.

5.4 Dependence of transport on the driving frequency ω

In this section we look at the driving form

$$f(t) = A\left[\cos(\omega t) + \cos\left(2\omega t + \frac{\pi}{2}\right)\right]$$

as a function of the driving frequency ω.

Measurements were taken of the cloud velocity for different driving frequencies, and are shown in figure 5.4. The relative phase was set to $\frac{\pi}{2}$, corresponding to maximum current for our biharmonic drive of $\omega_2 = 2\omega_1$.

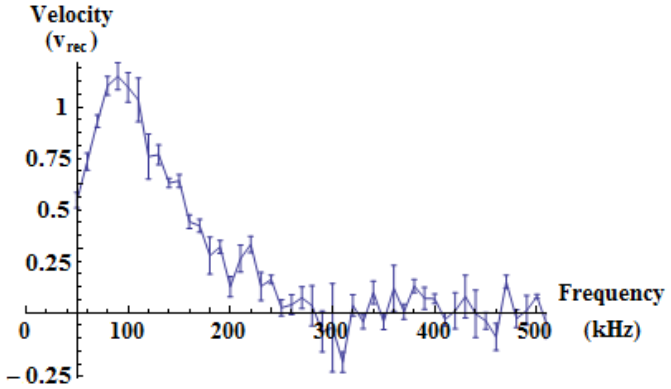

Figure 5.4: The atomic velocity as a function of the driving frequency for a biharmonic driving with $\phi = \frac{\pi}{2}$ and $A = 2\,\mathrm{V}$. The velocity increases until the optimum value around $\omega = 2\pi \cdot 100\,\mathrm{kHz}$, before dropping off at high frequencies. Each data point corresponds to the average velocity taken from five images.

The structure of the resulting curve displays some interesting dynamics, such as the peak at approximately 100 kHz corresponding to a resonant activation [29]. This is a consequence of the driving frequency resonating with a natural frequency of the system, which in this case is the vibrational frequency of atoms in the lattice. When the two frequencies are resonant, transport is maximised corresponding to an optimised rectification of fluctuations.
As the frequency is increased the velocity begins to drop off as a result of the lattice moving too fast for the atoms to respond. Therefore the atoms experience an averaged out 'painted' potential and the effects of the biharmonic driving are dissolved.

5.5 Dependence of transport on the frequency ratio $\omega_2/\omega_1 = p/q$

The following explores the driving

$$\begin{aligned} f(t) &= A\left[\cos(\omega_1 t) + \cos(\omega_2 t + \phi)\right] \\ &= A\left[\cos(\omega_1 t) + \cos\left(\frac{p}{q}\omega_1 t + \phi\right)\right] \end{aligned}$$

for different values of the frequency ratio $\omega_2/\omega_1 = p/q$. The symmetry analysis in chapter 2 indicated that transport is forbidden when p and q are both odd, and so p and q must have opposite parity to break the shift symmetry. The time-reversal symmetry condition was $q\phi = n\pi$, which depends only on q. Results for the biharmonic driving for different values of frequency ratio $\kappa = p/q$ are shown in figure 5.5. Each plot represents the velocity as a function of the relative phase ϕ, for the driving $f(t) = A\left[\cos(\omega t) + \cos(\kappa\omega t + \phi)\right]$.
There the sine-like structure $v_0 \sin(q\phi)$ is clearly visible, exemplifying the time-reversal condition that transport goes to zero for $q\phi = n\pi$.

Figure 5.6 shows a plot of the values of q_{fit} when the graphs in figure 5.5 are fitted to $v_0 \sin(q_{fit}\phi)$.

5.6 Dependence of transport on the relative phase ϕ_r

In this section we look at the driving form

$$f(t) = A\left[\cos(\omega t + \phi_1) + \cos\left(\frac{p}{q}\omega t + \phi_2\right)\right]$$

for different values of the phase ϕ_1.

From our symmetry analysis, the time-reversal symmetry is governed by the relative phase ϕ_r between the harmonics. In chapter 2 we saw that transport is forbidden for $q\phi_r = n\pi$, where $\phi_r = \phi_2 - (p/q)\phi_1$ is the relative phase, so the condition becomes $q\phi_2 - p\phi_1 = n\pi$. So far we have taken $\phi_1 = 0$ and have only varied ϕ_2.
In order to confirm that the velocity is dependent on the *relative* phase we perform biharmonic scans for ϕ_2 from 0 to 2π, as has been done before, but we do this for several different values of ϕ_1. When $\phi_1 = 0$, we expect a sine-wave of the form $\sin(q\phi_2)$, which corresponds to the time-reversal symmetry condition of no transport at $q\phi_r = n\pi$. For non-zero values of ϕ_1 the time-reversal condition becomes $q\phi_2 - p\phi_1 = n\pi$, and so we expect to see transport follow

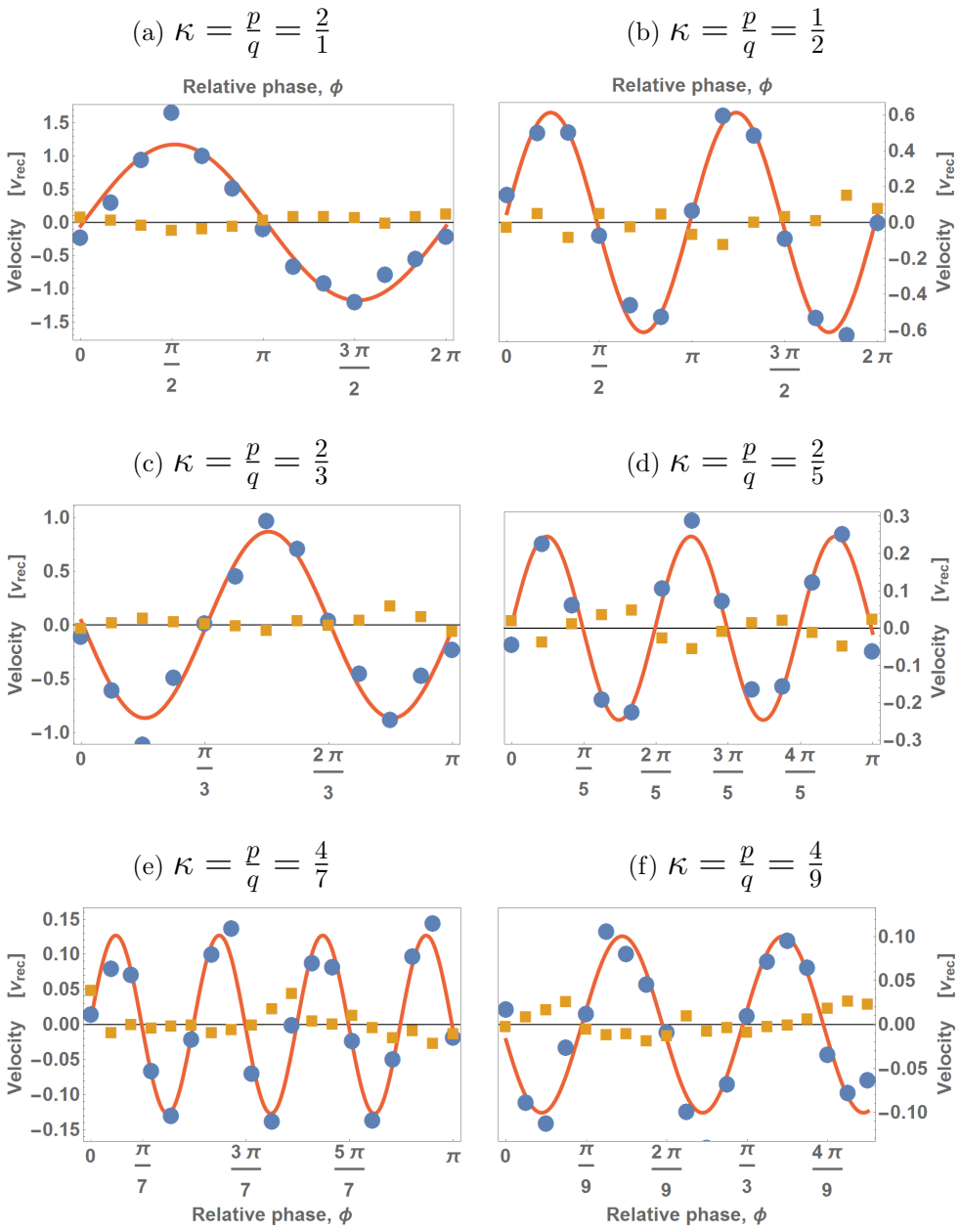

Figure 5.5: Atomic cloud centre-of-mass velocity as a function of the relative phase for different harmonic frequency ratios. When fitted with a curve $v = v_0 \sin(\phi - \phi_0)$ we see that for different relative frequencies, $\kappa = \frac{p}{q}$, ϕ scales with q.

a sine-curve of the form $\sin(q\phi_2 - p\phi_1)$. This corresponds to the original sine-

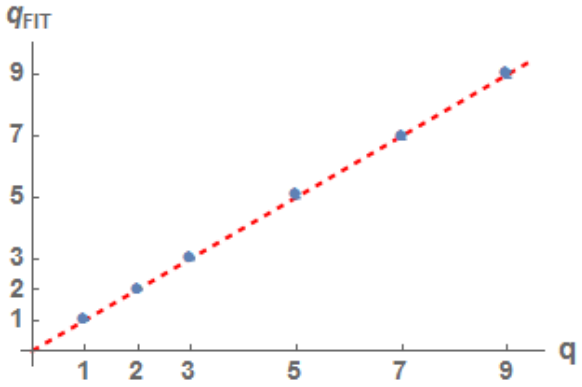

Figure 5.6: Plot of fitted values of q_{fit} when the velocity is fitted with function $v_0 \sin(q_{fit}\phi)$ for different values of driving frequency ratio p/q. The plot clearly shows that the dependence is on the value of q.

curve, but phase-shifted by $-p\phi_1$. Figure 5.7 gives the measured phase-shift as a function of ϕ_1 for two sets of p and q values.

5.7 Summary

This chapter examined the 1D ratchet effect in a two-dimensional optical lattice using the biharmonic driving force. The form of the velocity was characterised as a function of the various driving parameters and explanations of the dependencies were provided.

So what's new?

The characterisation of the ratchet transport as a function of the various driving parameters of the biharmonic force were presented. Some of these parameter dependencies have not been characterised previously, such as the relative driving strengths of the harmonics, which exposes the role that each harmonic plays in producing transport. The results for the biharmonic force as a function of phase for higher values of the p and q were also presented.

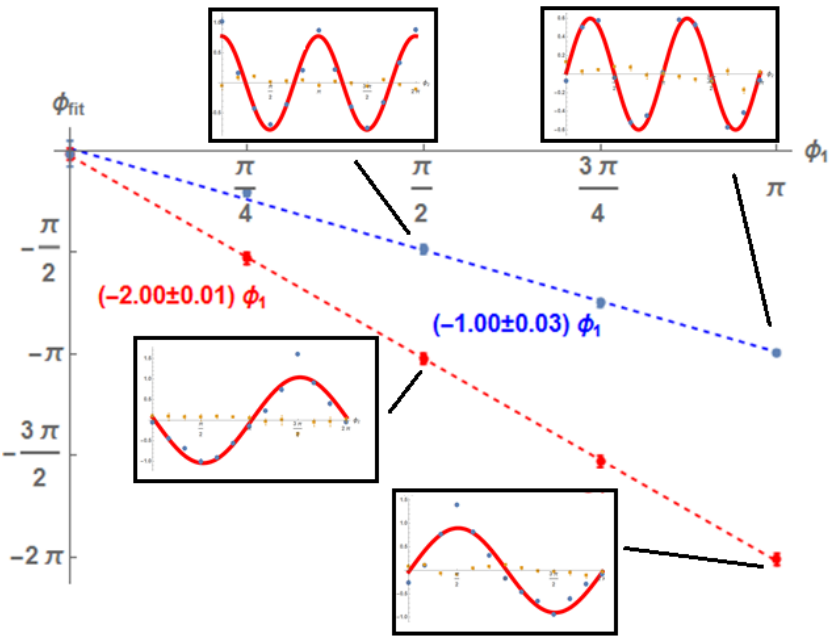

Figure 5.7: The plot of the fitted phase-shift vs. phase of first harmonic, showing that our symmetry condition $q\phi = n\pi$ applies to the relative phase such that $q\phi_2 - p\phi_1 = n\pi$. The red data points correspond to $p = 2$, $q = 1$ biharmonic driving, and the blue data points correspond to $p = 1$, $q = 2$. The **inset** plots show the data scans of ϕ_2 from 0 to 2π for some selected points. The parameters for the driving were $\omega = 2\pi \cdot 90\,\text{kHz}$ and $A = 2\,\text{V}$.

Chapter 6

Results of Experiments with the Ratchet Effect in 2D

This chapter examines the ratchet effect in two dimensions, that is, when driving is applied along both the x and y directions simultaneously. When the system is extended to two dimensions it is found that the transverse directions are coupled and can not be treated as two independent one-dimensional drivings. As a result of this coupling the form of the driving along one direction can influence the transport along the other direction. The chapter begins by demonstrating this coupling using the *split-biharmonic* drive.

By considering the commensurability of the relative driving frequencies we arrive at an analogy to quasiperiodicity in driven systems, and examine how this can be exploited to decouple the transverse degrees of freedom. We also consider how quasiperiodicity is defined in finite-time experiments and demonstrate that it is dependent on the interaction time of the atoms with the driving force.

Additionally, we explore how the specific values of p and q representing the frequency ratio $\frac{\omega_2}{\omega_1} = \frac{p}{q}$ affects the transport for finite interaction times. It is shown that transport is dependent on the value of the denominator q, which leads to the conclusion that, for finite-time experiments, irrational frequency ratios with poor rational approximations are better at exhibiting quasiperiodic behaviour.

It is also demonstrated that the measured velocity profile picks up an additional phase-shift that is proportional to the interaction time and the value of q when ω_2 is in the vicinity of $(p/q)\omega_1$ but not equal to it, leading to dynamical current reversals. By examining the amplitude and the measured phase of the velocity curves for different values of q and T_d we arrive at an experimentally determined velocity master equation.

6.1 Split-biharmonic driving

The split-biharmonic driving refers to the two-dimensional driving of the form:

$$f_x(t) = A\cos(\omega_1 t)$$
$$f_y(t) = B\cos(\omega_2 t + \phi),$$

where each direction is driven by a single harmonic with a relative phase-shift between them.

This is a particularly interesting case as the two harmonics are now separated and drive perpendicular directions, thereby allowing a distinction of effects arising from the presence of each harmonic.
Previous work [42, 43] has considered this driving for the specific case of $\omega_2/\omega_1 = 2/1$. This chapter considers this driving for higher values of p and q and also uses it to understand the role of coupling between the transverse degrees of freedom.

If one considers this driving form such that the transverse directions are completely independent, then it may appear that no driving can occur along either direction. This is because the driving along x is a single harmonic, which we have shown produces no transport, and the driving along y is another single harmonic, which produces no transport along y. This would be true if the x and y directions are decoupled and independent. The reality, however, is that the x and y directions are coupled, and the system must be treated in its entirety. This means that the characteristic time-period of the system is determined by considering both harmonics, and is given by $T = qT_1 = pT_2$. This is in contrast to the case where T_1 and T_2 would be treated as separate characteristic time periods along their respective directions. The symmetry analysis given in chapter 2 determined that p and q must have opposite parity (even/odd) in order for transport to occur.
We now explore the transport for specific values of p and q.

Split-biharmonic drive along each direction

To begin we use $\omega_1 = \omega$, $\omega_2 = 2\omega$ ($p = 2$, $q = 1$), such that the driving forces along each direction are:

$$f_x(t) = A\cos(\omega t)$$
$$f_y(t) = B\cos(2\omega t + \phi).$$

In this case, the presence of the 2ω harmonic breaks the shift-symmetry condition $f(t + T/2) = -f(t)$ where $T = 2\pi/\omega$. The time-reversal symmetry still holds for $\phi = n\pi$. When $\phi \neq n\pi$ we expect to observe transport.

Figure 6.1 shows results for split-biharmonic driving along the x and y directions. There we see that transport occurs along the direction of the 2ω driving.

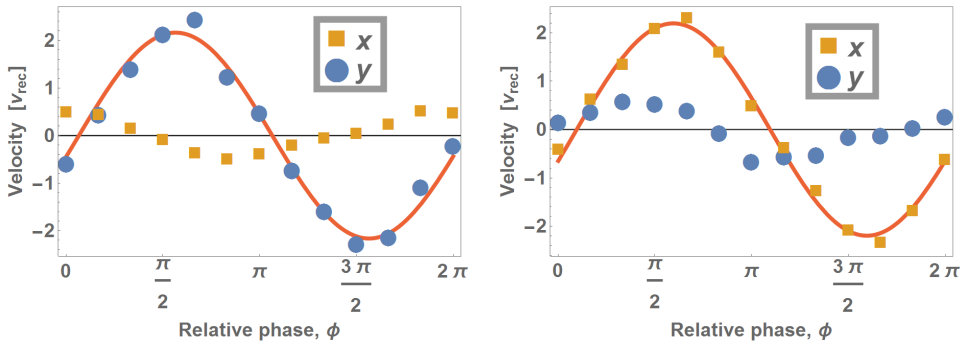

(a) $f_x(t) = A\cos(\omega t)$ and $f_y(t) = B\cos(2\omega t + \phi)$

(b) $f_x(t) = A\cos(2\omega t + \phi)$ and $f_y(t) = B\cos(\omega t)$

Figure 6.1: Split-biharmonic driving along the x and y directions. In this case the motion occurs along the direction of the 2ω driving. As expected, the transport takes on a sine-like structure, with zero transport when $\phi = n\pi$. The driving parameters are $\omega = 2\pi \cdot 90\,\text{kHz}$, $A = 2\,\text{V}$, $B = 1.5\,\text{V}$. Each data point corresponds to the average velocity (units $v_{rec} = 3.5\,\text{mm/s}$) taken from five images.

The significance of this result is that the presence of the harmonic along one direction (let's say x) affects the transport along the other (y) direction, thereby clearly exhibiting that they are coupled. If the driving along x were absent the system would be shift-symmetric due to the fact that the characteristic time-period would be that of the y direction's $\omega_2 = 2\omega$ drive, which is $T_2 = 2\pi/\omega_2 = \pi/\omega$. With the presence of the harmonic $\omega_1 = \omega$ along the x direction the characteristic time-period becomes the time-period of this slower ω_1 component, which is $T = 2\pi/\omega_1 = 2\pi/\omega = 2T_2$. With this new characteristic period, the ω_2 component now breaks the shift-symmetry. The time-reversal symmetry is then governed by the relative phase ϕ and we expect no transport for $\phi = n\pi$, as the results in figure 6.1 demonstrate.

6.2 Direction of motion

In this section we explore the direction of motion for the split-biharmonic drive.

According to our symmetry analysis, we require p and q to have opposite parity in order to break the shift-symmetry, and we require the relative phase to obey $q\phi \neq n\pi$ for n integer in order to break the time-reversal symmetry.

It is in fact the shift-symmetry that determines the direction that motion occurs. This becomes apparent when we consider the split-biharmonic case, because the two harmonics are spatially separated and it is only the even

harmonic that breaks shift-symmetry.
To clarify this matter, let us consider a separate case with the driving:

$$f_x(t) = A\cos(2\omega t)$$
$$f_y(t) = B\cos(\omega t + \phi).$$

Again the 2ω driving breaks the shift-symmetry, but this time it is orientated along the x direction. The y direction controls the relative phase and thereby the time-reversal symmetry. The condition for the time-reversal symmetry to hold is $q\phi = n\pi$, where $q = 2$ in this case.

As the results in figure 6.2 demonstrate, the direction of the motion occurs along the 2ω direction, which is the direction that breaks shift-symmetry, and the velocity follows the form of $\sin(q\phi)$ with $q = 2$.

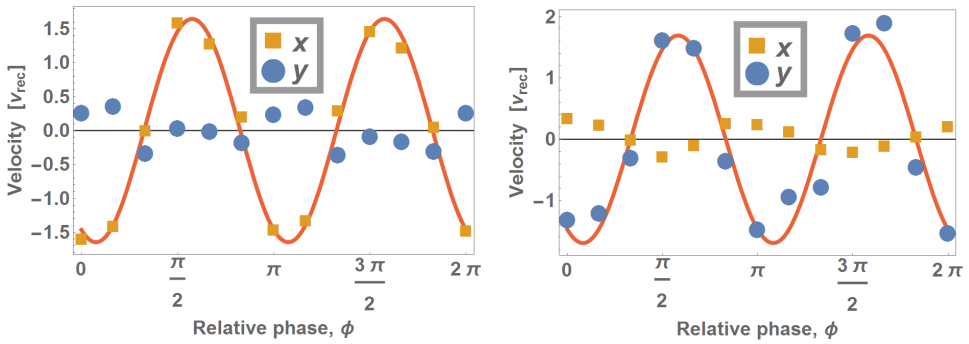

(a) $f_x(t) = A\cos(2\omega t)$ and $f_y(t) = B\cos(\omega t + \phi)$

(b) $f_x(t) = A\cos(\omega t + \phi)$ and $f_y(t) = B\cos(2\omega t)$

Figure 6.2: Split-biharmonic driving along the x and y directions. In this case the motion occurs along the direction of the 2ω drive. The driving parameters are $\omega = 2\pi \cdot 90\,\text{kHz}$, $A = 2\,\text{V}$, $B = 1.5\,\text{V}$.

To illustrate this matter further, and to show that transport is not simply occurring along the direction of the faster frequency component, we consider the following driving:

$$f_x(t) = A\cos(2\omega t)$$
$$f_y(t) = B\cos(3\omega t + \phi).$$

In this scenario the y direction has a higher frequency driving, and governs the time-reversal symmetry by the phase. The x direction is the slower component, but breaks the shift-symmetry due to the even harmonic. The results in figure 6.3 show that the transport occurs along the slower, but shift-symmetry breaking, 2ω direction.

It is interesting to note that even though motion does not occur along the direction where the shift-symmetry holds, it is still necessary for atoms

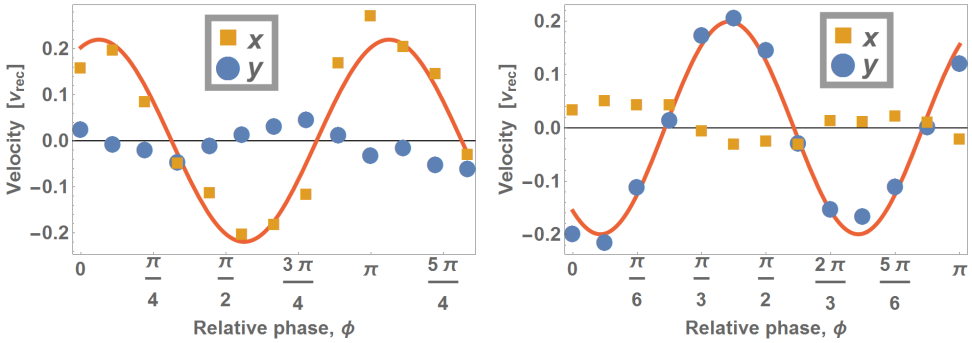

(a) $f_x(t) = A\cos(2\omega t)$ and $f_y(t) = B\cos(3\omega t + \phi)$

(b) $f_x(t) = A\cos(3\omega t)$ and $f_y(t) = B\cos(2\omega t + \phi)$

Figure 6.3: Split-biharmonic driving along the x and y directions for $p = 3$, $q = 2$ (**left**) and $p = 2$, $q = 3$ (**right**). In both cases the motion occurs along the direction of the 2ω driving. Driving parameters are $\omega = 2\pi \cdot 90\,\text{kHz}$, $A = 2\,\text{V}$, $B = 1.5\,\text{V}$.

to explore orbits along this direction in order to produce transport along the symmetry-breaking direction. If the symmetry-preserving frequency was absent no motion would occur along the symmetry-breaking direction.

Previous theoretical work [62, 16] has suggested that time-shift invariance of the system is responsible for the form of the current. The results presented above enable us to be more specific: in our experiments the time-reversal symmetry governs the shape and the shift-symmetry determines the direction.

The fact that the direction of transport is not related to the direction of the phase-shift is due to it being just a *relative* phase-shift $\phi_r = \phi_2 - \kappa\phi_1$ (where $\kappa = p/q$). Therefore applying a shift of $\phi_2 = \phi$ with $\phi_1 = 0$, or applying a shift of $\phi_2 = 0$ with $\phi_1 = -\phi/\kappa$, is exactly equivalent. The atoms in the lattice can't recognise which harmonic, and so which direction, is shifted with respect to the other. They can recognise, however, which direction breaks shift-symmetry and so this determines their direction of transport.

6.3 Irrationality and quasiperiodicity in the ratchet effect

In the case of the split-biharmonic driving we have so far only considered frequency ratios where $\omega_2 = (p/q)\omega_1$ exactly. The question now arises to how precisely defined this frequency ratio must be? For example, we know that a split-biharmonic driving where $\omega_2 = 2\omega_1$ produces transport, but what about a driving of $\omega_2 = 2.1\omega_1$, or $\omega_2 = 2.001\omega$? Can these be considered as *close enough*? This is a question of commensurability and is related to the concept of irrationality in number theory.

Approximating irrational numbers: the good, the bad, and the ugly

An irrational frequency ratio ω_2/ω_1 can be characterised by $|\omega_2/\omega_1 - p/q|$, which quantifies how close the value is to the rational approximation p/q. This measure $|N - p/q|$ is in fact a familiar quantity in number theory and as with all things familiar it is assigned a name: the Diophantine approximation. It is specifically used to measure how close a rational approximation p/q is to an irrational number N. Though the Diophantine approximation tells us how close the number is to a rational approximation, it doesn't tell us *how well* the rational number approximates it. Consider for example two rational approximations of the irrational number π: 22/7 and 1571/500. Both of these numbers are accurate to two decimal places but which one is a better approximation? If we look at the basic Diophantine approximation $|N - p/q|$ which measures the difference, then the latter fraction 1571/500 serves as a better approximation. This is not surprising as the precision is in increments of 1/500 and not 1/7. If, however, we consider how close it is as a fraction of the increment then we have $\frac{|N-p/q|}{1/q} = |N - p/q|q$ and we find that the approximation 1571/500 is accurate to 20% of an increment whereas the 22/7 approximation is accurate to within 1% of an increment. So it appears that 22/7 does uncannily well at approximating π given that the precision is a relatively coarse factor of 1/7. This is illustrated in figure 6.4.

In number theory the measure of how *well* a rational number p/q approximates an irrational number N is determined by the quantity $|N - p/q|q^2$, which can be considered as the fractional difference $|N - p/q|q$ expressed in units of $1/q$. It is the favoured quantity in several theorems such as Hurwitz's theorem, which states that there are infinitely many rational approximations to an irrational number such that $|N - p/q|q^2 < 1/\sqrt{5}$. These rational approximations are termed 'good' rational approximations. The approximation 22/7 counts as a good rational approximation because $|\pi - 22/7|7^2 = 0.061... < 1/\sqrt{5}$ whereas 1571/500 is a 'bad' approximation because $|\pi - 1571/500|500^2 = 101.8... \gg 1/\sqrt{5}$.

This section looks at this question of the commensurability of two frequencies and considers the emergence of quasiperiodic behaviour in driven systems, as theoretically explored in [14]. It is shown that those irrational numbers that admit poor rational approximations are better candidates for quasiperiodic behaviour in finite-time systems.

Incommensurability in the split-biharmonic drive

In this chapter we demonstrate the coupling between the transverse degrees of freedom using the split-biharmonic driving, and then show how this coupling is suppressed when the driving frequencies are incommensurate.

In the case of split-biharmonic driving, the symmetry analysis presented in

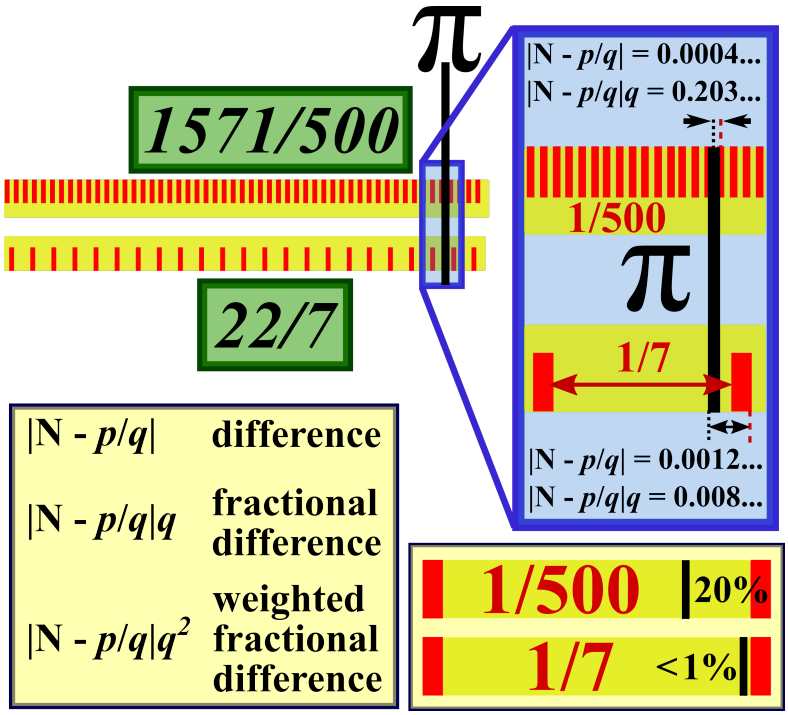

Figure 6.4: A depiction of the Diophantine approximation of an irrational number. The diagram shows two rational approximations - the 'bad' rational approximation 1571/500, and the 'good' rational approximation 22/7. Even though the bad rational is closer to the true value, the difference as a fraction of the unit is larger as shown by the box in the bottom right, which is roughly to scale. Therefore 22/7 provides a relatively better approximation to π when the size of the denominator is taken into account.

chapter 2 suggests that when ω_2 and ω_1 are incommensurate then no transport can occur as a result of the decoupling of the two directions and the resultant restoration of the shift-symmetry. Therefore, the transition from periodicity to quasiperiodicity for the split-biharmonic drive amounts to a transition from motion to no motion.

As suggested in the introduction, the incommensurability of two frequencies can only be established after a certain time, as irrationality is defined only in the infinite time limit. This means that the driving time T_d for which the atoms experience the split-biharmonic force becomes an important parameter when considering quasiperiodic systems, and we expect the transition to quasiperiodicity to be dependent on this time T_d.
In the next section the frequency commensurability as a function of the driving time T_d is considered.

6.3.1 Resonance width dependence on interaction time T_d

We now examine the time-dependence of the velocity when ω_2 is scanned about the primary value $2\omega_1$ for the split-biharmonic drive. Figure 6.5 shows experimental results for the resonance of ω_2 around $2\omega_1$ for different driving times T_d. There it is seen that the response of the system is time-dependent for values of ω_2 different to $2\omega_1$.

The 'peculiar' driving times of 7.24 ms and 14.5 ms in figure 6.5 correspond to 1024 waves and 2048 waves output at 141.42 kHz, these values being a remnant of my early attempts at quasiperiodicity (141.42 kHz may be recognised as $\sim \sqrt{2} \cdot 100$ kHz, and 1024/2048 being to do with the number of bits that the Agilent arbitrary waveform generator could output). The driving times of 10 ms, 20 ms, and 40 ms correspond to 1000 waves at 100 kHz, 1000 waves at 50 kHz, and 2000 waves at 50 kHz, respectively.

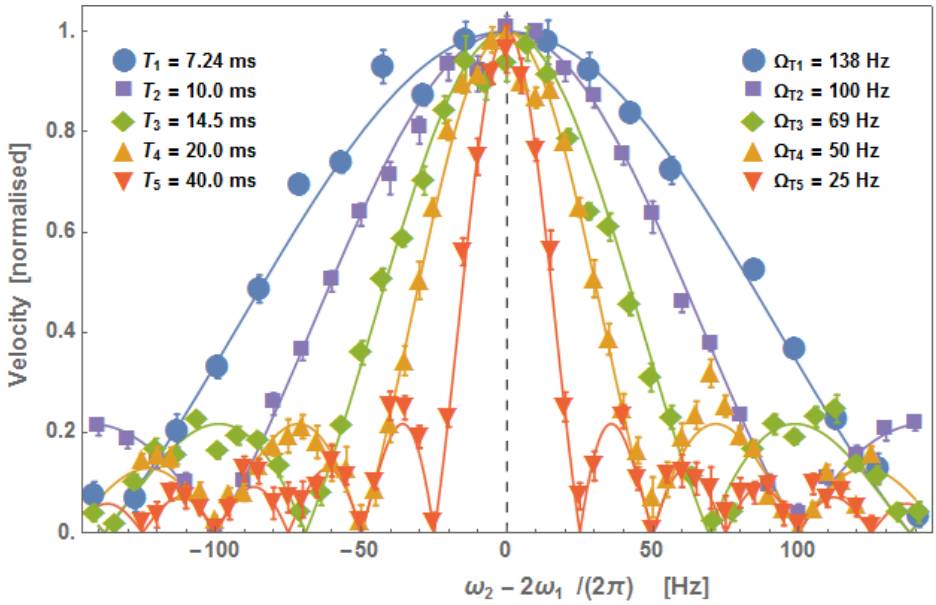

Figure 6.5: Maximum velocity as a function of ω_2 when ω_2 is scanned about $2\omega_1$ for various interaction times with the split-biharmonic driving. The plots display a narrowing of the linewidth for longer driving times. Each data point corresponds to a phase-scan from 0 to 2π in 13 steps, like that shown in figure 6.1, and the maximum velocity was extracted from the fitted sine curves. Behold!, this graph is the culmination of almost 14 000 images.

The results in figure 6.5 were obtained by scanning the relative phase ϕ from 0 to 2π in steps of $\pi/6$ and fitting the resulting curves with the function $v = v_0 \cos(\phi + \theta)$. This was done for each value of $\omega_2 - 2\omega_1$, represented by the x axis in figure 6.5. Therefore, the plot expresses the value of v_0 vs $\omega_2 - 2\omega_1$.

This means that when the velocity goes to zero in the above graph, it is zero for all values of the relative phase ϕ.

The solid lines represent a fit of

$$v_0 = v_{max}\,\mathrm{Sinc}\left[(\omega_2 - 2\omega_1)\frac{T_d}{2}\right].$$

If we define the width of a Sinc function Ω, such that $\mathrm{Sinc}(\frac{\pi x}{\Omega})$, then this Ω represents the value at which the function first becomes zero. Since our variable is in fact the frequency $x = f_2 - 2f_1$ and not the angular frequency, then the fitting equation is given by $v_0 = v_{max}\,\mathrm{Sinc}(2\pi x T_d/2)$, from which the width can be readily identified as

$$\Omega = \frac{1}{T_d}.$$

The significance of the results presented in figure 6.5 is that the atoms have an entirely different response to the driving fields for different driving times when ω_2 is not commensurate with ω_1. This is demonstrated in the plot, where the resonance width becomes narrower with time meaning that transport is suppressed at longer driving times. This can be interpreted as the atoms "realising" that the frequencies are not perfectly commensurate. In the case of our split-biharmonic driving, this realisation amounts to a drastic change of dynamics - the atoms stop moving. This is a striking result that the dynamics can completely change due to the time-dependent incommensurability.

This can in fact be interpreted as a dynamical decoupling of the degrees of freedom with longer driving times as a result of the incommensurability of the two frequencies. This decoupling causes the x and y directions to have independent shift-symmetry conditions and, in the case of our split-biharmonic driving, this means that transport is prohibited along x and along y due to separate and independent conditions.

Since the system's response to the incommensurability of two frequencies is time-dependent, in a finite-time experiment to guarantee quasiperiodic behaviour in a driven system one must ensure that the interaction time is long enough.

To illustrate this idea further, consider a driving with $\omega_2 \neq 2\omega_1$, but very close to it. On figure 6.6 this is indicated by the red dashed line that is offset from $2\omega_1$. For short driving times the system treats the two frequencies as commensurate. At longer times, and after more cycles, the system responds to the difference in frequency and transport is suppressed. This is demonstrated in figure 6.6 and the inset, which shows that transport goes to zero by simply increasing the driving time.

This is a remarkable result. A system that is driven by a force that produces transport at short times might be expected to also produce transport

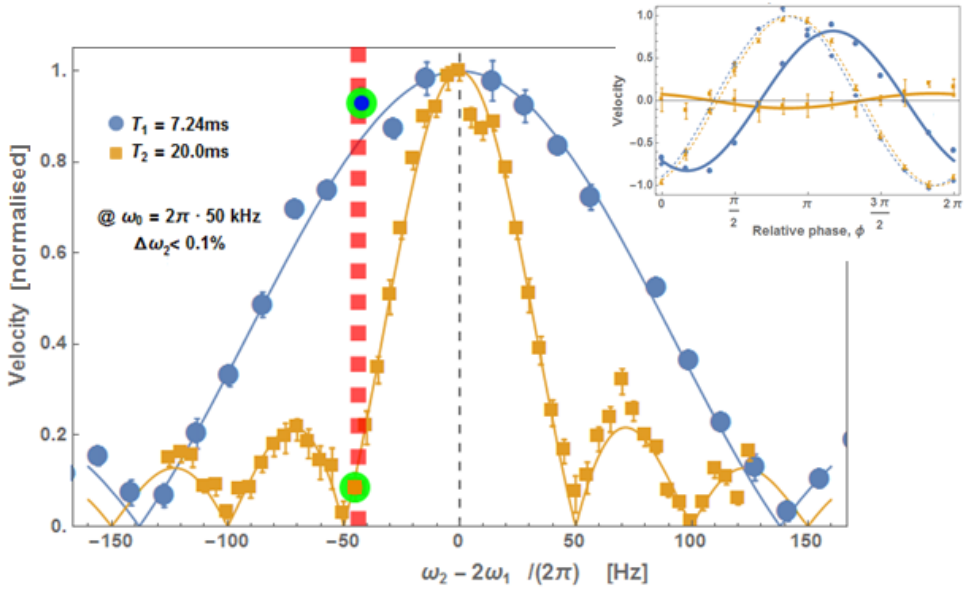

Figure 6.6: Suppression of transport with increasing driving time. The red dashed line corresponds to a frequency offset of less than 0.05 %, and the dynamics are already drastically changed. **Inset:** Split-biharmonic sine curves at green highlighted points for driving times of $T_d = 7.24$ms (blue) and $T_d = 20$ms (orange). The solid curves are for $\omega_2/\omega_1 \approx 1.999$ and the dashed curves are for $\omega_2/\omega_1 = 2$.

at longer times. If anything, it might be expected that the longer the driving is applied, the more transport is produced. But here it is the contrary; even though the driving produces transport at short times, as the driving time increases transport then ceases. This is a result of the time-resolution response of the system to the incommensurability of the two numbers. As the time is progressing, the system is responding to the fact that the two frequencies are incommensurate, resulting in the two directions becoming dynamically decoupled. For the split-biharmonic driving, this decoupling means that transport is forbidden along both directions due to independent shift-symmetry conditions.

As can be seen in the inset of figure 6.6, a phase-shift occurs that appears to be dependent on the interaction time when $\omega_2 - 2\omega_1$ is non-zero, but at $\omega_2 = 2\omega_1$ the phase-shift is time-independent. To explore this further, a plot was made of the phase-shifts θ corresponding to the fitted curves $v = v_0 \cos(\phi + \theta)$, for the different values of $\omega_2 - 2\omega_1$. The results are shown in figure 6.7, and they show a linear dependence with a gradient equal to $T_d/2$.

Combining this result that $\theta = \theta_0 + (\omega_2 - 2\omega_1)T_d/2$ with the fits from figure 6.5 $v_0 = v_{max}\,\mathrm{Sinc}((\omega_2 - 2\omega_1)T_d/2)$ determines the observed velocity

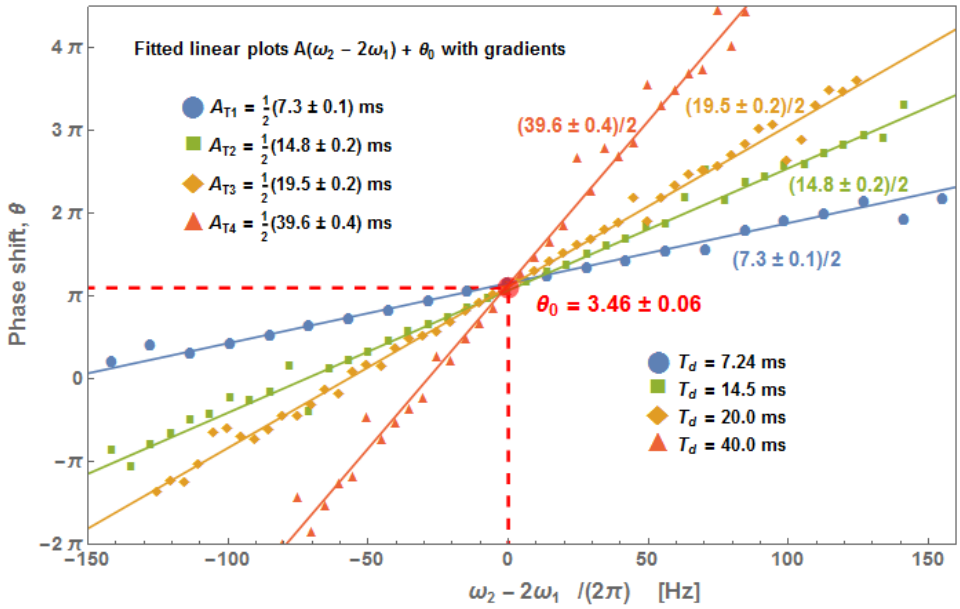

Figure 6.7: The phase-shift θ for the velocity function fit $v = v_0 \cos(\phi+\theta)$, showing a linear dependence with a gradient that scales with interaction time. The parameters for this measurement are the same as those in figure 6.5, where each data point corresponds to a phase-scan from 0 to 2π in 13 steps and the phase-shift was extracted from the fitted sine curves.

master equation for $p = 2$, $q = 1$, as

$$\begin{aligned} v &= v_0 \cos(\phi + \theta) \\ &= v_{max}\,\mathrm{Sinc}\left[(\omega_2 - 2\omega_1)\frac{T_d}{2}\right]\cos\left[\phi + \theta_0 + (\omega_2 - 2\omega_1)\frac{T_d}{2}\right]. \end{aligned}$$

The next section considers how the specific values of the frequency ratio affects the velocity resonance.

6.3.2 Resonance width dependence on q

In this section we explore how the values of p and q in the frequency ratio $\omega_2/\omega_1 = p/q$ affects the resonance width. In a similar way as was done with the driving times, we analyse how the maximum velocity and the phase of the velocity curves varies with $\omega_2 - (p/q)\omega_1$. The results are displayed in figure 6.8 and figure 6.9, and they show a narrowing of the linewidth that is proportional to q, as well as a proportional reduction in the maximum velocity.

The solid lines represent fits with the curve

$$v_0 = v_{max}\,\mathrm{Sinc}\left[(\omega_2 - \frac{p}{q}\omega_1)\frac{q\,T_d}{2}\right],$$

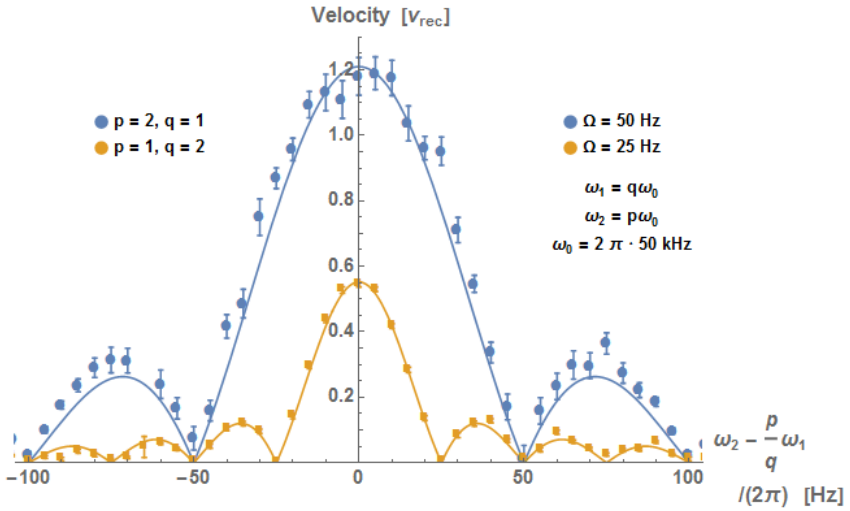

Figure 6.8: Split biharmonic driving for $p/q = 2$ and $p/q = 1/2$, showing a narrowing of the linewidth and reduction in the velocity that is proportional to q. The driving parameters for this experiment are $\omega = 2\pi{\cdot}50\,\text{kHz}$, $A = 2\,\text{V}$, $B = 1.5\,\text{V}$, $T_d = 20\,\text{ms}$. Velocity in units of $v_{rec} = 3.5\,\text{mm/s}$.

where the driving time was $T_d = 20\,\text{ms}$.

The plots of the corresponding phase-shifts are shown in figure 6.10. There it is seen that the gradient is proportional to q as well as T_d.

The velocity master equation is thus given by

$$\begin{aligned} v &= v_0 \cos(q\phi + \theta) \\ &= v_{max}\,\text{Sinc}\left[(q\omega_2 - p\omega_1)\frac{T_d}{2}\right]\cos\left[q\phi + \theta_0^{(q)} + (q\omega_2 - p\omega_1)\frac{T_d}{2}\right]. \end{aligned} \tag{6.1}$$

This result is in fact identical to the one derived in [9] and expounded upon in the supplementary material of [12] (see [13]), but in those papers it takes on a different form, namely:

$$v = v_{max}\frac{\sin\left[(q\omega_2 - p\omega_1)T_d + \theta\right] - \sin\left[\theta\right]}{(q\omega_2 - p\omega_1)\,T_d}. \tag{6.2}$$

To see how these are the same, we define $\alpha = (q\omega_2 - p\omega_1)\frac{T_d}{2} + \theta$ and $\beta = (q\omega_2 - p\omega_1)\frac{T_d}{2}$ such that $\alpha + \beta$ is the argument of the first sine function, and $\alpha - \beta$ is the argument of the second. Then we can readily use the identity $\sin(\alpha + \beta) - \sin(\alpha - \beta) = 2\sin(\beta)\cos(\alpha)$ to obtain

$$v = v_{max}\frac{\sin\left[(q\omega_2 - p\omega_1)T_d/2)\right]}{(q\omega_2 - p\omega_1)\,T_d/2}\cos\left[\theta + (q\omega_2 - p\omega_1)T_d/2\right],$$

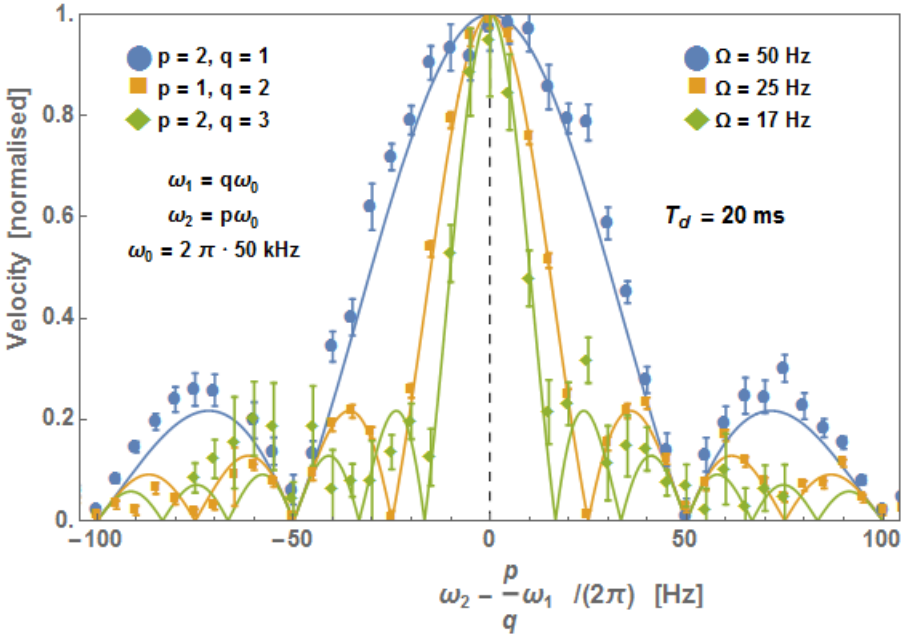

Figure 6.9: Split-biharmonic driving for different values of q, showing a proportional narrowing of the linewidth that is dependent on q and not dependent on p. The driving parameters for this experiment are $\omega = 2\pi \cdot 50\,\mathrm{kHz}$, $A = 2\,\mathrm{V}$, $B = 1.5\,\mathrm{V}$, $T_d = 20\,\mathrm{ms}$.

which is the experimentally determined result given in equation 6.1, where $\theta = q\phi + \theta_0$.
Since in an experiment we measure the cosine curves as a function of relative phase ϕ, then fitting to equation 6.1 is more applicable. In this case, it corresponds to the anticipated $\cos(q\phi + \theta_0)$ curve describing the periodic response, but with an additional phase-shift equal to $(q\omega_2 - p\omega_1)T_d/2$. This is then multiplied by a phase-independent amplitude envelope, which is a Sinc function with zeros separated by $2\pi/q\,T_d$.

6.3.3 Higher values of q and T_d

As was shown in the previous sections, the values of q and T_d have a direct impact on the measured ratchet velocity when ω_2 is different to $(p/q)\omega_1$. The key parameter is in fact the product $q\,T_d$, as is demonstrated in this section. In figure 6.11 the velocity profiles for $q = 2$ and $q = 3$ at various driving times are shown. There we see that the width scales inversely with $q\,T_d$.

The fact that the width depends on the product $q\,T_d$ means that the velocity profiles are not unique for different values of q. Indeed we can find different values of T_d such that the widths match each other, as is shown in figure 6.12a. The only feature that distinguishes the two profiles is the

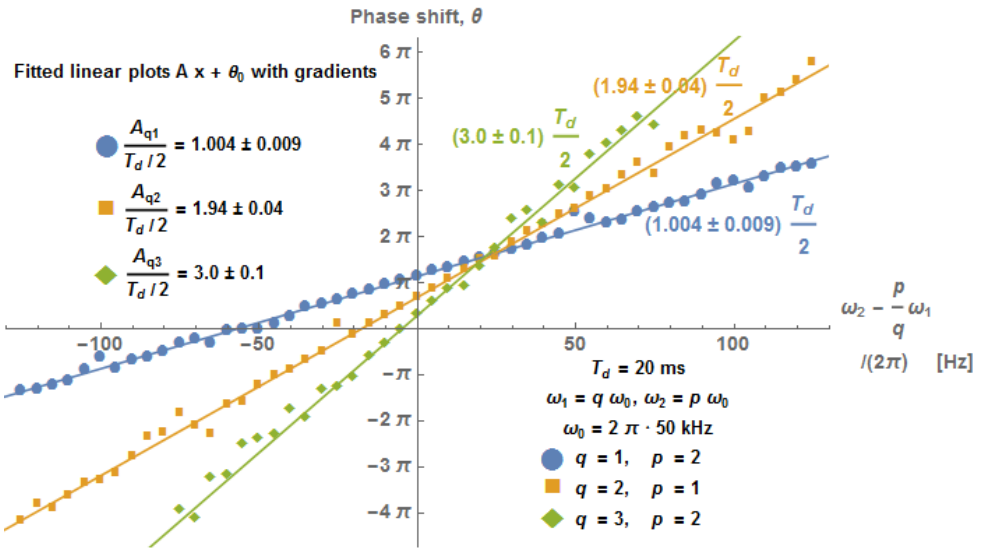

Figure 6.10: The phase-shift θ for the velocity function fit $v = v_0 \cos(q\phi + \theta)$, showing a linear dependence with a gradient equal to $qT_d/2$.

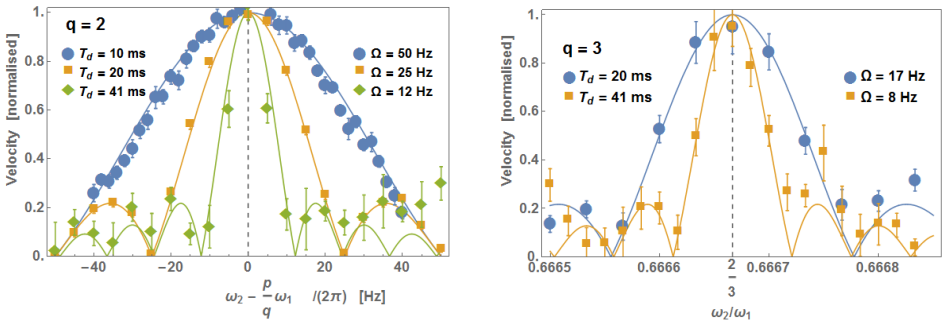

(a) $q = 2$ (b) $q = 3$

Figure 6.11: Narrowing of linewidth with time for $q = 2$ (left) and $q = 3$ (right).

maximum velocity, which scales inversely with q.

The dependence on the product also means that we can achieve quite drastic linewidth reductions with a relatively small range of q and T_d values, as is demonstrated in figure 6.13 where the linewidth is reduced by a factor 12 when q is changed from 1 to 3 and the atoms are modulated for just an additional 30 ms.

This portrays just how sensitive the transport is to the system parameters, showing entirely different behaviour (transport to no transport) for minor

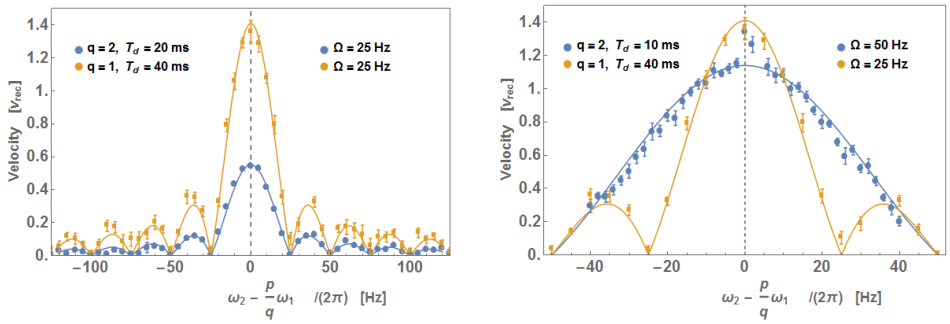

(a) Matching widths (b) $q = 1$ narrower than $q = 2$

Figure 6.12: Illustration of the fact that the different values of q and T_d can provide essentially the same velocity profiles. The effective parameter is in fact the product $q\,T_d$.

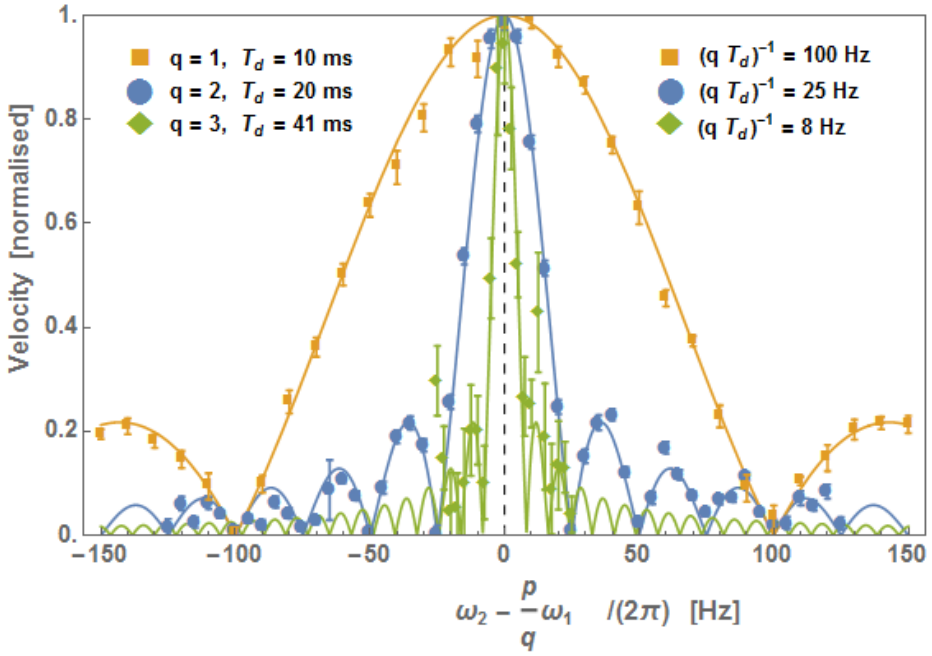

Figure 6.13: Narrowing of linewidth for various q and T_d showing drastic linewidth narrowing for minor parameter changes.

changes to parameter values.

6.3.4 Shift-symmetry zeros

In this section we explore the character of the zeros of the velocity resonance curve. It is shown that there are in fact two distinct 'types' of zero occurring, differing in their sensitivity to the driving phase ϕ. Figure 6.14 shows the

velocity as a function of $\Delta\omega_2 = \omega_2 - (p/q)\omega_1$ for a fixed driving phase, where the phase-sensitive and phase-insensitive zeros are both indicated.

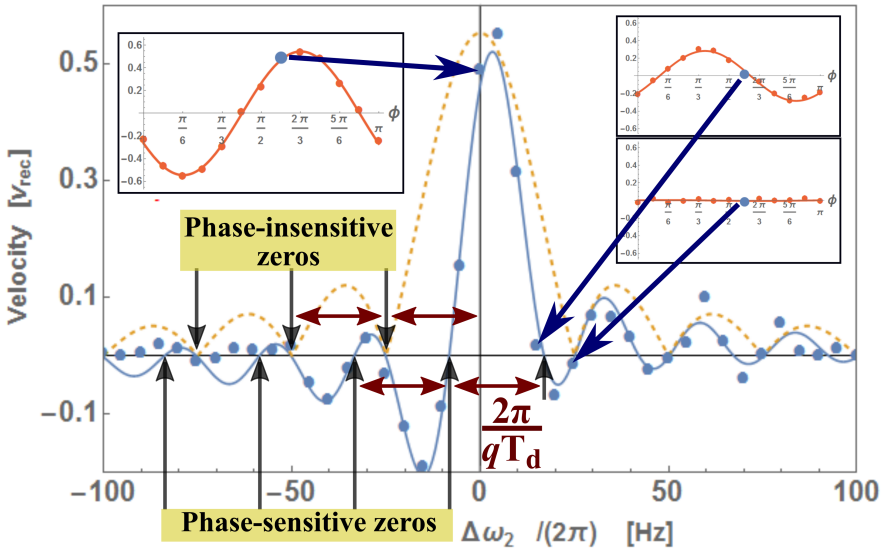

Figure 6.14: The measured velocity for fixed phase ϕ, depicting the two types of zero-crossing that occur. There are zeros that are dependent on the value of ϕ, and then there are zeros that are insensitive to ϕ. The parameters in the above graph are $\phi = 7\pi/2$, $q = 2$, $\theta_0 = 2.08$. The **insets** show the velocity when the phase ϕ is varied, portraying how the zero-crossings have a different phase-dependence. The highlighted point in each of the insets corresponds to $\phi = 7\pi/2$, which is plotted in the main graph.

The origins of the zeros can be traced to the shift-symmetry of the velocity, as will be described in this section. The following analysis relies on the results presented in [9, 12, 13] where it is shown that the periodic velocity v_{pq} possesses shift-symmetry on its argument, that is:

$$v_{pq}(\theta + \pi) = -v_{pq}(\theta) \tag{6.3}$$

where $\theta = q\phi + \theta_0$. This means that over a period of 2π any motion in one direction is balanced by motion in the opposite direction.

The equation for the finite-time average drift velocity v_{T_d} as a function of $\Delta\omega_2$ can be derived in the following rather neat way.
The drift velocity is given by the following general expression

$$v_{T_d} = \frac{1}{T_d}\int_0^{T_d} v(t)\,dt\,, \tag{6.4}$$

which is the average velocity over a driving time T_d.
A driving force that is given by $f(t) = \left\{\cos(\omega_1 t)\,,\, \cos(\omega_2^{(0)} t + \phi)\right\}$, where $\omega_2^{(0)} = (p/q)\omega_1$, results in a velocity $v(\phi) = \cos(q\phi + \theta_0)$ that is independent of time.
For $\omega_2 = \omega_2^{(0)} + \Delta\omega_2$, the driving force is given by
$f(t) = \left\{\cos(\omega_1 t)\,,\, \cos(\omega_2^{(0)} t + \Delta\omega_2 t + \phi)\right\}$, which equivalently results in a velocity $v(\phi + \Delta\omega_2 t) = \cos(q\phi + \theta_0 + q\Delta\omega_2 t)$ that is now a function of time. It is this latter form of the velocity that is used as $v(t)$ in the integral 6.4.

We now transform the integral 6.4 by setting $\theta = q\phi + \theta_0$ and redefining our time-dependent integration variable as $\theta' = \theta + q\Delta\omega_2 t$ such that $dt = d\theta'/(q\Delta\omega_2)$ and the limits on the integration become $\int_\theta^{\theta + q\Delta\omega_2 T_d}$. Then the finite-time average velocity is transformed to

$$v_{T_d} = \frac{1}{q\Delta\omega_2 T_d} \int_\theta^{\theta + q\Delta\omega_2 T_d} v(\theta')\, d\theta' \tag{6.5}$$

and upon substituting $v(\theta') = \cos(\theta')$ we obtain the previously stated equation 6.2, which, along with 6.5, was originally derived (by a different method) in [9, 12] and is repeated below:

$$v = v_{max} \frac{\sin\left(q\Delta\omega_2 T_d + \theta\right) - \sin(\theta)}{q\Delta\omega_2 T_d}\,.$$

This was shown to be equivalent to the result determined experimentally in this thesis given by equation 6.1, repeated here

$$v = v_{max}\,\mathrm{Sinc}\left[\Delta\omega_2 \frac{q\,T_d}{2}\right] \cos\left[\theta + \Delta\omega_2 \frac{q\,T_d}{2}\right].$$

This latter equation mathematically exposes the occurrence of the two types of zero - there are zeros of the Sinc function whenever $q\Delta\omega_2 T_d$ is a multiple of 2π, regardless of the phase θ – these shall be referred to as *phase-insensitive* zeros. Then there are zeros of the cosine function whenever $\theta + q\Delta\omega_2 T_d/2 = (n + 1/2)\pi$, which do depend on the value of the phase θ – these will be called *phase-dependent* zeros.

The origin of both of these zeros can be traced to the shift-symmetry properties of the velocity v_{pq} in equation 6.3. For the phase-insensitive zeros, the shift-symmetry property 6.3 means that when the velocity given in the integral 6.5 is averaged over a period of 2π – that is, when the integral $\int_\theta^{\theta + q\Delta\omega_2 T_d}$ is taken over $\int_\theta^{\theta + 2\pi}$ – then motion in one direction is cancelled by motion in the other direction and the net motion goes to zero. This means that there is zero transport at $\Delta\omega_2 = 2\pi/qT_d$, regardless of the driving phase θ, as a consequence of the shift-symmetry of the velocity v_{pq}.

Since these zeros are insensitive to variations in the phase θ they are robust against variations in experimental parameters, which typically affect θ

through its dependence on θ_0, which is a system-dependent phase-shift that is related to the dissipation in the system.

The above considerations have described the origin of the zeros occurring when $\Delta\omega_2$ is an integer (excluding zero) multiple of $2\pi/q\,T_d$, as indicated in figure 6.14.

The second type of zeros are phase-sensitive and occur whenever $\theta + q\Delta\omega_2 T_d/2 = (n + 1/2)\pi$. These phase-dependent zeros can also be traced back to the shift-symmetry condition given by equation 6.3; since the current reverses after a phase-shift of π then there must be a zero in the region $\theta \to \theta + \pi$. That is, aside from the phase-insensitive zero at $\Delta\omega_2 = 2\pi/qT_d$, there must be a zero in the region $\Delta\omega_2 = 0 \to \Delta\omega_2 = 2\pi/qT_d$. This zero is dependent on the value of the initial phase θ, contrary to the phase-insensitive zero at $\Delta\omega_2 = 2\pi/qT_d$.

The origin of the phase-dependent zeros can be seen geometrically by considering the measured velocity profiles as a function of phase. The earlier results of figures 6.7 and 6.10 demonstrated that the measured velocity as a function of phase attains a time-dependent phase-shift equal to $q\Delta\omega_2 T_d/2$. Therefore, for a fixed phase, there will be values of the phase-shift $q\Delta\omega_2 T_d/2$ such that the velocity becomes zero dynamically. This is represented in figure 6.15, which shows that the velocity profile can go to zero as a result of the time-dependent phase-shift that is incurred when $\Delta\omega_2$ is non-zero.

The above considerations have attempted to show that the zeros of the velocity resonance are of two types that possess different phase-dependencies. The zeros occurring at $\Delta\omega_2 = \pm 2\pi/q\,T_d$ and integer multiples thereof do not depend on the phase of the driving, but only depend on q and T_d, whereas the other type of zeros depend on the phase $\theta = q\phi + \theta_0$ as well as q and T_d.

Since the velocity resonance width narrows with time, as has been demonstrated earlier in this chapter, the positions of the zeros will also move towards the origin with increasing driving time. This means that with all parameters being fixed and with the frequency ω_2 in the vicinity of $(p/q)\omega_1$ (but not equal to it), the measured atom velocity will reduce to zero dynamically, and can even undergo current reversals. This is in contrast to the case when $\omega_2 = (p/q)\omega_1$ exactly, where no such dynamical reversals take place for fixed driving parameters.

6.3.5 Relation to quasiperiodicity

How does this relate to quasiperiodicity? Consider we have two frequencies, ω_1 and ω_2 such that ω_2/ω_1 is irrational. For our finite-time experiment, can we be certain that quasiperiodic behaviour will occur? For an irrational

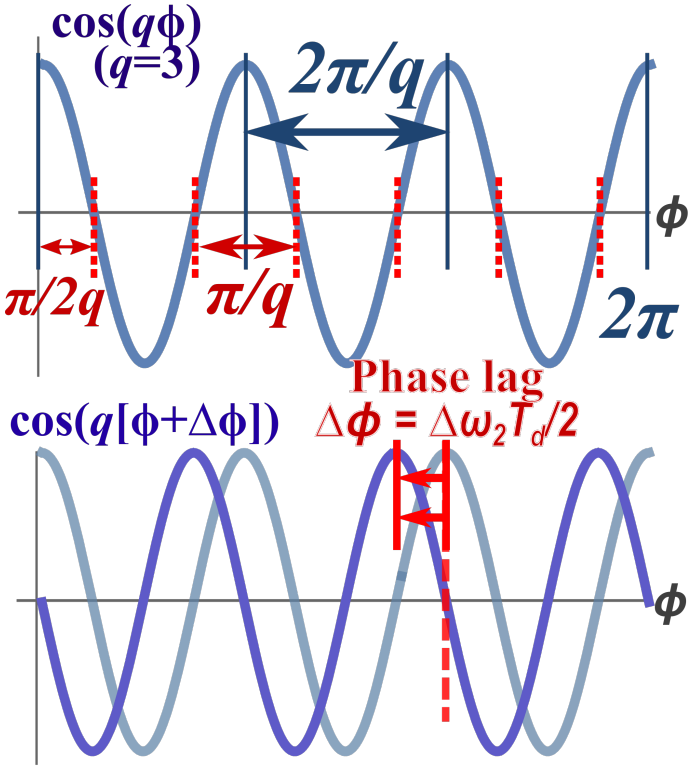

Figure 6.15: A depiction of how, for a fixed phase, the velocity goes to zero as a result of the time-dependent phase-shift of the measured velocity profile. These zeros are in general different to the phase-insensitive zeros, which are instead associated to the overall amplitude becoming zero.

ω_2/ω_1 there may exist certain rational approximations p/q such that in the time-frame of the experiment the system will behave periodically.

To put the discussion on firmer footing, let's consider a specific example where $\omega_2/\omega_1 = \pi$ is irrational and the ω_1 frequency is 1 Hz, so there's simply one wave per second and $T_1 = 1\,\mathrm{s}$. It may be presumed that since it is an irrational ratio then quasiperiodic behaviour is expected, but this is not necessarily the case for some time-periods as is demonstrated in figure 6.16.

The rational approximation 355/113 is close enough to the value of π that for a driving time of $T_d = 2000\,\mathrm{s}$ the frequency ratio lies within the resonance width for $q = 113$, $T_d = 2000\,\mathrm{s}$. This means that even though ω_2/ω_1 is irrational, periodic instead of quasiperiodic behaviour is observed. In the figure, with a driving time of $T_d = 2000\,\mathrm{s}$ the velocity is within 5 % of the

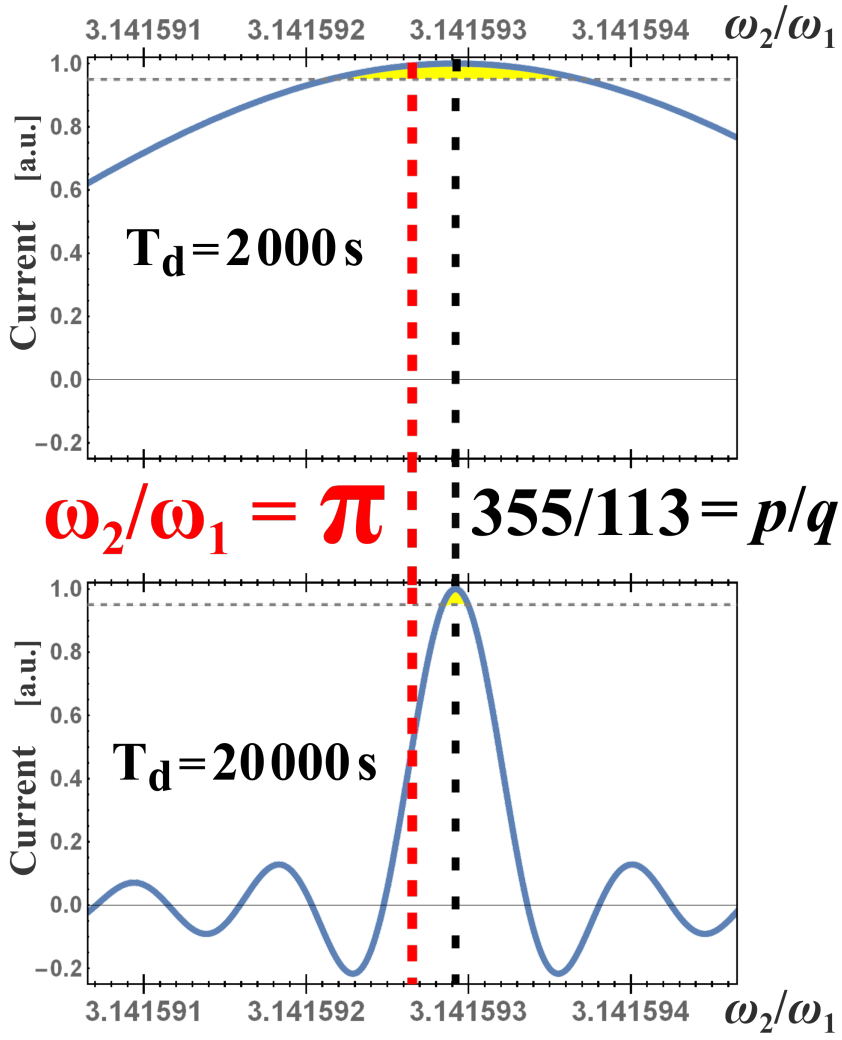

Figure 6.16: An irrational frequency ratio does not guarantee quasiperiodic behaviour, which would correspond to zero current in our case. As can be seen, there will be some time where the frequency ratio is well-approximated by a rational number p/q and the system behaves periodically.

periodic velocity even though ω_2/ω_1 is irrational.

This means that quasiperiodic behaviour can only be guaranteed when the width of the resonance is smaller than the closest rational approximation. Therefore quasiperiodic behaviour is only guaranteed for those irrational numbers with poor rational approximations and for long driving times.

6.3.6 Decoupling the degrees of freedom using quasiperiodic driving

Our experiments with the split-biharmonic driving have demonstrated that the x and y directions are coupled. If they weren't coupled transport would be prohibited for all values p, q, and ϕ because the shift-symmetry would hold along each direction independently. The fact that they're coupled, however, means that the shift-symmetry along one direction is dependent on the other, and we can exploit this fact to break this symmetry and observe transport. This transport is then in the direction of the shift-symmetry breaking direction, as was shown earlier in this chapter.

The situation changes, however, when the system is driven quasiperiodically such that ω_1 and ω_2 are incommensurate. A standard method for dealing with quasiperiodic systems is to treat the two incommensurate quantities as independent degrees of freedom [23]; in essence, increasing the dimensionality of the system as was discussed in chapter 2. How this translates to our split-biharmonic drive is that the two directions (driven by each frequency) become independent and decoupled when the driving frequencies are incommensurate. When the two directions are decoupled, the shift-symmetry along each direction is restored and transport is forbidden.

The coupling between the transverse degrees of freedom has further implications. We may consider two separate biharmonic drives along the x and y directions, given by

$$\begin{aligned} f_x(t) &= A\left[\cos(\omega_1 t) + \cos(2\omega_1 t + \pi/2)\right] \\ f_y(t) &= B\left[\cos(\omega_2 t) + \cos(2\omega_2 t + \pi/2)\right]. \end{aligned} \tag{6.6}$$

If we were to naïvely presume that the x and y directions are independent and decoupled, we would expect to observe transport with a magnitude and direction determined by the relative strengths A and B (with $\omega_2 = \omega_1$). We are wiser, however, because our split-biharmonic results have shown us that the transverse directions are in fact coupled. The impact of this is that the direction of motion is difficult to predict and is not a simple vector sum of the components. This has been demonstrated in previous experiments by our group [43] and by numerical simulations [14].

The decoupling of the degrees of freedom can be exploited, as is investigated in [14]. If we consider the driving given in equation 6.6, where we now use ω_2/ω_1 incommensurate, then with the degrees of freedom decoupled a more predictable direction of motion is expected, which is the vector sum of the components. This is demonstrated by numerical simulations in [14], which are displayed in figure 6.17.

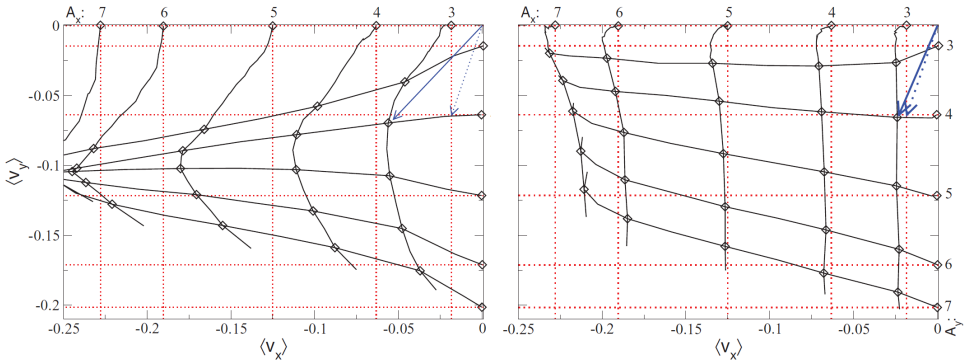

Figure 6.17: Numerical simulations by David Cubero showing that coupling between transverse degrees of freedom (exemplified on the left) is suppressed (right diagram) when ω_1 and ω_2 are incommensurate. This graph is from the paper [14].

6.3.7 Practical applications

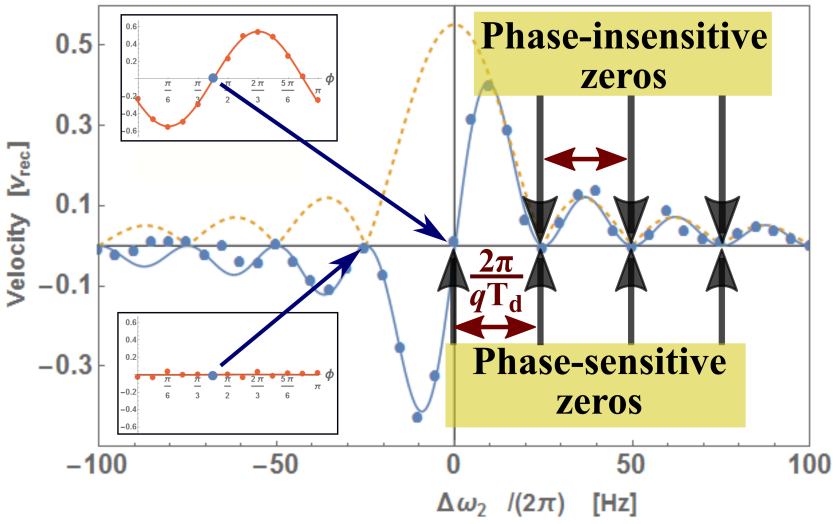

Figure 6.18: At the specific value of $q\phi + \theta_0 = 3\pi/2$ (or $\pi/2$) the phase-dependent restorations match the phase-insensitive zeros, except at the origin where there is a phase-dependent zero and a frequency-dependent current reversal. The parameters for this graph are $q = 2$, $\phi = 5\pi/12$, $\theta_0 = 2.08$, such that $q\phi + \theta_0 \approx 3\pi/2$.

In figure 6.18 the value of $q\phi$ has been chosen such that the phase-dependent zeros and the phase-insensitive zeros coincide, corresponding to $q\phi + \theta_0 \approx 3\pi/2$. This point is particularly interesting as there is a current

reversal around $\omega_2 = (p/q)\omega_1$, which means that atoms travel in opposite directions depending on whether ω_2 is bigger or smaller than it's closest rational approximation. This current reversal may be utilised to provide frequency-dependent separation mechanisms. Another noteworthy feature is that, aside from the current reversal at the origin, there are no further current reversals at higher and lower values, meaning that the separation mechanism would be robust. Also, the direction of motion can be used to determine whether the frequency is above or below the central value.

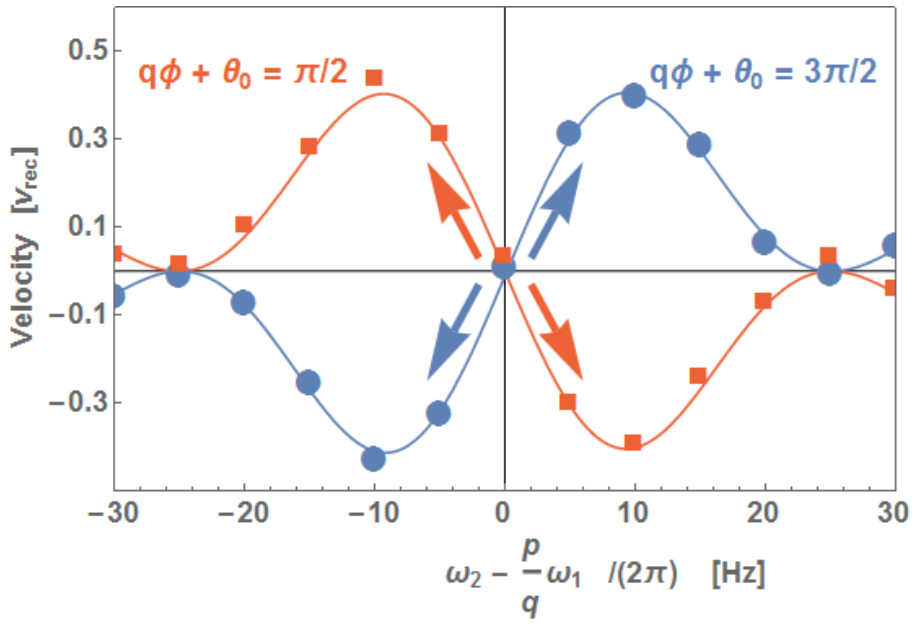

Figure 6.19: About the central frequency there is a current reversal, which can be exploited to provide frequency-sensitive motion. The sensitivity (gradient) about this point scales as $q\,T_d$.

The sensitivity of a device using this feature will then scale with q and T_d, since the gradient of the velocity about this centre point can be shown to scale as $v'(\Delta\omega_2 = 0) = v_{max}\sin(\theta)q\,T_d/2$, where $\theta = q\phi + \theta_0$. In the particular case where $\theta = 3\pi/2$ or $\pi/2$, then the magnitude of the gradient is maximised, and so these phases offer the most sensitive response as shown in figure 6.18. At these values of phase the gradient is equal to $\pm v_{max}\,q\,T_d/2$ respectively.

This feature may also have direct applications as a result of its sensitivity to various system parameters. If the phase ϕ is chosen so that $q\phi + \theta_0$ is equal to $3\pi/2$ (or its inverted counterpart at $\pi/2$) then a small change to any system parameter will displace the velocity curve. Any displacement of the velocity curve will result in transport in a specified direction, the direction being determined by the direction of the change. This changing parameter may be frequency, phase or even something more implicit such as noise strength [27]

or particle mass [9], which affect the phase-shift θ_0.

Utilising this feature as a mass separator, the phase ϕ may be set such that $q\phi + \theta_{th} = \pi/2$, where θ_{th} represents some threshold value that lies between the characteristic phases θ_0^{m1}, θ_0^{m2} of two masses $m1$, $m2$ so that they move in opposite directions. Here there is no explicit frequency-dependence but, as can be seen in figure 6.20, such a particle separator would be robust to small changes in frequency.

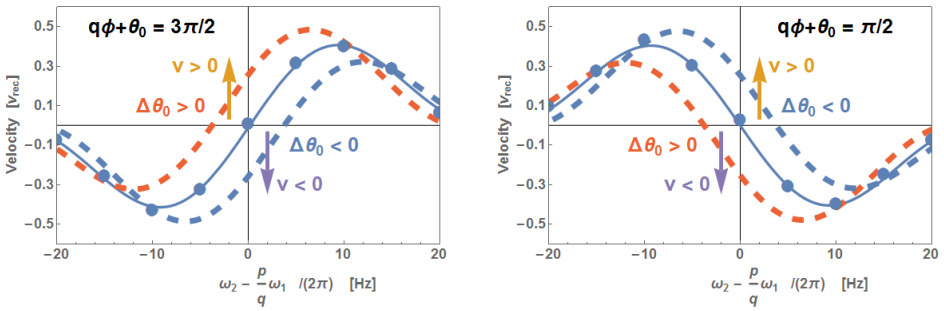

(a) $q\phi + \theta_0 = 3\pi/2$ (b) $q\phi + \theta_0 = \pi/2$

Figure 6.20: Illustration of how a change in θ_0, produced for example by different particle masses, can produce motion in opposite directions depending on the sign of the change. This has implications for use in separating particles about some threshold mass. Appropriate choice of the phase ϕ can achieve a positive or negative response.

What is particularly appealing is that one can use the value $\pi/2$ or $3\pi/2$ depending on whether one wants a positive or negative response about the central value, as depicted in figures 6.20a and 6.20b.

6.4 Summary

This chapter began by introducing the split-biharmonic driving as a fundamental example of a system demonstrating coupling between the transverse degrees of freedom. In the case of the split-biharmonic drive this coupling is clearly exposed by the fact that, if they weren't coupled, transport would be forbidden. Instead transport is observed due to the shift-symmetry conditions of one direction having an effect on the other direction, thereby exhibiting the coupling.

By exploring different values of p and q in the frequency ratio $\omega_2/\omega_1 = p/q$ it was demonstrated that motion occurs along the shift-symmetry breaking direction, but is shaped by the time-reversal symmetry. This extended the notion introduced in [62, 16] that the time symmetry shapes the current.

Analysis of the velocity for quasiperiodic driving for different values of q, T_d and ϕ allowed a precise determination of the shape of the functional curve, and an experimentally determined velocity master equation was derived. This was shown to be exactly equivalent to the equation theoretically derived in the literature [13].

By exploring the character of the zeros of the velocity resonance curve as a function of $\Delta\omega_2$ it was shown that there are two distinct types of zero occurring that are characterised by their dependence on the driving phase. The origin of both of these zeros was shown to be traceable to the shift-symmetry of the velocity.

Next it was considered how the velocity resonance width has implications for quasiperiodic driving and it was shown that quasiperiodic behaviour is only expected for irrationals with poor periodic approximations and for long driving times.

Then it was mentioned how this may be utilised to decouple the degrees of freedom, as theoretically explored in [14].

Finally, practical applications of the derived functional dependence were briefly considered. The feasibility for use as a particle separator was considered, and it was shown that transport is expected to be sensitive to system parameters, in some cases producing current reversals. These mechanisms differ from previous proposals as they rely on frequency-sensitive schemes.

So what's new?

The split-biharmonic driving, first introduced in [43] has been studied very little experimentally, even though it is exemplary for demonstrating the coupling between the transverse degrees of freedom. In this chapter, the split-biharmonic driving was studied for higher values of p and q for the first time, which allowed us to determine that the shift-symmetry governs the direction of motion.

Quasiperiodic behaviour in two dimensions for the split-biharmonic drive was also examined for the first time. The linewidth of the velocity resonance curve was extensively studied. It was observed that the measured velocity profile as a function of driving phase incurs a phase-shift that is proportional to the driving time. The velocity resonance zeros were shown to be of two distinct types, differing in their dependence on driving phase, and their origin was traced to the shift-symmetry of the velocity.

An experimentally determined velocity master equation was derived, which was shown to be equivalent to that derived theoretically in the literature [12]. Also, a novel theoretical derivation for the velocity equation was presented. The velocity equation was used to discuss possible frequency-dependent transport schemes.

Chapter 7

Discussion and Outlook

7.1 Results presented

This thesis described the development of an experiment to produce a cold atom ratchet in a two-dimensional optical lattice and, using this ratchet, explored the transition to quasiperiodicity in driven systems. It was demonstrated that the transition from periodicity to quasiperiodicity decouples the transverse degrees of freedom, which manifests as a suppression of ratchet current for our choice of driving. In order to demonstrate the coupling of the transverse degrees of freedom, a split-biharmonic drive was used. In this scheme the coupling is crucial for transport to occur and so a decoupling becomes clearly evident as going from a regime of transport to a regime of no transport.

This was the first extensive study of the split-biharmonic driving in a two-dimensional lattice.

It was experimentally demonstrated that the interaction time T_d and the value of q in the frequency ratio p/q determine the response of the system to quasiperiodic driving. This means that, in a real experiment, quasiperiodicity is only guaranteed for longer driving times and for irrational numbers that have poor rational approximations.

It was also demonstrated that the *direction* of the current corresponds to the direction of shift-symmetry breaking and the *shape* of the current is determined by the time-reversal symmetry, this latter fact being already suggested in the literature [62, 16]. This distinction between the effects of each symmetry was obscured in previous experiments due to the fact that the forces governing the shift-symmetry and time-reversal symmetry were directionally overlapped.

7.2 Future of the ratchet effect with cold atoms

In this section it is considered what lies in store for the ratchet effect.

First I present the next steps in relation to the results in this thesis, and those investigations that could be explored with the current setup of cold caesium atoms in a two-dimensional optical lattice. These are avenues I would have liked to venture had time permitted.

Then it is considered what may happen in the next generation of ratchet experiments in our lab. For this purpose the group has produced a Rb Bose-Einstein condensate. Already the experimental setup is promising on account of the ultra-cold Rb atoms in the double MOT system, with good optical access. This will provide longer holding times in the lattice and so provide a chance to better distinguish more subtle features. Not to mention the peculiar quantum characteristics that may introduce intriguing effects.

Further studies

There are some interesting extensions to the results presented in this thesis, based mainly on continuing the study of quasiperiodicity and how it may be used in some novel mechanisms.

7.2.1 Extending control of ratchet motion

The dependence of the atomic current on the values of T_d and q mean that one can manufacture interesting dynamics that are sensitive to system parameters, as was discussed at the end of chapter 6.
This can be further extended to some novel new schemes of operation using multiple frequencies - a so-called 'tri-harmonic' driving.

In two dimensions, one such scheme could mix the biharmonic driving introduced in chapter 5 with the split-biharmonic driving introduced in chapter 6, to form the following driving

$$\begin{aligned} f_x(t) &= A_x \cos(\omega_1 t) + B_x \cos(\omega_2 t + \phi_2) \\ f_y(t) &= B_y \cos(\omega_3 t + \phi_3)\,. \end{aligned}$$

Alternatively, a three-dimensional lattice could be used where the ω_1 harmonic drives the third 'z' axis, so that there is one harmonic driving each direction. In that case the x direction and the y direction are both essentially undergoing separate split-biharmonic drivings.

$$\begin{aligned} f_z(t) &= A_z \cos(\omega_1 t) \\ f_x(t) &= A_x \cos(\omega_2 t + \phi_2) \\ f_y(t) &= A_y \cos(\omega_3 t + \phi_3)\,. \end{aligned}$$

These two possible configurations (2D or 3D) are represented in figure 7.1.

There are a few interesting aspects about this. First, let us consider the 2D case with $\omega_1 = \omega$ and $\omega_2 = \omega_3 = 2\omega$. In this case we have the standard

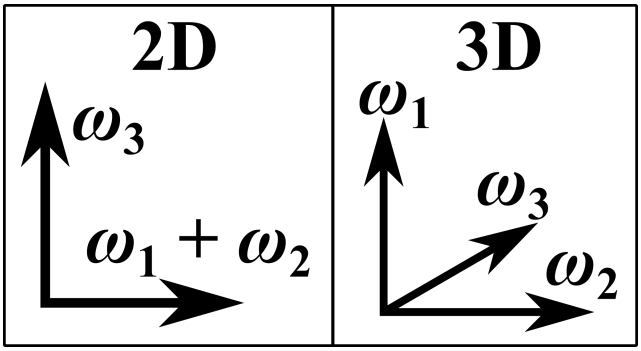

Figure 7.1: Examples of triharmonic driving. The frequency of the driving along each axis is labelled. The left panel is for a two-dimensional lattice, and the right panel is for a three-dimensional lattice. By controlling the relative frequencies of the driving, we may manufacture the desired frequency-dependent transport.

biharmonic along x and split-biharmonic along y. Therefore we expect to see transport along the respective directions depending on the values of ϕ_2 and ϕ_3. What is nice about this is that transport along both directions is immediately stopped if we switch off the first harmonic ($A_x = 0$).

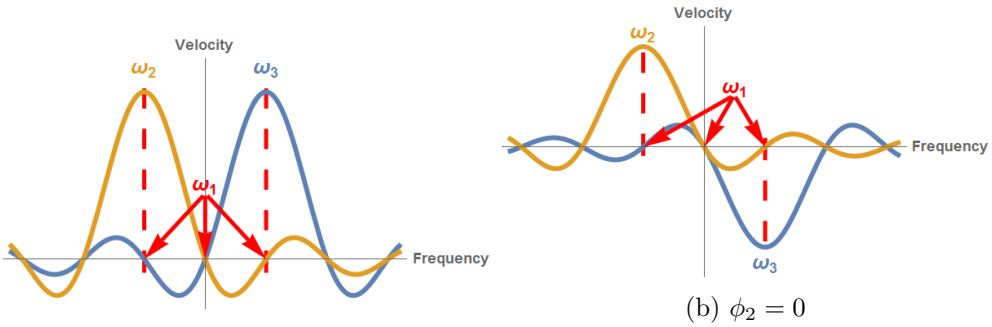

(a) $\phi_2 = \phi_3 = 0$

(b) $\phi_2 = 0$
$\phi_3 = \pi$

Figure 7.2: The frequency ω_1 can be varied so as to produce directed transport along one direction only, or no motion. This is a frequency-sensitive transport mechanism, for fixed phase of the driving.

Perhaps more interesting, however, is if we start playing with the mutual commensurabilities of ω_1, ω_2, ω_3. It is not clear what the extent of coupling is between ω_2 and ω_3 when they are almost equal. This can be investigated by analysing the motion along the y axis while varying B_x (or vice versa along x while varying B_y). We may flip-flop the value of ω_1 so that it changes its commensurability with each harmonic, thereby swapping directions of motion, as portrayed in figure 7.2.

Alternatively, it would be possible to fix ω_1 and then vary ω_2 and ω_3

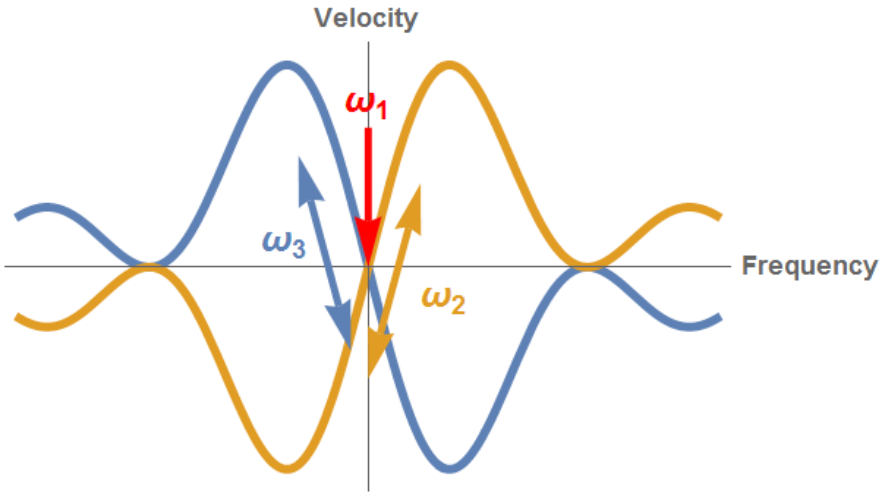

Figure 7.3: With ω_1 fixed, it is the frequencies ω_2 and ω_3 that determine ratchet motion. Specific values of their phases can be used to provide the required transport. The values of the phase are $\phi_2 = 3\pi/2$ and $\phi_3 = \pi/2$.

providing a frequency-dependent directional transport mechanism. This is represented in figure 7.3 where it is shown that a change in the frequency of ω_2 or ω_3 will produce a change in amount of transport. The phases can be chosen to produce the desired shift, and the sensitivity/gradient of the transport change is dependent on the value of the driving time T_d and the value of q.
Three-dimensional lattices also enable the creation of a blue-detuned optical lattice to trap atoms, which is not possible in two- or one-dimensional blue-detuned lattices. In a blue-detuned lattice the atoms sit at nodes where the intensity is a minimum. This means that atoms will scatter less light, and so the Hamiltonian regime of ratchets becomes more accessible.

7.2.2 Extension to studies of quasiperiodicity

As has been shown in chapter 6, there is a time-dependence of the motion for quasiperiodic driving. Since long driving times and short driving times exhibit such different behaviour, it is yet to be determined how crucial the continuity of the driving signal is. This is not considering the case of a pulsed ratchet, but rather something like an 'interrupted' ratchet, as the actual driving time is extended over a longer period than that associated to a pulse.

We may consider applying a quasiperiodic driving for a determined period of time, with brief periods of interruption, such as that shown in figure 7.4.

In that figure a quasiperiodic driving is cyclically ramped on for a certain time T_{on}, and off for a time T_{gap}. In order to understand why this is an interesting case we can look at the two limiting scenarios – the first where

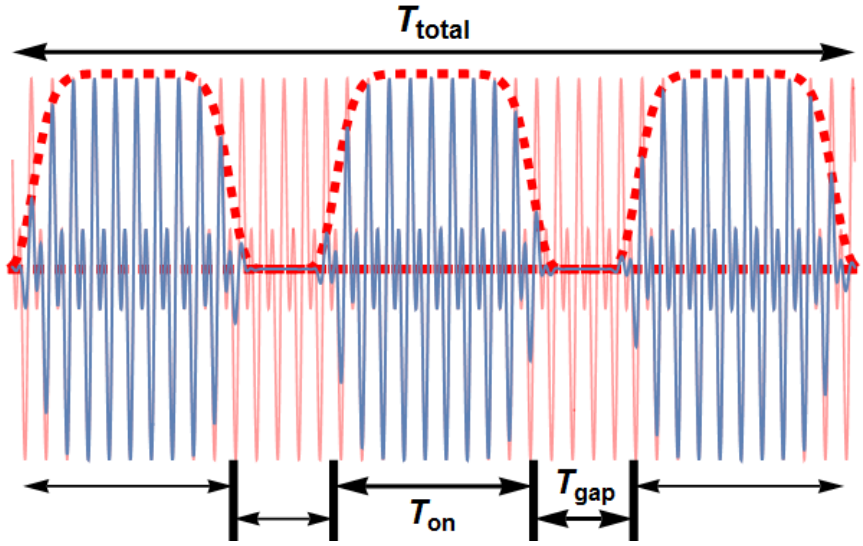

Figure 7.4: It is interesting to consider how the system transitions from an interrupted/slowly pulsed ratchet to a continuous ratchet. This can be explored using quasiperiodic driving as the two regimes correspond to different driving times, and this leads to entirely different behaviour when using quasiperiodic driving. This could perhaps provide some clues to relaxation mechanisms.

T_{gap} goes to zero, and the second where T_{gap} goes to some large value.

In the first scenario where T_{gap} is zero the driving time will become that of T_{total}, and so quasiperiodic behaviour is expected, which amounts to no transport for the split-biharmonic driving.

In the other scenario where T_{gap} is large, the atoms experience a driving of T_{on} (and not T_{total} as before), and they experience this driving multiple times. Therefore it is expected that the motion would correspond to the T_{on} time-period, which can be chosen to be a time-period that produces transport for split-biharmonic driving. So there is now an additional time-variable, T_{gap}, that produces two very different behaviours. It would be interesting to try to understand how the system transitions from one regime to the other. An initial presumption would be that it will depend on the level of dissipation and noise strength of the system, as this will determine the relaxation rate. Also, quantum ratchets would be expected to display a different response than classical ratchets as quantum ratchets are sensitive to the initial (and subsequent) conditions of the driving, in a sense preserving memory of the history of the driving. This is not the case with classical cold atom ratchets, which preserve no memory of initial conditions.

7.2.3 Bose-Einstein condensate in a ratchet

The next generation of ratchet experiments in our group hopes to explore a Bose-Einstein condensate (BEC) in a ratchet. A BEC is produced when atoms are cooled to quantum degeneracy, and the atomic ensemble behaves as a single coherent matter-wave.
A BEC in a ratchet would constitute a quantum ratchet, which renders it an intriguing subject on account of the peculiar features of a quantum ratchet, such as quantum resonances and a dependence on the initial driving phases [20, 19, 72]. Another feature of quantum ratchets that makes them interesting is that there exists another transport mechanism for atoms in the lattice, namely quantum tunnelling between lattice sites.

BECs can provide a test-bed for solid-state phenomena as there are some striking resemblances between the two fields and phenomena occurring in one often find a counterpart in the other.

One such example is the presence of vortices occurring in a BEC, which resemble the vortices occurring in a type-II superconductor associated to magnetic flux quanta. Such vortices can be generated in a BEC by rotating it and once the rotation stops the vortices remain in the BEC as a result of the superfluid state of the atoms [1].

Although the heart of a vortex represents an absence of the underlying fluid, the vortices display behaviours typically associated to particles, such as forming lattices (some with defects)[1] as well as nucleation of vortices [64]. Already the ratchet effect has been observed with superconducting vortices - or magnetic flux quanta - in solid-state systems [84, 74], but to my knowledge it has not yet been observed for vortices embedded in a BEC.

This is perhaps unsurprising as it would be technically very challenging. Examining the ratchet current of vortices in a BEC requires a different approach to observing the ratchet effect with the BEC itself. In the case of the ratchet effect with the BEC, it is the optical potential that is rocked, and the BEC undergoes ratchet transport. This already is non-trivial, as any near-resonant fields and strong perturbing rocking forces can excite the BEC cloud and destroy the quantum degeneracy. The solution lies in using a far-detuned optical lattice to provide a conservative potential; for a Rb BEC operating at 780 nm, a 1064 nm Nd-YAG laser is used.

This effect, however, is distinct from a vortex ratchet. For a vortex ratchet, its potential landscape is the matter field that it sits in. So the rocking force should perhaps be supplied by the BEC itself acting on the vortices, and not by the optical potential acting on the BEC. In this way, it may be the internal vibrational state of the BEC that provides the rocking force to produce vortex ratchet transport. This internal rocking could perhaps be induced by displacing the BEC from the centre of a harmonic trap, or even possibly may come about as a by-product of a ratchet driven BEC.

7.2.4 The ratchet effect in other fields

Parrondo's game [58] has displayed how the ratchet effect can make an appearance in contexts other than physical and biological. This is due to the fact that the two fundamental requirements of a ratchet are (1) a system out of equilibrium and (2) a broken symmetry. Therefore directed motion in other systems can not be precluded if these conditions are satisfied. One such alternative scheme for the ratchet effect may be in finance theory, as it is well known that share prices behave stochastically and are modelled by methods originally developed for stochastic mechanics.

Final remarks

Over one hundred years since its inception and the field of ratchets is burgeoning. This is on account of the recognition of its influence in biological processes and its potential for use in nano-technology, such as in particle pumps and nano-motors.

The ability to observe macroscopic quantum effects in a BEC, as well as in solid-state superconductors, has allowed experimental realisations of quantum ratchets.

Cold atoms in optical lattices provide an excellent test-bed for investigating ratchet phenomena, and particularly for investigating phenomena occurring in solid-state physics. This correlation between superfluidity in matter and superconductivity in electromagnetic systems is a neat manifestation of the underlying connection between the two fields, and is of course a hint of the unifying principal principle from which all of physics stems

... but that is the subject of my next thesis.

Part II

Rubidium Atomic Fountain Clock at NPL

Chapter 8

The Rubidium Atomic Fountain Clock

Once upon a time...

This chapter describes the work performed on the rubidium atomic fountain at the National Physical Laboratory (NPL) in Teddington to measure the hyperfine frequency-splitting of the rubidium-87 ground-state, which led to a new published result [57] and subsequent redefinition of the value by the International Bureau for Weights and Measures (BIPM) [7].

The chapter begins by briefly introducing the main features of an atomic fountain clock, and then goes on to describe the process for taking the measurements in that paper. Finally I present the results of the rubidium-87 ground-state hyperfine splitting frequency.

8.1 Atomic clocks

Man has had the need to keep track of the relentless progression of time since, well, a very long time ago. Conventionally we use a cyclical process with a seemingly constant rate – that way we can count the number of cycles and thus keep track of the 'time' elapsed. The cycles of the seasons constituted a year, the rotation of the Earth was a day, the swing of a pendulum a second. All of these clocks served well for their respective measurement intervals but for more precise definitions of time they are lacking. As the world developed there was a growing need for more accurate, more precise, and more stable clocks.

James Clerk Maxwell was first to posit some time in 1870 [76, 81] that the radiation of atoms could be used as a fundamental frequency standard in

an incredible act of foresight some seventy years before the first atomic clock was built at NPL in 1955 [21].

Atoms, which behave as tiny oscillators – or clocks, – make a good candidate as a universal time-keeper, since they are presumed to be the same throughout the Universe and not defined by our Earth's rotation rate (as in a day) or its gravitational field (as with a pendulum).

Humankind has currently adopted caesium-133 as its primary clock. Thus the second is *defined* by the hyperfine frequency-splitting of ^{133}Cs's ground-state, which is equal to 9 192 631 770 cycles per second. This is called the primary frequency standard and national labs around the globe act as their nations' timekeepers by constantly measuring the hyperfine splitting frequency of the caesium ground-state.

NPL was the first place in the world to build an atomic clock based on the caesium frequency standard and its caesium atomic fountain clock is currently rated as the most stable primary standard on Earth[1]. Its stability is so high that it would neither lose nor gain a second in 138 million years.

Precise knowledge of the time is critical to accurate navigation and atomic clocks form the back-bone of the global navigation satellite system and are now even used to time-stamp banking transactions for high-frequency traders.

Of course caesium is not unique in its ability to act as an oscillator. In fact it is not necessarily the best atom to use as it suffers from a large collisional cross-section at ultra-cold temperatures compared to other alkali-metals, such as rubidium. The lower collisional cross-section of rubidium reduces the frequency shifts due to background-gas collisions, as well as reducing the quantum projection noise and density fluctuations, allowing for better statistics. The rubidium hyperfine frequency-splitting is an officially endorsed secondary representation of the second and is sometimes the favoured choice as a clock on account of the lower collisional cross-section.

The current trend in time and frequency standards is a move towards optical frequency standards using the element strontium. This is because optical wavelengths are shorter and so the associated time-period of an optical oscillation is shorter than a microwave oscillation and it is possible to obtain even more precise time intervals. The expected stability of an optical clock is such that it would neither lose nor gain a second in the entire current age of the Universe.

8.2 Working principle of an atomic fountain clock

The general scheme of operation for an atomic fountain clock is shown in figure 8.1, the design of which is based on the rubidium atomic fountain at

[1] claim publicly announced in news articles and based on results in [48].

NPL built by Yuri Ovchinnikov.

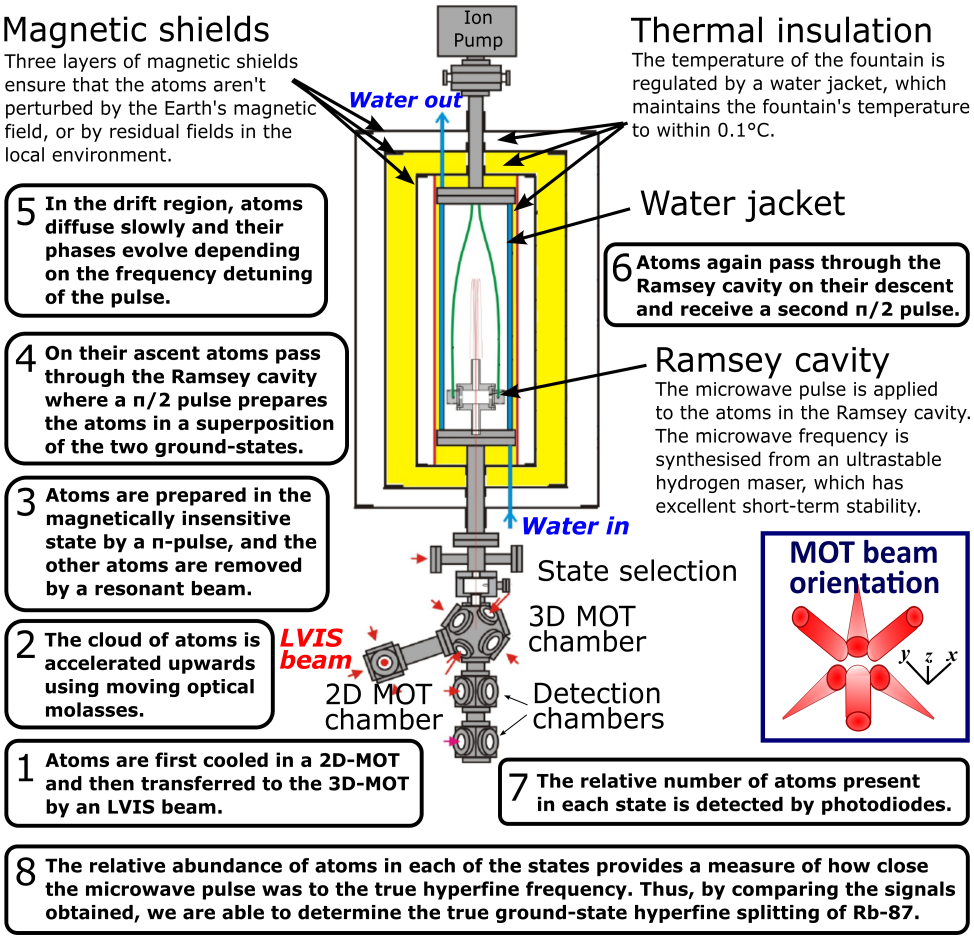

Figure 8.1: The working principle of an atomic fountain clock with the main steps of the experimental cycle numbered. Atoms are launched upwards in the fountain, undergo a Ramsey interaction, and then are detected at the bottom of the fountain. The fountain image was produced by Yuri Ovchinnikov but the annotations and beam orientation inset were added for this thesis.

Cold-atom preparation

Atoms are cooled in a 2D-MOT and transferred to the main MOT chamber by an LVIS[2] beam [54] where they are accumulated in the main six-beam MOT before being launched upwards in "moving molasses" [40], by detuning

[2]LVIS stands for **L**ow **V**elocity **I**ntense **S**ource (of cold atoms) [50]

the upward-pointing beams relative to the downward-pointing beams (the orientation of the six MOT beams is depicted in the inset of figure 8.1).

State-selection

On their ascent the atoms undergo state-selection, where atoms in the magnetically-insensitive $|F = 2, m_F = 0\rangle$ ground-state are transferred to the $|F = 1, m_F = 0\rangle$ ground-state by a resonant microwave π-pulse and the remaining atoms in $|F = 2\rangle$ are blown away by a resonant laser ('blown away' as in *gentle breath* not *violent explosion*!). This blowing-away laser is resonant to the $F = 2 \rightarrow F' = 3$ transition (which is the cooling transition) so the state-selected atoms in $F = 1$ are unaffected by it and they continue their flight into the Ramsey cavity. The state-selection process is depicted in figure 8.2.

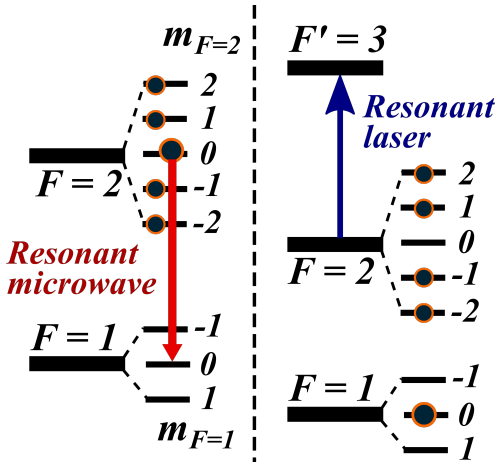

Figure 8.2: The state-selection procedure. A π-pulse induces a transition between the magnetically-insensitive ground-states, as shown on the left. The atoms remaining in the $F = 2$ ground-state are then removed by a beam resonant to the $F = 2 \rightarrow F' = 3$ transition. It may be noted that the π-pulse is also resonant to some other transition frequencies ($m_F = +1 \rightarrow -1$ and $m_F = -1 \rightarrow +1$) but these transitions are prohibited by selection rules.

Ramsey interaction

When the state-selected atoms enter the Ramsey cavity they receive a $\pi/2$ pulse, which transfers them to a coherent superposition of the two hyperfine ground-states. The atoms leave the cavity and their phases freely evolve in the drift region. On their return descent they pass through the Ramsey cavity a second time where they receive another $\pi/2$ pulse.

The purpose of the microwave pulses is explained next. The first $\pi/2$ pulse puts the atoms into a superposition of the two ground-states. If a second $\pi/2$ pulse were applied instantly then it would be equivalent to a π-pulse and all the atoms would be transferred to the $F = 2$ ground-state.
In the fountain, however, there is a diffusion time between the pulses as the atoms ascend, reach the apex and then descend under gravity. During this free-fall time the atoms' phases evolve. The phase-difference between the two states is proportional to the detuning of the pulse from the resonant frequency (as well as the diffusion time between the pulses, which is constant for a sequence of measurements).
If the microwave pulse is exactly resonant, the phase-difference between the two states is zero and all atoms are transferred to the $F = 2$ ground-state by the second $\pi/2$ pulse on their descent.
If the microwave pulse is non-resonant, however, then the two states accumulate a relative phase-difference and when the second $\pi/2$ pulse is applied, only a fraction of the atoms are transferred to the $F = 2$ ground-state.

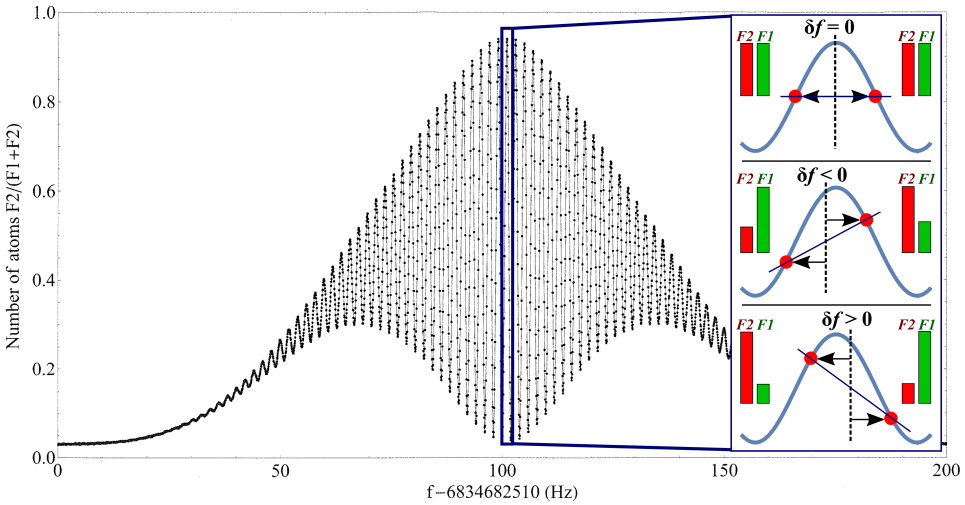

Figure 8.3: The measured Ramsey fringes of NPL's rubidium atomic fountain exhibiting the relative population in the $F = 2$ ground-state as a function of the microwave pulse detuning, where each point represents a single launch. The main graph was produced by Yuri Ovchinnikov. The **inset** portrays the split-Ramsey method used to determine the central frequency by hopping the frequency about the central fringe. The three diagrams illustrate three separate regimes of pulse detuning and indicate the relative number of atoms in the $F = 1$ and $F = 2$ states, which are equal when their mid-frequency is on resonance.

The evolution of the phase with respect to the microwave pulse detuning is depicted by Ramsey fringes, which shows the relative number of atoms

in the $F = 2$ ground-state when the pulse frequency is scanned about the resonant frequency. The Ramsey fringes for NPL's rubidium atomic fountain are shown in figure 8.3. The very centre of the fringes is a maximum and corresponds to the resonant pulse frequency where all atoms are transferred to the $F = 2$ ground-state.

The width of the entire Ramsey fringes is dependent on the time spent in the Ramsey cavity, and the width of the central peak is dependent on the evolution time between the pulses. This is the benefit of a fountain clock, where the free-diffusion time is longer than in traditional caesium clocks with two separated Ramsey cavities, allowing a narrower line-width about the centre frequency.

Atomic state measurement

After the atoms have undergone the Ramsey interaction, the number of atoms in each state is measured in the detection chambers. This is achieved by observing the fluorescence of the falling atomic sample. First, atoms in the $F = 2$ ground-state are detected by a beam resonant with the $F = 2 \rightarrow F' = 3$ transition. Then the atoms in the $F = 1$ ground-state are excited to the $F = 2$ ground-state by a repumping beam and then detected with the beam resonant to the $F = 2 \rightarrow F' = 3$ transition. This provides a measurement of the relative number of atoms in the $F = 2$ state, which is related to the frequency detuning of the pulse, as depicted in figure 8.3.

Split-Ramsey method

The actual process for measuring the central fringe frequency, corresponding to the ground-state hyperfine splitting frequency, uses the split-Ramsey method – sometimes called the method of separated oscillatory fields [65]. The measurement is performed by 'hopping' the pulse frequency between the two sides about the central fringe and determining the centre point, as depicted in the inset of figure 8.3. The amount by which the frequency is jumped corresponds to the FWHM of the central fringe, which is about 1 Hz for our rubidium fountain. When the beam is exactly resonant there is an equal number of atoms in each state and so the measurement of the number of atoms is fed back to the pulse-synthesiser in a servo loop in order to minimise the difference in population of each state.
After many measurements an accurate statistical average for the ground-state hyperfine splitting can be obtained by measurements of the relative atomic fluorescence in each state. This average value provides us with a measurement of the rubidium ground-state hyperfine splitting frequency or, in the case of the caesium frequency standard, is used to define the second.
The quantum projection noise [38, 73] is a consequence of the measurement procedure in the split-Ramsey method and is the limiting factor to the sta-

bility of an atomic fountain clock using this method. It arises from the fact that measurements are made about the half-maximum where atoms are in an equal superposition of the two ground-states. When the atoms are then measured, they are projected onto one of the two states $F = 1$ and $F = 2$ with equal probability. Therefore, there is some degree of uncertainty as to which state the atom will be projected to and only by gathering statistics with a large number of atoms can the distribution be accurately determined. This uncertainty is the source of the quantum projection noise, which scales as the inverse-root of the number of atoms $1/\sqrt{N}$ and so can be reduced by using a larger number of atoms. The quantum projection noise is at a maximum when the splitting ratio is 50–50, which corresponds to the regime of the split-Ramsey method, and so it limits the stability of an atomic fountain clock. In the NPL rubidium atomic fountain the flux of atoms from the LVIS to the main MOT is 8×10^9 atoms per second and so can provide a large number of atoms in a relatively short time.

8.3 The NPL rubidium atomic fountain

The rubidium atomic fountain at NPL was designed and built by Prof. Yuri Ovchinnikov, and its characterisation is given in [56, 47, 53, 55] and its design is shown in figure 8.1.

8.3.1 Modifications to existing fountain

There were several modifications made to the fountain during my time at NPL, including a modification to the vacuum system therefore breaking the ultra-high vacuum after six years undisturbed.

A new detection chamber was added beneath the existing detection chamber so that there would be a separate chamber for detecting each state in order to increase the signal-to-noise ratio and obtain better statistics. In the original design both states were detected in the same chamber, limiting the optical access and reducing the signal obtained by the CCDs. With the additional chamber, larger beams can be used to read out the number of atoms in each state.

When adding the new detection chamber to the existing fountain, the fountain had to be opened and so lost its vacuum. This was also beneficial as the fountain had been operating for several years and so rubidium vapour had accumulated. Opening the fountain and subsequently re-baking and pumping the system enabled a de-contamination after so many years in service. Improvement of the vacuum allows for cooler atoms due to reduced background-gas collisions and leads to better statistics.

Once the new detection chamber had been appended the system was baked and pumped. The baking was achieved by covering the entire (two-metre tall) fountain by a heat-proof blanket to act as a thermal insulator and placing several radiator heaters underneath the fountain. Thermocouples were positioned along the length of the fountain in order to monitor its temperature and there were also thermocouples embedded beneath the magnetic shields from the original construction. Particularly important were the thermocouples located next to the indium seals near the Ramsey cavity, since indium has a melting point of 156°C and so it was necessary to ensure the temperature didn't exceed this value.

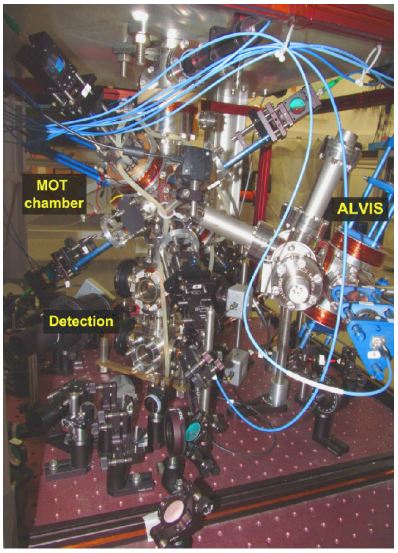

Figure 8.4: Photograph of the modified detection and surrounding optics, also showing the 2D-MOT and main MOT chambers. Light is delivered to the detection region by fibres. The additional detection chamber means that optical access is not limited and better statistics can be obtained.

With the new detection chamber in place the optical detection system was upgraded to take advantage of the enhanced optical access (figure 8.4). The upper detection chamber is used to measure the atoms in the $F = 2$ ground-state. A retro-reflected light-sheet is used to excite atoms by a $F = 2 \rightarrow F' = 3$ transition and the atom fluorescence is picked up by a CCD camera. The lower part of the beam is not retro-reflected in order to provide a free-running beam that pushes the atoms away. The remaining atoms are those in the $F = 1$ ground-state. In the lower detection chamber there is the repumping beam resonant to the $F = 1 \rightarrow F' = 2$ transition, which transfers atoms into the $F = 2$ ground-state. Then these atoms pass through a light-sheet resonant to the $F = 2 \rightarrow F' = 3$ transition and are detected by

a CCD.

8.3.2 Characterising the frequency shifts

There are many effects that shift the energy, and so frequency, of the atoms. These include all effects that perturb the system, such as magnetic fields, temperature, gravity, background-gas collisions, and even shifts from the microwave pulses used to probe the transitions.
These shifts must be accounted for and they are summarised in an "uncertainty budget", which gives details of the energy-shift produced by the effect as well as the uncertainty on that energy-shift value. The uncertainty budget for NPL's rubidium fountain is shown in figure 8.5.

Effect	Frequency shift (10^{-16})	Uncertainty (10^{-16})
Second order Zeeman	853.7	1.0
Black-body radiation	-133.5	0.5
Cavity distributed phase	0	0.9
Collisions with res. Gas	<0.2	0.2
Microwave lensing	-0.89	0.5
Microwave leakage	0	1.0
Gravity	12.6	0.3
Other	0	1.0
Total	732.11	**2.1**

Figure 8.5: The uncertainty budget of the rubidium fountain, characterising the systematic frequency shifts of the fountain. The total uncertainty is obtained by adding all the uncertainties in quadrature.

It is not necessarily the frequency shift that must be reduced, but rather it is the uncertainty of the shift that is most important for an accurate atomic clock. For example it is currently impossible to stop the effects of the Earth's gravitational field on the atoms but it is possible to try to characterise the effect well. If we have a good knowledge (low uncertainty) about how it is shifted, then we can account for this shift and thereby deduce the true frequency. Therefore, when using an uncertainty budget to determine how good a clock is, it is often the uncertainty on the shift that interests us most and not necessarily the actual magnitude of the shift.

The source of each shift is described briefly below but more in-depth descriptions can be found in [88].
The **second-order Zeeman shift** is a result of the non-zero magnetic field in the drift region as a result of the C-field coil, which is used to establish the

quantisation axis.
The **black-body radiation shift** is the energy shift due to the non-zero temperature of the environment. The uncertainty on this shift is minimised by using the temperature-stabilised water-jacket that maintains the temperature of the interrogation region to within ±0.1°C.
Collisions with residual gas also shift the energy of the atoms. This effect is less for rubidium-87 than for caesium because rubidium has a smaller collisional cross-section.
There is also a **gravitational** shift as a result of the general-relativistic redshift produced by the Earth.
Then there are a few shifts that are a result of the microwave interaction, these are distributed cavity-phase shift, cavity-pulling shift, microwave leaking and microwave lensing.
The **distributed cavity-phase shift** is a result of the atoms experiencing a varying phase of the microwave pulse during their trajectory.
The **cavity-pulling shift** is a result of the Ramsey-cavity resonance being detuned with respect to the atomic resonant frequency, which creates an effective shift on the measured frequency. This can be minimised by stabilising the cavity's temperature so that it is resonant to the atomic frequency.
The **microwave leaking** describes the energy perturbation to the atoms as a result of any microwave-field leaking into the drift-region of the chamber, where the atoms are meant to evolve undisturbed.
The **microwave lensing** shift arises from the non-uniformity of the microwave pulse across the finite-sized atomic sample, which produces an effective lensing of the atomic states that, upon detection, looks like a frequency shift, which must be accounted for.

Most of these shifts have been characterised previously [56, 55]. I participated in measuring the second-order Zeeman shift as well as characterising the cavity-pulling and black-body radiation shifts through taking temperature measurements. The measurements of the temperature stability, shown in figure 8.6, supply information for the uncertainty on the black-body radiation shift and the cavity-pulling shift. The temperature is regulated by a water jacket connected to a thermo-electric heater/cooler that maintains the fountain's temperature to within 0.1°C over many months.

There are two important reasons why the temperature must be stabilised. Firstly, the temperature is the source of the black-body radiation shift and so the temperature stability determines the uncertainty on this shift, which transfers to an uncertainty on our final measurements. The second reason accurate knowledge of the temperature is important is because the microwave cavity resonance condition is dependent on its temperature. The length of the cavity determines its resonant frequency and so thermal expansion of the aluminium cavity affects that resonance.

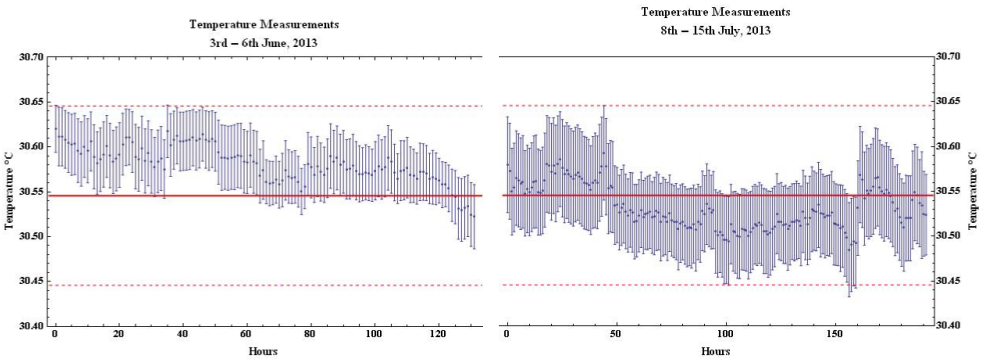

Figure 8.6: The temperature measurements of the atomic fountain show that the temperature is maintained to within ±0.1°C over months.

8.4 Absolute measurement of the rubidium-87 ground-state hyperfine splitting frequency

This section describes the measurement of the frequency-splitting between the $F = 1$ and $F = 2$ hyperfine levels of the $5^2S_{1/2}$ ground-state of ^{87}Rb.

The fact that it is an absolute measurement comes from our ability to directly reference it to the caesium atomic fountain primary frequency standard at NPL [80, 48], which defines the second in the UK. The rubidium and caesium fountains have frequency synthesisers that are locked to a single hydrogen maser at NPL, which works as an excellent short-term stable oscillator. This means that any shifts in the maser frequency are experienced by both fountains, and can be factored out. In this way a comparison of the rubidium frequency with respect to the primary frequency standard gives an absolute measurement.

8.4.1 Measurement procedure

In order to measure the hyperfine frequency averages are taken using the split-Ramsey method, as described previously.
The pulse frequency is hopped between the two sides of the central Ramsey fringe, the number of atoms is measured and the microwave pulse frequency is adjusted in a servo in order to maintain the frequency about the central fringe. The adjustments to the pulse frequency provide a measurement of the frequency offset and after averaging many measurements the centre frequency can be inferred very accurately. Figure 8.8 shows a graph of typical measurement results.

The frequency about which the value oscillates is the ground-state hyperfine splitting frequency inclusive of all systematic frequency shifts. Therefore, by using the knowledge of the measured systematic shifts we can calculate

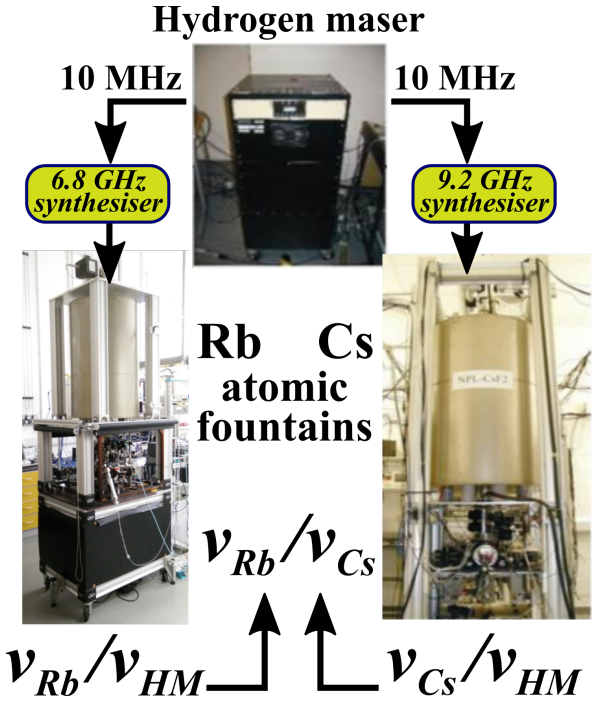

Figure 8.7: The inter-connection of the frequency standards at NPL, showing how the rubidium atomic fountain and caesium atomic fountain primary standard are referenced to the same hydrogen maser, thereby allowing us to cancel out relative shifts and obtain an absolute frequency measurement.

the unperturbed frequency.

The two types of uncertainty on this value are called type-A and type-B uncertainty. Type-A uncertainty represents the statistical uncertainty of the results like those measured in figure 8.8, and so is given as the standard error on the mean. Type-B uncertainty relates to the uncertainty on the systematic shifts as portrayed in the final column of the uncertainty budget in figure 8.5. The type-A and type-B uncertainties for the rubidium and caesium atomic fountains relevant to the measurements in this chapter are given in figure 8.9.

When measuring the absolute frequency of the rubidium ground-state hyperfine splitting, the results must be compared to the caesium fountain and so the uncertainty on the caesium fountain results must also be accounted for. This is accomplished by adding the uncertainties in quadrature to obtain the total uncertainty

$$\sigma_{TOT} = \sqrt{(\sigma_A^{Rb})^2 + (\sigma_B^{Rb})^2 + (\sigma_A^{Cs})^2 + (\sigma_B^{Cs})^2}\,.$$

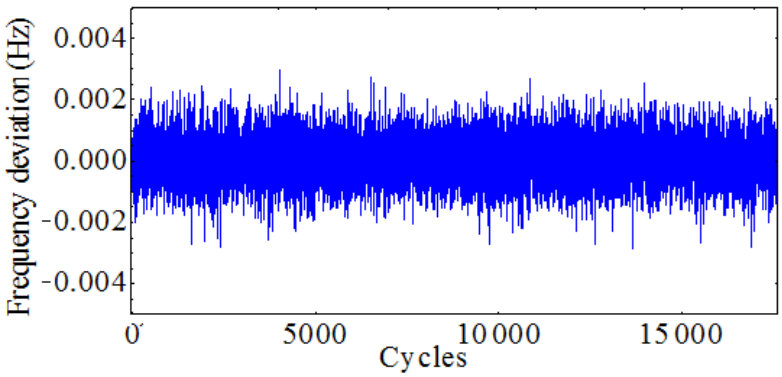

Figure 8.8: Typical graph of the microwave frequency, displaying how after many cycles we can obtain a statistically accurate mean value for the frequency. The statistical error on the mean contributes to the type-A uncertainty. The measured value includes all systematic shifts and so subtracting these shifts allows us to derive the true unperturbed frequency.

	2010	2012	2013
Integration time (hr)	238	330	132
$\sigma_{\mathrm{A}}^{\mathrm{Cs}}$ (10^{-16})	3.3	3.4	4.4
$\sigma_{\mathrm{B}}^{\mathrm{Cs}}$ (10^{-16})	2.0	2.0	2.0
$\sigma_{\mathrm{A}}^{\mathrm{Rb}}$ (10^{-16})	4.2	6.7	7.2
$\sigma_{\mathrm{B}}^{\mathrm{Rb}}$ (10^{-16})	3.7	2.4	2.4
Total uncertainty (10^{-16})	6.8	8.1	9.0

Figure 8.9: The type-A and type-B uncertainties of NPL's rubidium and caesium fountain frequency standards for the three measurement sessions.

8.4.2 Analysis of results

The frequency of an atomic fountain clock as measured in the lab f_m^{Rb} is a sum of the unperturbed frequency f_0^{Rb} plus any systematic shifts in the frequency f_{ss}^{Rb} minus any shift in the frequency of the microwave field used to measure the transition. That is

$$f_m^{Rb} = f_0^{Rb} + f_{ss}^{Rb} - \beta f_m^{Rb},$$

where β is the fractional error of the hydrogen maser's frequency given by $\beta = \frac{f^{HM} - f_0^{HM}}{f_0^{HM}}$. Since the caesium fountain is running concurrently and is referenced to the same hydrogen maser, the coefficient β is derived from the

caesium measurements. Therefore

$$\beta = \frac{f_0^{Cs} + f_{ss}^{Cs} - f_m^{Cs}}{f_m^{Cs}} ,$$

giving us a relatively simple expression for the rubidium-87 ground-state hyperfine splitting frequency:

$$f_0^{Rb} = f_m^{Rb} \left(\frac{f_0^{Cs} + f_{ss}^{Cs}}{f_m^{Cs}} \right) - f_{ss}^{Rb} . \tag{8.1}$$

The values on the right-hand side of equation 8.1 are all measured or defined. f_0^{Cs} defines the second, f_{ss}^{Cs} was measured at NPL by those in charge of the caesium fountain [48], f_m^{Cs} is constantly being measured and the values corresponding to the times of our measurement were extracted and used, f_{ss}^{Rb} was measured and characterised in [56], and f_m^{Rb} is of course the value we are measuring by averaging. Then from all of these an absolute measurement for the rubidium ground-state hyperfine splitting frequency f_0^{Rb} can be inferred.

8.4.3 Rubidium-87 ground-state hyperfine splitting frequency

Before the measurement at NPL, the recommended CCTF value[3] for the rubidium-87 ground-state hyperfine splitting frequency was based on measurements performed at LNE-SYRTE in Paris [33]. The CCTF found it "prudent" to increase the uncertainty threefold on account of it being based on a measurement performed at a single laboratory. Therefore this new measurement performed at NPL allows a more precise and conclusive definition of the frequency. Furthermore, another measurement at another location that agrees well with the original result also indicates the validity of the current approaches to frequency measurements.

There were three separate measurement sessions performed with NPL's rubidium atomic fountain – I participated only in the third measurement in 2013. The measurement results are as follows:

$$\begin{aligned} f_{Rb}(\text{NPL 2010}) &= 6\ 834\ 682\ 610.904\ 308(4.6)\,\text{Hz} \\ f_{Rb}(\text{NPL 2012}) &= 6\ 834\ 682\ 610.904\ 305(5.5)\,\text{Hz} \\ f_{Rb}(\text{NPL 2013}) &= 6\ 834\ 682\ 610.904\ 306(6.1)\,\text{Hz} . \end{aligned}$$

Combining these results gives an overall frequency of

$$\boxed{f_{Rb}(\text{NPL}) = \mathbf{6\ 834\ 682\ 610.904\ 307(3.1)\,Hz}}$$

[3] the report [6] for the previous recommended value can be found online at `https://www.bipm.org/utils/common/pdf/mep/87Rb_6834MHz_2013.pdf`.

The only other published independent values come from LNE-SYRTE, the most recent of which was in 2012 [32] with a value of f_{Rb}(SYRTE 2012) = 6 834 682 610.904 312(3) Hz, and so combining this with our measured value gives a final result for the ground-state hyperfine splitting frequency as

$$f_{Rb}(\text{NPL \& SYRTE}) = \mathbf{6\ 834\ 682\ 610.904\ 310(2.4)\ Hz}$$

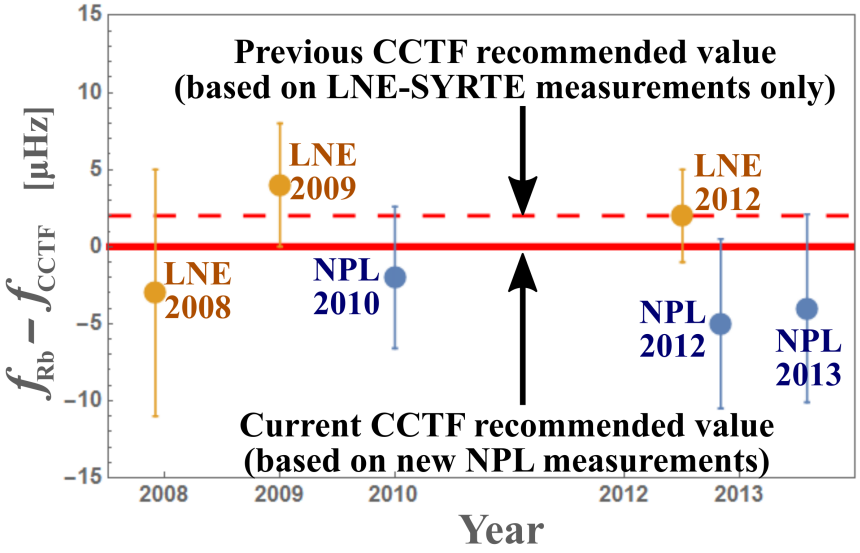

Figure 8.10: A graph of the rubidium-87 frequency measurements over previous years. The official recommended value has been adjusted in 2015 [7] based on the newly published [57] measurements at NPL.

Figure 8.10 displays the results of measurements performed over previous years by NPL and LNE-SYRTE, so far the only two places to have published values for this secondary frequency standard.

This new measurement has already been incorporated into the BIPM recommended values[4] and the recommended rubidium-87 frequency has been adjusted accordingly.

[4]The report [7] for the new recommended value based on our result can be found online at `https://www.bipm.org/utils/common/pdf/mep/87Rb_6.8GHz_2015.pdf`.

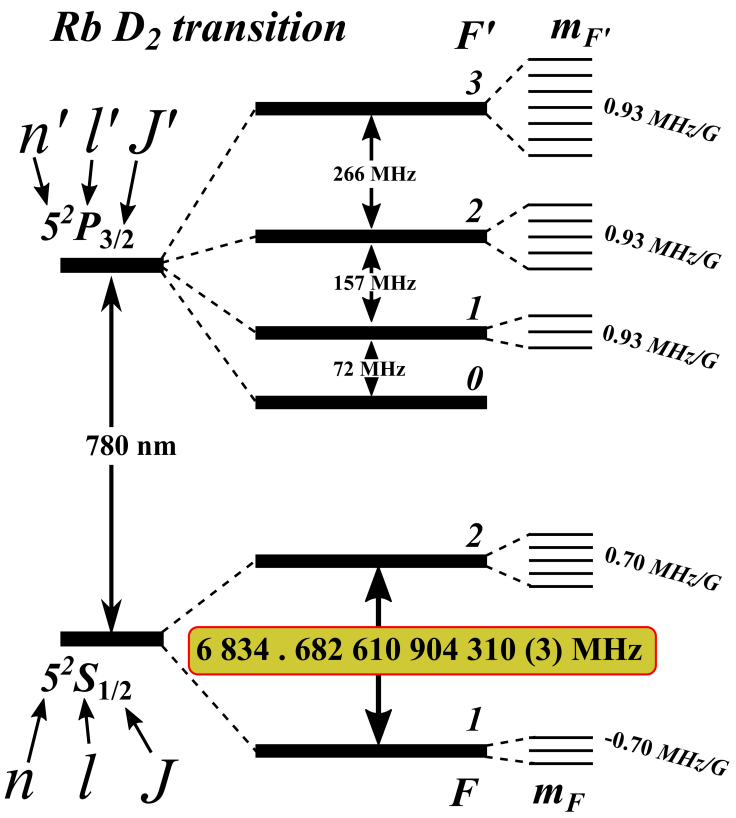

Figure 8.11: The hyperfine energy levels for the ^{87}Rb D_2 transition at 780 nm. The diagram was inspired by Daniel Steck's rubidium-87 D-line data [77] and the values were taken from that paper except for the highlighted value for the ground-state splitting, which is the central and new result presented in this chapter.

8.5 Summary

This chapter described the procedure for the measurement of the ^{87}Rb ground-state hyperfine splitting frequency using the rubidium atomic fountain at NPL. The fact that the rubidium fountain is driven by the same hydrogen maser as the caesium primary frequency standard at NPL means that it is possible to make an absolute measurement of the rubidium hyperfine frequency-splitting.

The new published result has corroborated the previous measurements performed at LNE-SYRTE, the only other laboratory to have published a measurement, and has resulted in a redefinition of the rubidium-87 ground-state hyperfine splitting frequency, which is currently the most popular secondary frequency standard used in practice.

Bibliography

[1] Abo-Shaeer, J. R., Raman, C., Vogels, J. M., and Ketterle, W. Observation of Vortex Lattices in Bose-Einstein Condensates. *Science 292*, 5516 (2001), 476–479.

[2] Anderson, M. H., Ensher, J. R., Matthews, M. R., Wieman, C. E., and Cornell, E. A. Observation of Bose-Einstein Condensation in a Dilute Atomic Vapor. *Science 269*, 5221 (1995), 198–201.

[3] Astumian, D., and Hänggi, P. Brownian Motors. *Physics Today 55* (Feb 2002), 33.

[4] Astumian, R. D., and Bier, M. Fluctuation Driven Ratchets: Molecular Motors. *Phys. Rev. Lett. 72* (Mar 1994), 1766–1769.

[5] Bartussek, R., Hänggi, P., and Kissner, J. G. Periodically Rocked Thermal Ratchets. *EPL (Europhysics Letters) 28*, 7 (1994), 459.

[6] BIPM. Recommended values of standard frequencies for applications including the secondary representations of the definition of the Second, 2013 – Rubidium 87.
available online at
`https://www.bipm.org/utils/common/pdf/mep/87Rb_6834MHz_2013.pdf`.

[7] BIPM. Recommended values of standard frequencies for applications including the practical realization of the Metre and secondary representations of the definition of the Second, 2015 – Rubidium 87.
available online at
`https://www.bipm.org/utils/common/pdf/mep/87Rb_6.8GHz_2015.pdf`.

[8] Brillouin, L. Can the Rectifier Become a Thermodynamical Demon? *Phys. Rev. 78* (Jun 1950), 627–628.

[9] Casado-Pascual, J., Cubero, D., and Renzoni, F. Universal Asymptotic Behavior in Nonlinear Systems Driven by a Two-Frequency Forcing. *Phys. Rev. E 88* (Dec 2013), 062919.

[10] Chu, S., Hollberg, L., Bjorkholm, J. E., Cable, A., and Ashkin, A. Three-Dimensional Viscous Confinement and Cooling of Atoms by Resonance Radiation Pressure. *Phys. Rev. Lett. 55* (Jul 1985), 48–51.

[11] Cohen-Tannoudji, C., and Phillips, W. D. New Mechanisms for Laser Cooling. *Physics Today 43*, 10 (1990), 33–40.

[12] Cubero, D., Casado-Pasqual, J., and Renzoni, F. Irrationality and Quasiperiodicity in Driven Nonlinear Systems. *Phys. Rev. Lett. 112* (2014), 174102.

[13] Cubero, D., Casado-Pasqual, J., and Renzoni, F. Irrationality and Quasiperiodicity in Driven Nonlinear Systems - Supplemental Material. *Phys. Rev. Lett. 112* (2014), 174102.

[14] Cubero, D., and Renzoni, F. Control of Transport in Two-dimensional Systems via Dynamical Decoupling of Degrees of Freedom with Quasiperiodic Driving Fields. *Phys. Rev. E 86* (Nov 2012), 056201.

[15] Cubero, D., and Renzoni, F. *Brownian Ratchets: From Statistical Physics to Bio and Nano-motors*. Cambridge University Press, 2016.

[16] Cuesta, J. A., Quintero, N. R., and Alvarez-Nodarse, R. Time-Shift Invariance Determines the Functional Shape of the Current in Dissipative Rocking Ratchets. *Phys. Rev. X 3* (Nov 2013), 041014.

[17] Dalibard, J., and Cohen-Tannoudji, C. Laser Cooling Below the Doppler Limit by Polarization Gradients: Simple Theoretical Models. *J. Opt. Soc. Am. B 6*, 11 (Nov 1989), 2023–2045.

[18] Davis, K. B., Mewes, M. O., Andrews, M. R., van Druten, N. J., Durfee, D. S., Kurn, D. M., and Ketterle, W. Bose-Einstein Condensation in a Gas of Sodium Atoms. *Phys. Rev. Lett. 75* (Nov 1995), 3969–3973.

[19] Denisov, S., Morales-Molina, L., and Flach, S. Quantum Resonances and Rectification in AC-Driven Ratchets. *EPL (Europhysics Letters) 79*, 1 (2007), 10007.

[20] Denisov, S., Morales-Molina, L., Flach, S., and Hänggi, P. Periodically Driven Quantum Ratchets: Symmetries and Resonances. *Phys. Rev. A 75* (Jun 2007), 063424.

[21] Essen, L., and Parry, J. An Atomic Standard of Frequency and Time Interval: A Caesium Resonator. *Nature 176* (1955), 280–282.

[22] Feynman, R. *The Feynman Lectures*, vol. 1. Addison-Wesley, 1964.

[23] Flach, S., and Denisov, S. Symmetries and Transport with Quasiperiodic Driving. *Acta Phys. Pol. B 35* (Mar 2004), 1437.

[24] Flach, S., Yevtushenko, O., and Zolotaryuk, Y. Directed Current due to Broken Time-Space Symmetry. *Phys. Rev. Lett. 84* (Mar 2000), 2358–2361.

[25] Ganichev, S. D., Tarasenko, S. A., Olbrich, P., Karch, J., Hirmer, M., Mller, F., Gmitra, M., Fabian, J., Yakimova, R., Lara-Avila, S., Kubatkin, S., Wang, M., Vajtai, R., Ajayan, P. M., Kono, J., and Drexler, C. Magnetic Quantum Ratchet Effect in Graphene. *Nature Nanotechnology 8* (June 2013), 104–107.

[26] Gommers, R. *Symmetry and Transport in Cold Atom Ratchets*. PhD thesis, University College London (UCL), June 2007.

[27] Gommers, R., Bergamini, S., and Renzoni, F. Dissipation-Induced Symmetry Breaking in a Driven Optical Lattice. *Phys. Rev. Lett. 95* (Aug 2005), 073003.

[28] Gommers, R., Denisov, S., and Renzoni, F. Quasiperiodically Driven Ratchets for Cold Atoms. *Phys. Rev. Lett. 96* (Jun 2006), 240604.

[29] Gommers, R., Douglas, P., Bergamini, S., Goonasekera, M., Jones, P. H., and Renzoni, F. Resonant Activation in a Nonadiabatically Driven Optical Lattice. *Phys. Rev. Lett. 94* (Apr 2005), 143001.

[30] Gorre, L., Ioannidis, E., and Silberzan, P. Rectified Motion of a Mercury Drop in an Asymmetric Structure. *EPL (Europhysics Letters) 33*, 4 (1996), 267.

[31] Grynberg, G., Lounis, B., Verkerk, P., Courtois, J.-Y., and Salomon, C. Quantized Motion of Cold Cesium Atoms in Two- and Three-dimensional Optical Potentials. *Phys. Rev. Lett. 70* (Apr 1993), 2249–2252.

[32] Guéna, J., Abgrall, M., Clairon, A., and Bize, S. Contributing to TAI with a secondary representation of the SI second. *Metrologia 51*, 1 (2014), 108.

[33] Guéna, J., Rosenbusch, P., Laurent, P., Abgrall, M., Rovera, D., Lours, M., Santarelli, G., Tobar, M. E., Bize, S., and Clairon, A. Demonstration of a Dual Alkali Rb/Cs Atomic Fountain Clock. *IEEE Transactions on Ultrasonics, Ferroelectrics and Frequency Control 57* (2010), 647.

[34] Guidoni, L., Triché, C., Verkerk, P., and Grynberg, G. Quasiperiodic Optical Lattices. *Phys. Rev. Lett. 79* (Nov 1997), 3363–3366.

[35] Guidoni, L., and Verkerk, P. Optical Lattices: Cold Atoms Ordered by Light. *Journal of Optics B: Quantum and Semiclassical Optics 1*, 5 (1999), R23.

[36] Hänggi, P., Marchesoni, F., and Nori, F. Brownian Motors. *Annalen der Physik 14*, 1-3 (2005), 51–70.

[37] Hänsch, T., and Schawlow, A. Cooling of Gases by Laser Radiation. *Optics Communications 13*, 1 (1975), 68 – 69.

[38] Itano, W. M., Bergquist, J. C., Bollinger, J. J., Gilligan, J. M., Heinzen, D. J., Moore, F. L., Raizen, M. G., and Wineland, D. J. Quantum projection noise: Population fluctuations in two-level systems. *Phys. Rev. A 47* (May 1993), 3554–3570.

[39] Jones, P. H., Goonasekera, M., and Renzoni, F. Rectifying Fluctuations in an Optical Lattice. *Phys. Rev. Lett. 93* (Aug 2004), 073904.

[40] Kasevich, M. *Atom Interferometry in an Atomic Fountain*. PhD thesis, Stanford University, June 1992.

[41] Kasevich, M., and Chu, S. Atomic Interferometry using Stimulated Raman Transitions. *Phys. Rev. Lett. 67* (Jul 1991), 181–184.

[42] Lebedev, V. *AC Driven Ratchets for Cold Atoms: Beyond 1D Rocking Ratchets*. PhD thesis, University College London (UCL), October 2009.

[43] Lebedev, V., and Renzoni, F. Two-dimensional Rocking Ratchet for Cold Atoms. *Phys. Rev. A 80* (Aug 2009), 023422.

[44] Letokhov, V. S. Narrowing of the Doppler Width in a Standing Light Wave. *JETP Lett. 7* (1968), 272.

[45] Letokhov, V. S., and Minogin, V. G. Cooling, Trapping, and Storage of Atoms by Resonant Laser Fields. *J. Opt. Soc. Am. 69*, 3 (Mar 1979), 413–419.

[46] Lett, P. D., Watts, R. N., Westbrook, C. I., Phillips, W. D., Gould, P. L., and Metcalf, H. J. Observation of Atoms Laser Cooled below the Doppler Limit. *Phys. Rev. Lett. 61* (Jul 1988), 169–172.

[47] Li, R., and Gibble, K. Comment on 'Accurate Rubidium Atomic Fountain Frequency Standard'. *Metrologia 48*, 5 (2011), 446.

[48] Li, R., Gibble, K., and Szymaniec, K. Improved Accuracy of the NPL-CsF2 Primary Frequency Standard: Evaluation of Distributed Cavity Phase and Microwave Lensing Frequency Shifts. *Metrologia 48*, 5 (2011), 283.

[49] Linke, H., Alemán, B. J., Melling, L. D., Taormina, M. J., Francis, M. J., Dow-Hygelund, C. C., Narayanan, V., Taylor, R. P., and Stout, A. Self-Propelled Leidenfrost Droplets. *Phys. Rev. Lett. 96* (Apr 2006), 154502.

[50] Lu, Z. T., Corwin, K. L., Renn, M. J., Anderson, M. H., Cornell, E. A., and Wieman, C. E. Low-Velocity Intense Source of Atoms from a Magneto-optical Trap. *Phys. Rev. Lett. 77* (Oct 1996), 3331–3334.

[51] Mennerat-Robilliard, C., Lucas, D., Guibal, S., Tabosa, J., Jurczak, C., Courtois, J.-Y., and Grynberg, G. Ratchet for Cold Rubidium Atoms: The Asymmetric Optical Lattice. *Phys. Rev. Lett. 82* (Jan 1999), 851–854.

[52] Neumann, E., and Pikovsky, A. Quasiperiodically Driven Josephson Junctions: Strange Nonchaotic Attractors, Symmetries and Transport. *The European Physical Journal B - Condensed Matter and Complex Systems 26*, 2 (2002), 219–228.

[53] Ovchinnikov, Y., and Marra, G. Reply to 'Comment on 'Accurate Rubidium Atomic Fountain Frequency Standard' '. *Metrologia 48*, 5 (2011), 448.

[54] Ovchinnikov, Y. B. Compact Magneto-optical Sources of Slow Atoms. *Optics Communications 249*, 4 (2005), 473 – 481.

[55] Ovchinnikov, Y. B. Development of NPL Rb Fountain Frequency Standard. In *Proceedings of European Time and Frequency Forum* (2012), [arXiv:1206.1158].

[56] Ovchinnikov, Y. B., and Marra, G. Accurate Rubidium Atomic Fountain Frequency Standard. *Metrologia 48*, 3 (June 2011), 87.

[57] Ovchinnikov, Y. B., Szymaniec, K., and **Edris, Soliman**. Measurement of Rubidium Ground-State Hyperfine Transition Frequency Using Atomic Fountains. *Metrologia 52* (2015), 595–599.

[58] Parrondo, J., and Dinís, L. Brownian Motion and Gambling: From Ratchets to Paradoxical Games. *Contemporary Physics 45*, 2 (2004), 147–157.

[59] Phillips, W. D. Nobel Lecture - Laser Cooling and Trapping of Neutral Atoms. *Reviews of Modern Physics 70* (1998), 721.

[60] Phoonthong, P. *State-Insensitive Traps for Caesium Atoms.* PhD thesis, University College London (UCL), February 2012.

[61] Prost, J., Chauwin, J.-F. m. c., Peliti, L., and Ajdari, A. Asymmetric Pumping of Particles. *Phys. Rev. Lett. 72* (Apr 1994), 2652–2655.

[62] Quintero, N. R., Cuesta, J. A., and Alvarez-Nodarse, R. Symmetries Shape the Current in Ratchets Induced by a Biharmonic Driving Force. *Phys. Rev. E 81* (Mar 2010), 030102.

[63] Rahman, A., Sanyal, M. K., Gangopadhayy, R., De, A., and Das, I. Evidence of a Ratchet Effect in Nanowires of a Conducting Polymer. *Phys. Rev. B 73* (Mar 2006), 125313.

[64] Raman, C., Abo-Shaeer, J. R., Vogels, J. M., Xu, K., and Ketterle, W. Vortex Nucleation in a Stirred Bose-Einstein Condensate. *Phys. Rev. Lett. 87* (Nov 2001), 210402.

[65] Ramsey, N. F. Nobel Lecture - Experiments with Separated Oscillatory Fields and Hydrogen Masers. *Reviews of Modern Physics 62* (Jul 1990), 541–552.

[66] Reimann, P. Brownian Motors: Noisy Transport far from Equilibrium. *Physics Reports 361* (2002), 57–265.

[67] Reimann, P., and Hänggi, P. Introduction to the Physics of Brownian Motors. *Applied Physics A 75*, 2 (2002), 169–178.

[68] Renzoni, F. Chapter 1 Driven Ratchets for Cold Atoms . In *Advances in Atomic Molecular and Optical Physics*, P. R. B. E. Arimondo and C. C. Lin, Eds., vol. 57 of *Advances In Atomic, Molecular, and Optical Physics*. Academic Press, 2009, pp. 1 – 32.

[69] Renzoni, F. Ratchets from the Cold: Brownian Motors with Cold Atoms in Optical Lattices. *Europhysics News 43*, 1 (2012), 26.

[70] Ricci, L., Weidemüller, M., Esslinger, T., Hemmerich, A., Zimmermann, C., Vuletic, V., König, W., and Hänsch, T. A Compact Grating-Stabilized Diode Laser System for Atomic Physics. *Optics Communications 117*, 5 (1995), 541 – 549.

[71] Rousselet, J., Salome, L., Ajdari, A., and Prost, J. Directional Motion of Brownian Particles induced by a Periodic Asymmetric Potential. *Nature 370* (1994), 446–447.

[72] Salger, T., Kling, S., Hecking, T., Geckeler, C., Morales-Molina, L., and Weitz, M. Directed Transport of Atoms in a Hamiltonian Quantum Ratchet. *Science 326*, 5957 (2009), 1241–1243.

[73] Santarelli, G., Laurent, P., Lemonde, P., Clairon, A., Mann, A. G., Chang, S., Luiten, A. N., and Salomon, C. Quantum Projection Noise in an Atomic Fountain: A High Stability Cesium Frequency Standard. *Phys. Rev. Lett. 82* (Jun 1999), 4619–4622.

[74] Shalóm, D. E., and Pastoriza, H. Vortex Motion Rectification in Josephson Junction Arrays with a Ratchet Potential. *Phys. Rev. Lett. 94* (May 2005), 177001.

[75] Smoluchowski, M. Experimentell Nachweisbare, der Üblichen Thermodynamik Widersprechende Molekularphänomene. *Physikalische Zeitschrift 13* (1912), 1069–1080.
reprinted in *Pisma Mariana Smoluchowskiego 2*, 1 (1927), 226-251.

[76] Snyder, W. F. Lord Kelvin on Atoms as Fundamental Natural Standards (for Base Units). *IEEE Transactions on Instrumentation and Measurement 22*, 1 (March 1973), 99–99.

[77] Steck, D. Rubidium 87 D Line Data.
available online at
`http://steck.us/alkalidata/rubidium87numbers.pdf`.

[78] Steck, D. Cesium D Line Data.
available online at
`http://steck.us/alkalidata/cesiumnumbers.pdf`.

[79] Switkes, M., Marcus, C. M., Campman, K., and Gossard, A. C. An Adiabatic Quantum Electron Pump. *Science 283*, 5409 (1999), 1905–1908.

[80] Szymaniec, K., Park, S. E., Marra, G., and Chalupczak, W. First Accuracy Evaluation of the NPL-CsF2 Primary Frequency Standard. *Metrologia 47*, 4 (2010), 363.

[81] Tait, P. G., and Kelvin, W. T. *Elements of Natural Philosophy.* Cambridge University Press, 1879.

[82] van der Meer, D., Reimann, P., van der Weele, K., and Lohse, D. Spontaneous Ratchet Effect in a Granular Gas. *Phys. Rev. Lett. 92* (May 2004), 184301.

[83] van Oudenaarden, A., and Boxer, S. G. Brownian Ratchets: Molecular Separations in Lipid Bilayers Supported on Patterned Arrays. *Science 285*, 5430 (1999), 1046–1048.

[84] Villegas, J. E., Savel'ev, S., Nori, F., Gonzalez, E. M., Anguita, J. V., García, R., and Vicent, J. L. A Superconducting

Reversible Rectifier That Controls the Motion of Magnetic Flux Quanta. *Science 302*, 5648 (2003), 1188–1191.

[85] Weiss, S., Koelle, D., Mller, J., Gross, R., and Barthel, K. Ratchet Effect in dc SQUIDs. *EPL (Europhysics Letters) 51*, 5 (2000), 499.

[86] Wickenbrock, A. *Cold Atoms in Light Fields: From Free-space Optical Lattices to Multi-mode Optical Cavities*. PhD thesis, University College London (UCL), March 2012.

[87] Wineland, D. J., Dalibard, J., and Cohen-Tannoudji, C. Sisyphus Cooling of a Bound Atom. *J. Opt. Soc. Am. B 9*, 1 (Jan 1992), 32–42.

[88] Wynands, R., and Weyers, S. Atomic Fountain Clocks. *Metrologia 42*, 3 (2005), S64.

[89] Yevtushenko, O., Flach, S., Zolotaryuk, Y., and Ovchinnikov, A. A. Rectification of Current in ac-Driven Nonlinear Systems and Symmetry Properties of the Boltzmann Equation. *EPL (Europhysics Letters) 54*, 2 (2001), 141.